The Dissertation Committee for Monroe Patrick Griffin certifies that this is the approved version of the following dissertation:

Probing the Chemistry and Morphology of Material Interfaces in Emerging Photovoltaics

Committee:

David A. Vanden Bout, Supervisor

Ananth Dodabalapur

Graeme A. Henkelman

Charles Buddie Mullins

Sean T. Roberts

Probing the Chemistry and Morphology of Material Interfaces in Emerging Photovoltaics

by

Monroe Patrick Griffin

Dissertation

Presented to the Faculty of the Graduate School of

The University of Texas at Austin

in Partial Fulfillment

of the Requirements

for the Degree of

Doctor of Philosophy

The University of Texas at Austin

May 2018

Dedication

To my family, blood and chosen.

Acknowledgements

I have been so fortunate to receive the support of many different people as I have worked my way through graduate school. To start, I would like to thank my advisor, Professor David Vanden Bout, for providing his guidance, support, and knowledge throughout this whole journey. I thank you for taking me into your group, and it is because of you that I am the independent scientist I am today.

I would like to thank Dr. Raluca Gearba and Dr. Andrei Dolocan. It is hard to describe the influence you have had. Raluca was always willing to help by sharing her knowledge, especially her expertise in polymer materials and characterization tools, as well as general life advice. Her guidance was always welcomed and helpful. Andrei showed me a unique passion for understanding every minute detail. It is because of him that I know and have enjoyed learning everything I do about ToF-SIMS (and maybe figure making). I appreciate these two for being great colleagues as well as good friends.

Graduate school would not have been the same without my groupmates. I thank Dr. Micah Glaz and Dr. Marlene Gutierrez for encouraging me to work on organic photovoltaics. Marlene was a great and fun mentor to have in my first few years. Dr. Oleksiy Slobodyan (from the Dodabalapur Group) was tremendously helpful with my foray into device making. I would like to thank Dr. Katie Mulligan (née Clark) for her moral support and (graduate school) wisdom, especially around the time of my qualifying exam. I thank Dr. Leigh Krueger for all of our distressing talks and walks, and I think the CVS on Guad will miss our frequent trips. And, I would like to thank the rest of the group for their respect, friendship, and individual impact on my graduate career: Shauna Law (née Ingle), Dr. Zhongjian Hu, Dr. Katherine Milligan (née Koen), Dr. Beiyue Shao, Geoff Geberth, Jason Michael, and Emily McHugh.

I thank Professor Alan Campion for his mentoring. I had many opportunities to work and learn directly with him as his teaching assistant, in both lectures and lab. I am grateful for the unique experience with our time in revamping the Physical Chemistry labs – you pushed me to grow as a scientist as well as an instructor. Moreover, I enjoyed all of our intelligent conversations, especially those related to my Austin allergies.

I would not be where I am today without the love of my family. My parents, especially, have always supported my education. My time in graduate school saw a number of changes with respect to my immediate family. I owe the beginnings of my scientific curiosity to my late father, James, whose career as a boilermaker taught him a lot about chemistry, to which he passed along to my brother and I at an early age, and in many fun ways (i.e. learning optics by staring at the sun through welding glasses). My mother, Marie's, love of numbers and computers sparked my interest in math, and to this day, she has been such an advocate for my scientific endeavors. My parents, as well as the rest of my family, may not have understood what I have been doing, but they undeniably encouraged me in it.

Last, but not least, I would like to thank all of my friends – those from before graduate school and those that I made during my time in Austin. I have amassed so many friends outside of science and now, hopefully, you now have a better understanding of what I do. I am thankful for the almost daily encouragement/phone calls from Arienne Thacker and Raiford Collins. I am thankful for the unwavering support of my college roommate, Jamie Arakas, and his family, especially Wendy (Mama) and Mike (Papa) throughout this time. I wish I could continue listing everyone that has supported me through this process, but that would be longer than this dissertation. I hope you know who you are and the impact you have made. I cannot be more grateful and thankful for everyone in my life during this time.

Probing the Chemistry and Morphology of Material Interfaces in Emerging Photovoltaics

Monroe Patrick Griffin, Ph.D.

The University of Texas at Austin, 2018

Supervisor: David A. Vanden Bout

Emerging photovoltaics hold great promise to add to the existing solar cell market by either becoming cost competitive or accessing new, niche markets unavailable to current technologies. Unfortunately, wide adoption of these systems, in particular organic photovoltaics (OPVs) and perovskite photovoltaics, is hampered by overall poor performance in either efficiency (in OPVs) or in long-term stability (in perovskite photovoltaics). Designing better materials and optimizing device morphology/architectures, with the latter changing intrinsic material interfaces within the devices, has made progress to overcome some of these issues. Since these interfaces affect overall efficiency and stability, understanding interface chemistry (composition) and morphology is important in understanding overall device performance. Characterization of these interfaces requires techniques capable of probing the chemistry-morphology relationship at the nanoscale. Here, we use Time-of-Flight Secondary Ion Mass Spectrometry (ToF-SIMS) and Atomic Force Microscopy (AFM) to characterize these material systems and their device interfaces. In P3HT:PCBM, a classic OPV system, we directly imaged the active layer buried morphology and determined the mixing length of the D/A interface, which is crucial for device performance and had yet to be measured. We determined, contrary to the general understanding, that thermal annealing in this system

actually leaves the bulk heterojunction film mostly mixed. Our methodology provides a route to determining this D/A interface length for other OPV systems providing a new metric and insight for better device design principles. For $MAPbI_3$ perovskites, we studied interfacial behavior to understand light-induced degradation in functioning devices and electrical-induced degradation in films based on contact selection as well as visualized bias-induced ion migration. We determined that the PDI-EH electron transport layer hinders degradation; whereas, a PCBM electron transport layer allows and facilitates it. For electrical degradation, we determined that an ITO electrode induces more degradation than a platinum contact by measuring interface $MAPbI_3$/ITO mixing. And, by using lateral $MAPbI_3$ devices, we visualized ion migration due to an applied electric field. For perovskite devices, interfacial behavior dictates long-term performance. Overall, using a combination of ToF-SIMS and AFM to interrogate interfacial chemistry and morphology, we are working towards better devices through understanding limits on efficiency and stability.

Table of Contents

List of Figures

List of Abbreviations

The following list defines select abbreviations and acronyms used throughout the dissertation. Not all abbreviations and acronyms used in this dissertation are listed here, but these and the rest are defined at least once in the text where they occur.

A	Electron Acceptor or Anode (Chapter 5)
AFM	Atomic Force Microscopy (or Microscope)
ALD	Atomic Layer Deposition
BA	Burst Alignment
BHJ	Bulk Heterojunction
BL	bilayer
C	Cathode
$CH_3NH_3PbI_3$	methylammonium lead iodide (also $MAPbI_3$)
D	Electron Donor
D/A interface	Electron Donor/Electron Acceptor interface
dPCBM	pentadeuterophenyl-C_{61}-butyric acid methyl ester
DRF	Depth Resolution Function
D-SIMS	Dynamic Secondary Ion Mass Spectrometry
DSSC	Dye Sensitized Solar Cell
EBIC	Electric Beam Induced Current
EDS	Energy-Dispersive X-Ray Spectroscopy (also EDX)
EDX	Energy-Dispersive X-Ray Spectroscopy (also EDS)
EELS	Electron Energy Loss Spectroscopy
EFTEM	Energy-Filtered Transmission Electron Microscopy

EQE	External Quantum Efficiency
ESI	Electrospray Ionization
ET	Electron Tomography
ETL	Electron Transport Layer
FA	formamidinium
$FAPbI_3$	formamidinium lead iodide (also $NH_2CHNH_2PbI_3$)
FF	Fill Factor
FIB	Focused Ion Beam
GIWAXS	Grazing-Incidence Wide-Angle X-ray Scattering
HC	High-current
HPLC	High-Performance Liquid Chromatography
HTL	Hole Transport Layer
IPES	Inverse Photoelectron Spectroscopy
ITO	Indium Tin Oxide
J_{SC}	Short Circuit Current
KPFM	Kelvin Probe Force Microscopy
LBIC	Light Beam Induced Current
LMIG	Liquid Metal Ion Gun
MA	methylammonium
$MAPbI_3$	methylammonium lead iodide (also $CH_3NH_3PbI_3$)
MRI model	Mixing-Roughness-Information model
NEXAFS	Near Edge X-ray Absorption Fine Structure
$NH_2CHNH_2PbI_3$	formamidinium lead iodide (also $FAPbI_3$)
NR	Neutron Reflectivity
OPV	Organic Photovoltaic

P3HT	poly (3-hexylthiophene-2-5-diyl)
PCBM	[6,6]-phenyl-C_{61}-Butyric acid methyl ester
PCE	Power Conversion Efficiency
PDI	perylene diimide
PDI-EH	N,N'-di-2-ethylhexyl-3,4,9,10-perylenetetracarboxylic diimide
PEDOT:PSS	poly(3,4-ethylenedioxythiophene):polystyrene sulfonate
PID loop	proportional–integral–derivative loop
PTIR	Photothermal Induced Resonance
RMS	Root Mean Square
ROI	Region of Interest
RSoXS	Resonant Soft X-ray Scattering
SEM	Scanning Electron Microscopy
SHG	Second Harmonic Generation
SIMS	Secondary Ion Mass Spectrometry
SPM	Scanning Probe Microscopy
STXM	Scanning Transmission X-ray Microscopy
TA	Transient Absorption
TEM	Transmission Electron Microscopy
ToF	Time-of-Flight
ToF-SIMS	Time-of-Flight Secondary Ion Mass Spectrometry
UPS	Ultraviolet Photoelectron Spectroscopy
UV	Ultraviolet
V_{OC}	Open Circuit Voltage
XPS	X-ray Photoelectron Spectroscopy

Chapter 1: The Importance of Interfaces in Emerging Photovoltaics

1.1 MOTIVATION

Current estimates place the world's growing energy demand to increase by 28% over the next two decades (2040) with renewable energy sources being the fastest growing market to meet this demand.[1] Solar energy is one part of this diverse portfolio (hydroelectric, wind, biomass, solar and geothermal) and is harnessed with the use of solar cells (photovoltaics). Currently, commercially available crystalline silicon (c-Si) solar cells (~21%, as high as 26%[2]) make up most of the market (90%) with the rest of the market shared by gallium arsenide (GaAs) and thin film technologies, amorphous silicon hydride (a-Si:H), cadmium telluride (CdTe), and copper indium diselenide ($CuInSe_2$).[3] Even so, emerging photovoltaics (organic, perovskite, dye-sensitized, quantum dot, etc.) still hold great promise to add to the existing market by either becoming cost competitive (scaled to output/efficiency/stability) or more likely, accessing new, niche markets unavailable to current commercial technologies. My work will focus on two types of emerging photovoltaic systems: organic photovoltaics (OPVs) and perovskite photovoltaics.

Although different material systems, OPVs and perovskite photovoltaics offer some of the same advantages. For one, these materials are easily dissolved in common solvents providing for cheaper device fabrication/processing (spin coating, printing, doctor blading, etc.) when compared to the energy-intensive fabrication associated with current inorganic photovoltaics.[4–8] In addition, these materials have advantageous mechanical properties, such as flexibility, coupled with being lightweight, due to high absorption coefficients ($>10^4$),[9–11] opening up these solar cells to new markets, such as wearables.[4,12] And, in the case of OPVs, the possibility of a semi-transparent active layer

allows for integration into areas such as window coatings, where conventional opaque inorganic solar cells cannot be utilized.[12,13] Although the systems have many advantages and progress is being made, both of these systems are still the focus of much fundamental research. For OPV technologies the issues is the relatively low efficiencies (current best single solar cells at ~11.7%).[14] For perovskites the efficiencies are better (currently at ~22%)[15] but they have long-term stability issues[6,16–18] .

To overcome efficiency and stability issues in these systems, research has focused on designing better materials as well as optimizing device morphology/architecture. For OPVs, improvements have come from synthesizing new materials (conjugated polymers and small molecules) [19–24] as well as optimizing device morphologies (bilayers and bulk heterojunctions with processing conditions)[25–30] and architectures (single cells, tandem cell, multijunction cells).[14,31–33] In perovskites photovoltaics, similar advances in material design (by changing composition and/or stoichiometric ratios of A[34–38], B[16,39], and/or X[40–44] in the typical ABX_3 perovskite crystal structure) and using different device architectures (nanostructured[34,45–51] or planar[8,51–53]) have increased efficiency and stability.

With synthetic capabilities able to produce almost any desired material, the continued focus on optimizing and understanding device morphologies is critical. When thinking about device morphologies and architectures, it is the *interfaces* between different materials that are of primary interest. At the core of changing the device morphology or architecture to increase performance is the change in the device interfaces with respect to interfacial chemistry/composition and interfacial morphology. A number of important physical processes occur in photovoltaics at these interfaces (such as, charge generation, charge transfer, recombination, etc.), either within the active layer itself, between the active layer and supporting layers (i.e. electron transport layers or hole

transport layers), or just between different supporting layers. The key to understanding the composition-morphology relationship to performance is in understanding interfaces. Characterization of these device interfaces requires techniques that are capable of determining chemical, spatial, and energetic information on the nanoscale.

Section 1.2 looks at the role of buried interfaces within the active layer of organic photovoltaics (OPVs). **Section 1.3** describes the role of buried interfaces between devices layers in perovskite photovoltaics. Finally, **Section 1.4** outlines currently available techniques to study various aspects of interfaces.

1.2 BURIED INTERFACES IN ORGANIC PHOTOVOLTAICS (OPVS)

Organic photovoltaics have an active layer made of organic, that is, mainly carbon based, materials that fall into two classes: polymers and small molecules. Although small molecule-based OPVs have made similar advances, this work will focus on polymer-based OPVs, in which the polymer is some highly conjugated, semiconducting polymer. For these materials, the relatively low dielectric permittivity ($\varepsilon \approx 3-4$) provides poor charge screening, creating coulombically bound electron-hole pairs (excitons, with binding energy, $E_b \approx 0.5-1$ eV) upon light excitation, necessitating the use of an electron accepting material in creating free (unbound) charges.[54] Coupling the electron donor (conjugated polymer) with the electron acceptor (typically a fullerene derivative) occurs with two different device structures of either a bilayer or a bulk heterojunction (BHJ). **Figure 1.1** gives the chemical structures of a common conjugated polymer, poly(3-hexylthiophene-2,5-diyl) (P3HT), and a common fullerene derivative, [6,6]-phenyl-C_{61}-butyric acid methyl ester (PCBM), as well as schematics for a bilayer device and a BHJ device.

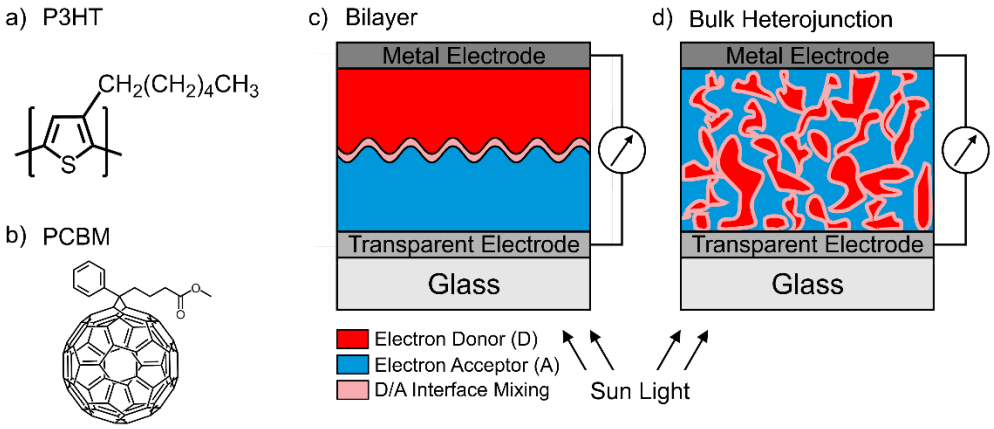

Figure 1.1 Typical OPV materials and device structures. (a) a common electron donor (conjugated polymer), P3HT, (b) a common electron acceptor (fullerene derivative, PCBM, (c) schematic of bilayer device structure and (d) schematic of BHJ device structure showing regions of pure donor (D, red) and pure acceptor (A, blue) as well as the D/A interface (mixing, pink).

Currently, the most progress in power conversion efficiency (PCE) has been achieved in polymer:fullerene BHJs by synthesizing polymers with low band gap[19–23] and optimizing the device morphology.[25–30] In these BHJ devices, both conjugated polymer (electron donor, D) and fullerene derivative (electron acceptor, A) are mixed in a common solvent and cast together to form the active layer (~100 nm thick). Here, The "desirable" morphology is commonly attained by trial-and-error, employing a battery of preparation procedures that can include thermal[11,25,55] or solvent vapor[26,56,57] annealing, and choice of solvent,[29,58] rate of solvent removal,[59,60] relative volume fraction of the donor and acceptor,[29,30,61] and use of chemical additives.[27,28,62] However, these strategies lead to complex and largely unknown morphologies with no clear link to increases in performance.

Functionally, the common understanding in these systems is that phase segregation, through any number of aforementioned preparation procedures, results in the

formation of relatively pure donor (D) and acceptor (A) nanometer size domains (**Figure 1.1**d).[63,64] Light absorption mostly in the donor material creates bound excitons that dissociate into free charges at the D/A interface. In these systems, the exciton diffusion length, before recombination occurs, is ~10 nm,[65] necessitating the need for small diffusion pathways to the D/A interface. After dissociation, transport of the resulting free charges towards the electrodes occurs in the relatively pure domains. Recently, the presence of a third, intermixed (at molecular level) composite phase between the pure phases has been identified (pink, **Figure 1.1**d) and there is compelling evidence that the extent of this mixed phase controls the charge separation and therefore the device efficiency.[64,66–73]

This molecularly mixed, composite phase contains many molecular D/A interfaces. A larger region of mixing is beneficial for free charge generation as it provides a larger region for exciton dissociation while also reducing exciton recombination by reducing the distance the exciton must travel in the pure phases to a D/A interface. However, it is the pure phases that are important for transport and minimizing free charge recombination. More mixing implies less pure material phases for efficient charge transport as well as more regions for free charge recombination, that is, a hole in the donor material is generally located closer to an electron in the acceptor material. External device efficiency improves with higher free charge generation but diminishes with poor transport and/or high charge recombination and vice versa. Thus, there is an inherent trade-off to the extent of this mixed phase that is important for external device efficiency. It is this mixed phase, that is, the *buried* donor/acceptor interface that is of interest in improving device efficiency in OPVs.

Moreover, the ability to identify and interrogate this mixed phase or D/A interface in these systems is a general challenge. Since mixing in these systems occurs on

nanometer length scales, techniques that aim to understand the composition-morphology relationship fail at providing high enough chemical sensitivity to separate the mixing component or fail at providing high enough spatial resolution in identifying the extent of mixing. **Section 1.4** discusses the successes and limitations of some current techniques to study buried interfaces in OPVs. **Chapter 3** will explore my work with understanding molecular mixing in OPVs.

1.3 INTERFACES IN PLANAR PEROVSKITE PHOTOVOLTAICS

The family of perovskite materials has a crystal structure in the form ABX_3 and is named after Russian Mineralogist Lev A. Perovski. Prussian Mineralogist Gustav Rose discovered the first perovskite, calcium titanium oxide ($CaTiO_3$), in 1839 from analyzing a piece of skarn taken from the Ural Mountains and collected by Russian Mineralogist Alexander Kämmerer.[74] The first attempt of using a perovskite material for photovoltaics appeared in dye-sensitized solar cells (DSSC) by using organic-inorganic hybrid perovskites, methylammonium lead iodide ($CH_3NH_3PbI_3$) and methylammonium lead bromide ($CH_3NH_3PbBr_3$), as the light-absorbing sensitizer in the solar cells in 2009.[75] Most often, in these semiconducting perovskites the monovalent A cation is some organic cation, typically, methylammonium ($CH_3NH_3^+$, MA) or formamidinium ($NH_2CHNH_2^+$, FA); the divalent B cation is some metallic cation, typically, lead (Pb^{2+}); and, the monovalent X anion is some halide or mix of halides, typically, iodide (I^-), bromide (Br^-) or chloride (Cl^-), giving them the name organic-inorganic hybrid perovskites. A generalized crystal structure is given in **Figure 1.2**

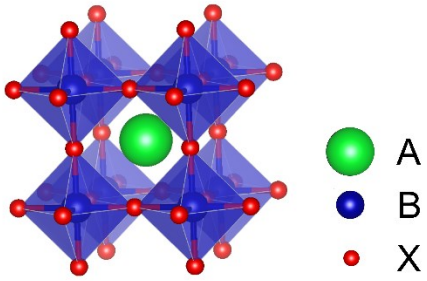

Figure 1.2 Perovskite crystal structure, ABX_3. For typical hybrid perovskites, A is an organic cation, B is a metal anion, and X is a halide.

The use of perovskites in solid-state photovoltaics has taken off over the past few years. Within the past decade, they have gone from initial efficiencies of <10% to ~22%[15] with much success coming from simple improvements in material composition and device architecture.[76] In these systems, light absorption generates excitons that readily dissociate into free charges at room temperature (~25 meV). The nature of the exciton is still debated, but most estimates suggest the binding energy is ~50 meV.[76–78] More importantly, hybrid organic-inorganic perovskites have large electron and hole diffusion lengths (100 nm – 1000 nm)[77] especially when compared to device thicknesses (~100 nm) suggesting that generated free charges can be collected externally without loss. Moreover, the electron and hole diffusion lengths are similar (i.e. balanced) meaning that there is little efficiency loss to do charge build-up in the active layer itself; this also suggests the ambipolar nature of perovskite films requiring some bias (internal or external) to extract charges. Lastly, large crystalline domains (~200 nm to >1 μm),[79] reduce the effect of grain boundaries in these systems, thus reducing disorder, which can facilitate charge trapping/recombination. Considering all of these factors, organic-inorganic hybrid perovskite materials make for great photovoltaic candidates in terms of initial device performance, that is, initial efficiency.

However, organic-inorganic hybrid perovskites are unstable under a number of external stresses, some of which are vastly important for photovoltaic applications: moisture/humidity,[6,80] light exposure,[6,52,80] electrical bias,[6,80,81] and thermal decomposition.[82] Besides material engineering of the perovskite itself, device/interface engineering has led to drastic improvements in performance (efficiency and long-term stability).[6,12] Device engineering has succeeded by manipulating the bulk geometry and/or composition of layers and thus, changing the nanoscale composition and morphology of the device interfaces. **Figure 1.3** gives common device architectures used in perovskite photovoltaics.

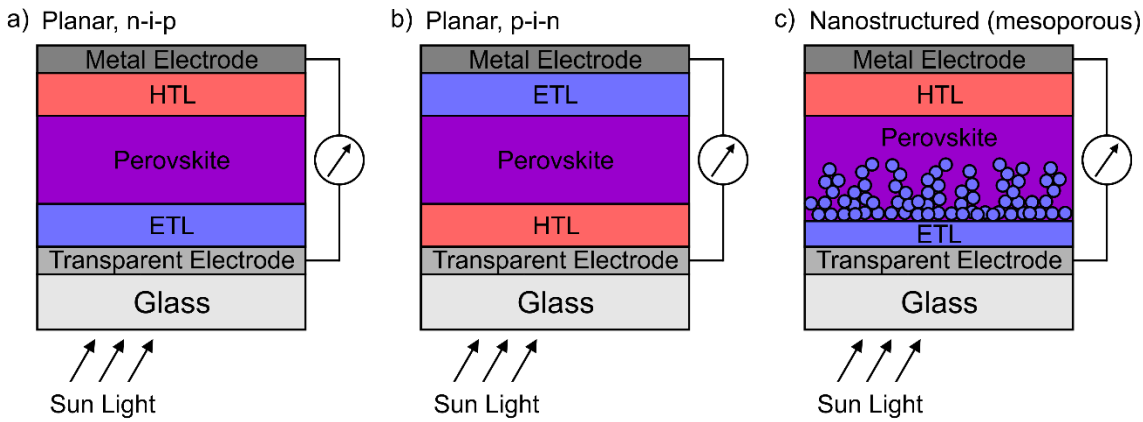

Figure 1.3 Common perovskite photovoltaic device architectures. (a) a planar, n-i-p structure, (b) a planar, p-i-n structure, (c) a nanostructured, or mesoporous, structure. HTL: Hole Transport Layer, ETL: Electron Transport Layer

To address moisture degradation in perovskite devices, researchers have looked at the effect of supporting layer composition and device geometry. The mechanism of perovskite degradation with moisture is still debated.[6,83–85] But, for $CH_3NH_3PbI_3$, decomposition with water produces HI and CH_3NH_2 leaving behind solid PbI_2. In the presence of UV radiation and oxygen, HI can be oxidized into I_2 and H_2O, continuing the

cycle.[80] Separately, a perovskite hydrate can form (say, $(CH_3NH_3)PbI_6 \cdot 2\ H_2O$)[84], which does not have beneficial photovoltaic properties. The most common approach to improve stability has been to introduce hydrophobicity into the device either by selecting a more hydrophobic hole[83] (HTL) or electron[86] (ETL) transport material layer, altering the interface between perovskite and supporting layers,[87–89] or altering interactions within the perovskite layer itself.[90] All of these changes showing the importance of interface chemistry to prevent moisture degradation. Moreover, changing device geometry has led to stability advances. In a typically planar structure (n-i-p, **Figure 1.3**a), the HTL is in direct contact with the perovskite towards the top- (air) interface; whereas, in an inverted planar device structure (p-i-n, **Figure 1.3**b) it is on the bottom. Simply changing the geometry improves stability.[6] However, in inverted device structures, the n-type material (i.e. C_{60}) is only tens of nanometers thick, potentially being a poor barrier and providing pathways for water and oxygen transport to the perovskite interface.[6] For practical use, devices are fabricated with an encapsulation layer to minimize moisture effects. Regardless, interface engineering has proven to increase perovskite device stability with respect to moisture degradation.

Photoinstability in perovskite photovoltaics stems from photo-oxidation caused by TiO_2 ETL[91] or photocatalyzed reactions of the perovskite with other supporting layers.[52,92] In devices with TiO_2, holes formed from UV excitation can react with adsorbed oxygen radicals forming energetic deep trap states for the excited electrons. An electron trapped in one of these states can either oxidize the perovskite (say, I^- to I_2) or recombine with free holes.[91,93] The solution here has been to modify the TiO_2/perovskite interface to reduce trap states[93–95] or use a different ETL layer (such as a fullerene[6] or perylene diimide (PDI)[52] derivative). It is also possible for photoinduced degradation of the perovskite to occur with the formation of volatile HI, I_2, H_2, and/or CH_3NH_2.[96] Where

diffusion of these products to the metal contact interface (or vice versa) leads to the formation of metal iodide complex (i.e. AgI)[52] as will be discussed in **Chapter 4**.

Electrical instability of perovskite photovoltaics manifests as a J-V hysteresis caused by one or more debated phenomena related to a capacitive effect in the material, such as ion migration,[97] interfacial trapping at grain boundaries and/or at supporting layers,[98] a photoinduced giant dielectric response,[99] or a ferroelectric response.[100] Interface engineering has worked to minimize this hysteresis leading to some of the advances in understanding the mechanism. By using a mesoporous device architecture (**Figure 1.3**c) versus a planar architecture (**Figure 1.3**a), the hysteresis can be reduced; furthermore, by going to an inverted planar device structure (**Figure 1.3**b), the effect is (almost) completely eliminated.[12,80,101,102] The effect of changing these geometries is thought to reduce ion migration as well as interfacial traps at either device interfaces or grain boundaries. In terms of extent, electrical biasing can cause reversible,[81,103–105] known as a switchable photovoltaic effect under light bias, or irreversible[81,96,106] degradation under prolonged or high bias. The effect is also controlled by choice of supporting layers, suggesting interface chemistry is a key factor.[81,101,102] A greater understanding of electrical instability for $MAPbI_3$ perovskites will be explored in **Chapters 4 and 5**.

Again, one of the main issues with studying these degradation pathways as related to interfaces is in having tools capable of both high chemical selectivity/sensitivity as well as spatial resolution to probe the nanoscale (or microscopic) domains/changes in these systems. **Section 1.4** summarizes some of the main techniques in studying perovskite photovoltaics interfaces. **Chapters 4 and 5** will explore my work in this field using Time-of-Flight Secondary Ion Mass Spectrometry (ToF-SIMS) to understand the chemical changes at the nanoscale due to light- and electric field- induced degradation.

1.4 METHODS OF STUDYING INTERFACES IN ORGANIC AND PEROVSKITE PHOTOVOLTAICS

Studying interfaces in organic and perovskite photovoltaics presents unique challenges that are based on the types of inherent interfaces in these systems, that is, the difference of buried interfaces *within* the active layer of OPVs and interfaces *between* the active layer and supporting layers in perovskite photovoltaics. Although different, the methods and techniques at approaching these problems are similar. While not an exhaustive list, here we will describe common techniques for studying interfaces with respect to understanding interface morphology and composition. It is important to note that there are also a number of techniques that measure surface/interface energetics (charge generation, charge transfer, charge recombination, band bending, etc.) that are vastly important in understanding overall device performance and rely on interfacial chemistry and morphology that will not be discussed here, as they are outside of the scope of this dissertation. Some examples of these techniques include Xray/Ultraviolet/Inverse Photoelectron Spectroscopy (XPS/UPS/IPES)[107,108] and any number of non-linear optical techniques, such as Transient Absorption (TA)[109,110] Spectroscopy and Second-Harmonic Generation (SHG).[111]

There is a myriad of techniques to study interface morphology. The use of scanning probe techniques to study organic and perovskite photovoltaics provides primarily for an understanding of interface morphology but also for an understanding of either energetics or composition, either directly or indirectly. Atomic Force Microscopy (AFM) is routinely used to understand surface topography of films which is useful in understanding surface coverage and defects (i.e. pin holes or grain boundaries).[28,62,112–115] Moreover, applications of AFM can show how surface energetics change with morphology, an example being Kelvin Probe Force Microscopy (KPFM) to look at

surface work function,[116,117] or how chemical composition changes with morphology, an example being Photothermal Induced Resonance (PTIR), where measuring spatial changes in thermal expansion relate to changes in chemical composition.[105] Other non-AFM based techniques are used to understand electronic-spatial behavior, such as Electric or Laser Beam Induced Current (EBIC[36,118] or LBIC[119]), where external current is collected as a function of excitation from electrodes, leading to and understanding of collection efficiency. In addition, some x-ray techniques, such as Grazing-Incidence Wide-Angle X-ray Scattering (GIWAXS),[14,77–79] Resonant Soft X-ray Scattering (RSoXS),[14,72,121] and Scanning Transmission X-ray Microscopy (STXM),[71,121] aim to understand morphology of bulk films and interfaces. In organic and perovskite systems these techniques can reveal crystalline orientation and in the case of polymer systems are able to determine the degrees and regions of crystallinity versus other polymer phases (that is, amorphous). Moreover, electron imagining techniques, such as Scanning Electron Microscopy (SEM)[122] and Transmission Electron Microscopy (TEM)[25,57,114,123–125] are capable of visualizing surface morphology. Some success with imaging interfaces in OPVs has come from cross-sectional TEM (in combination with Focused Ion Beam (FIB) milling) and other energy-dependent (i.e. composition-dependent) TEM techniques, such as Energy-Filtered TEM (EFTEM),[114,124] Electron Energy Loss Spectroscopy (EELS),[125] or Electron Tomography (ET).[123,125]

Other techniques aim to understand chemical composition at interfaces. Dynamic (D-)[67,126,127] and static, Time-of-Flight (ToF-)[52,81,113,128,129] Secondary Ion Mass Spectrometry (SIMS) are used to understand surface and interface composition. ToF-SIMS will be discussed throughout this dissertation in that manner. Neutron reflectivity (NR) is also a powerful technique capable of revealing chemical concentration and can indirectly measure composition of a film (and its interfaces),[115,130]

albeit with lower sensitivity than ToF-SIMS.[113] In addition, x-ray techniques, such as RSoXS,[14,72,121] Near Edge X-ray Absorption Fine Structure (NEXAFS)[71,120] and Energy-Dispersive X-Ray Spectroscopy (EDX),[96,128] are capable of revealing bulk/interfacial chemical composition. X-Ray Photoelectron Spectroscopy (XPS) is another highly surface selective technique capable of measuring surface composition and can perform depth profiling, similar to ToF-SIMS, to reveal chemical composition with depth and analyze buried interfaces.[128,131]

Although there are all of these techniques to study morphology, composition and energetics, none of these fully analyzes the relationship between all three nor do most of these techniques tackle two of these areas at once on the nanoscale. In order to understand the relationship between composition/morphology and relate it to device performance, there needs to be a technique capable of accessing chemical information as well as spatial information on the nanoscale. To do this, we will use a combination of ToF-SIMS, with the ability to determine chemical information with high selectivity and sensitivity, and AFM, with the ability to spatially resolve morphology at the nanoscale, to understand the changes in organic and perovskite photovoltaic systems that lead to better performing devices.

1.5 DISSERTATION OVERVIEW

In order to overcome performance issues in organic and perovskite photovoltaics, there is a need to understand interfacial behavior in these systems. For OPVs, buried interfaces within the active layer dictate device efficiency; for perovskite photovoltaics, the buried interfaces between active layer and supporting layers can dictate long-term stability. Thus, understanding and characterizing nanoscale device interfaces is crucial to understanding the composition-morphology relationship to performance. In order to

properly identify and investigate the chemistry and morphology of these interfaces on the nanoscale, a new technique is required to access chemical information and spatial information. Here, my work with ToF-SIMS with (or without) AFM is able to probe necessary changes in these systems to gain fundamental understanding of interfacial behavior that limits performance.

Chapter 2 will give a basic overview of Time-of-Flight Secondary Ion Mass Spectrometry (ToF-SIMS) and Atomic Force Microscopy (AFM) as well as explain the use of the two techniques in combination. **Chapter 3** will explore the use of ToF-SIMS/AFM in understanding the chemistry (composition) and morphology of buried interfaces in P3HT:PCBM bulk heterojunctions. **Chapter 4** details our work using ToF-SIMS in understanding the effects of light-induced degradation and electrical field-induced degradation in $MAPbI_3$ photovoltaics and films, respectively. And, **Chapter 5** will explore electrical degradation in lateral $MAPbI_3$ devices by *in situ* ToF-SIMS chemical imaging under bias.

Chapter 2: Combining ToF-SIMS and AFM to Study Interface Chemistry and Morphology

2.1 Time-of-Flight Secondary Ion Mass Spectrometry (ToF-SIMS)

Time-of-Flight Secondary Ion Mass Spectrometry (ToF-SIMS) is a powerful analytical technique used across many disciplines (physical sciences, earth sciences, material science/engineering, biosciences, etc.) to study surface chemistry/composition.

2.1.1 Operating Principles

In ToF-SIMS, a primary ion beam (analysis beam) bombards a sample's surface, which emits atomic and molecular fragments (as large or larger than 10,000 amu), most of which are neutral, but some (~1%) of which are ionized known as secondary ions (**Figure 2.1**).[132,133] These secondary ions are collected by a time-of-flight (ToF) analyzer to generate a mass spectrum of the sample surface. In this manner, ToF-SIMS provides elemental, including hydrogen, and molecular compositional information of the top surface (<1 nm) with high chemical sensitivity (ppm to ppb) and high mass resolution (0.001 amu).[132] In addition to point spectra, raster scanning the analysis beam can build up a chemical compositional map of the surface in an x-y plane with moderate spatial (lateral) resolution (~100 nm).[132] When surface analysis is combined with a separate sputtering beam (pink, **Figure 2.1**), depth profiling occurs as the sputtering beam intermittently exposes a new plane for analysis, producing spectra as a function of sputtering time, and thus, depth. Depth profiling is also done with high depth resolution (< 1 nm),[134] in part due to the energy of the sputtering beam, but also because of the surface selectivity of the analysis beam. Depth profiling is used to understand atomic and molecular mixing at buried interfaces, that is, interfaces below the top surface (the air-sample interface) of a sample film.

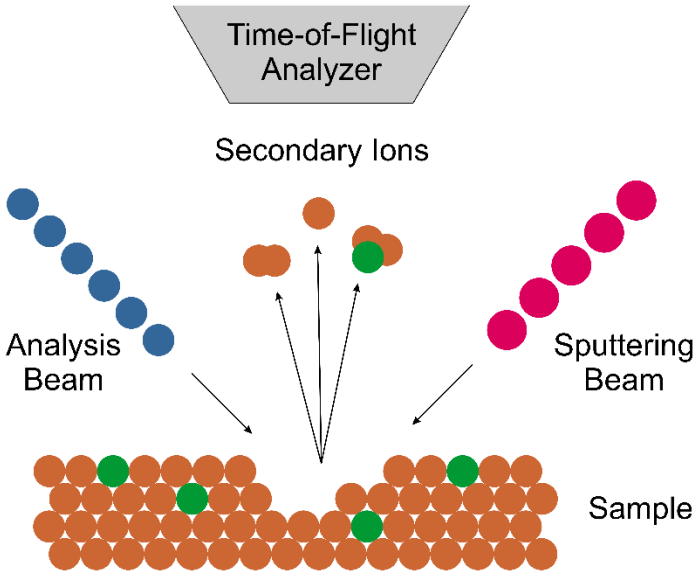

Figure 2.1 Schematic of ToF-SIMS operation. An analysis (primary ion) beam bombards the sample's surface, which emits secondary ions for detection with a time-of-flight mass analyzer to produce mass spectra. To do depth profiling, a sputtering beam removes the top surface, creating a fresh surface for analysis.

2.1.2 Depth Profiling

With ToF-SIMS depth profiling, a series of surface mass spectra are collected as a function of sputtering time, where sputtering time corresponds to a depth below the air-surface interface. In using this capability, depth profiling allows for studying the chemistry/composition of buried interfaces, that is interfaces below the surface of a film. However, there are some subtleties to understanding this experiment that can best be understood by examining a model case of a simple bilayer film. For a simple bilayer (**Figure 2.2**a), where one material (blue, Region A) is deposited on top of another material (pink, Region B), there is intrinsic atomic/molecular mixing (purple) at the now-buried interface between the two materials. The length of this interface over a macroscopic region will be the combination of this mixing length and the intrinsic

corrugation of the interface. Depth profiling through this bilayer provides chemical information in the form of mass spectra in which the selection of a unique ion fragment can map out the change in composition with sputtering time. For instance, a unique ion fragment or marker, A, for Region A, with maximum yield, I_A, in Region A, will change as you sputter through Region A and enter Region B (increase in sputtering time) to its minimum yield, I_B, in Region B due to the change in composition of material A in the different regions (**Figure 2.2**b). The change in yield (here, a drop) corresponds to the interface between the two materials.

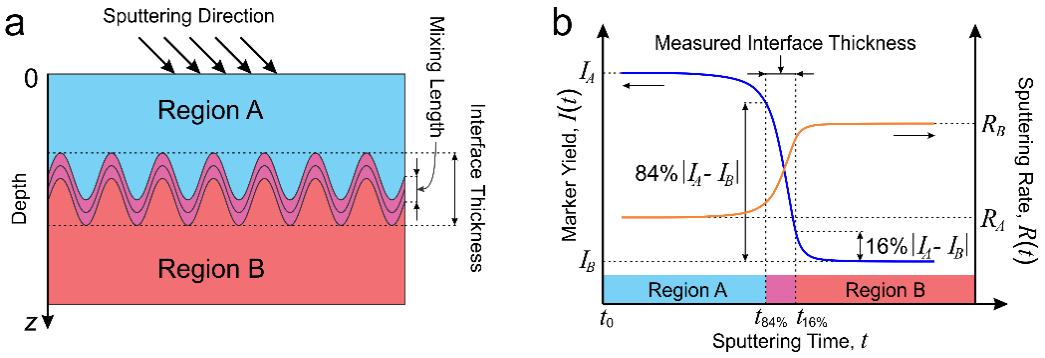

Figure 2.2 ToF-SIMS depth profiling through a simple bilayer system. (a) Schematic of bilayer showing interface mixing and corrugation as well as the direction of ToF-SIMS sputtering/analysis. (b) Depth profile of arbitrary ion fragment, A, showing the bilayer interface as well as changing sputtering rate from depth profiling.

To understand chemical concentration with depth, we must convert our data from sputtering time to depth, in a so-called, depth conversion. In our simply bilayer, each material sputters at a different (but constant) rate in the pure regions, R_A or R_B, for Region A or B, respectively. These sputtering rates are material- and operating condition-dependent and correspond to the etch rate. The sputtering rate for a pure material, R_{pure}, can be determined by sputtering through a standard of known thickness, z_{std},

$$R_{\text{pure}} = \frac{z_{\text{std}}}{t_{\text{total}}} \tag{2.1}$$

where t_{total} is the amount of sputtering time to pass through the standard pure film (in practice, this time can be taken to be where the signal falls off 50% at the film-substrate interface). For a simple bilayer system, the instantaneous overall sputtering rate, $R(t)$, through the interface can be assumed to be a linear combination[113,135,136] of these pure rates

$$R(t) = \left|\frac{I(t) - I_B}{I_A - I_B}\right| R_A + \left|\frac{I(t) - I_A}{I_A - I_B}\right| R_B \tag{2.2}$$

where $I(t)$ is the instantaneous yield of marker A (or B) across the interface. Now, depth conversion is simply done by integrating the instantaneous sputtering rate, $R(t)$, selecting either the pure sputtering rates (**Equation 2.1**) in the pure regions or the linear combination rate in the interface (**Equation 2.2**), to obtain a sputtering depth, $z(t)$, corresponding to sputtering time, t,

$$z(t) = \int_{t_0}^{t} dt' R(t') \tag{2.3}$$

where t_0 corresponds to the time at which a given region is reached.

For ToF-SIMS depth profiling, the sputtering beam can either be the same composition as the analysis beam (single beam) or of different composition (dual beam). In single beam operation, the ion beam alternates between a low-current high-energy pulsed analysis mode and a high-current low-energy DC sputtering mode; here, switching time and current stability can cause issues.[132] Single beam depth profiling requires a large cluster ion beam (i.e. C_{60}^+) for sputtering which gives the advantage of producing higher mass fragments and enhanced secondary ion yield during analysis, especially useful in organic systems.[137–139] With dual beam operation, analysis and sputtering are decoupled providing for optimal selection of separate analysis and sputtering beams. That is, the

analysis beam can be optimized for pulse width, lateral resolution and intensity; the sputtering beam optimized for depth resolution and sputtering rates.[132] For depth profiling, we will use dual beam operation with a bismuth (Bi_1^+ or Bi_3^+ ions) liquid-metal-ion-gun (LMIG) for analysis and a cesium (Cs^+) sputtering beam. In negative mode, cesium doping of the matrix enhances the ionization probability of some ion species by reducing the work function of those species due to the low work function of cesium (~1.9 eV).[132]

Dual beam depth profiling can be operated in two different modes – non-interlaced or interlaced mode. With non-interlaced mode, analysis and sputtering are performed separately where complete interruption of analysis is followed by sputtering and vice versa.[132] This is how single beam depth profiling occurs. With interlaced mode, analysis and sputtering occur quasi-simultaneously, where the sputtering beam operates during the dead time of the analysis frame.[132,140] Here, the extractor is turned off during sputtering allowing for collected ions to drift to detection while not collecting any fragments from sputtering. With interlaced mode, experiment time is greatly reduced and the effects of residual gas (i.e. higher background counts) from constant analysis are reduced.[132] However, non-interlaced mode is preferred when the sample undergoes strong charging induced by the sputtering beam, given the lag time between sputtering and analysis.[132] In this work, data collected in **Chapter 3** for the OPVs as well as the work in **Section 4.3** on electrical degradation in perovskite films were performed in non-interlaced mode; whereas, the data in **Section 4.2** on light-induced degradation in perovskite devices were collected in interlaced mode. For our work conducted in non-interlaced mode, we were concerned about getting the flattest analysis plane possible (to keep depth resolution) – interlaced mode sputters as you analyze causing your image

plane to be tilted. For our work with interlaced mode, depth resolution was not as important as the time necessary for data collection.

2.1.3 Mixing-Roughness-Information (MRI) Model

To determine atomic or molecular mixing at buried interfaces in systems after ToF-SIMS depth profiling, we employ the mixing-roughness-information (MRI) model. In **Chapter 3**, an expanded description is given for use of the MRI model to extract short-range mixing in P3HT:dPCBM bilayers. And in **Chapter 4**, we use the MRI model as presented here to extract atomic/molecular mixing at the $MAPbI_3$/ITO interface after electrical degradation.

Considering an interface between two materials, the MRI model consists of three assumptions: (1) the real interface (that is, the intrinsic atomic/molecular mixing between the two materials following fabrication, described by a parameter w_0) will appear broader during depth profiling due to three fundamental factors: (a) sputtering induced mixing (described by a parameter w), (b) intrinsic and sputtering-induced corrugations (described in conjunction by a parameter σ) and (c) signal depth of origin (that is, the escape depth of the secondary ions, described by a parameter λ) at the regressing surface; (2) these three factors are independent from each other and (3) they can be described by analytical functions of depth whose convolution defines the so-called depth resolution function (DRF). Consequently, the real interface length (that is, the fabrication-induced atomic/molecular mixing length) can be extracted by deconvoluting the DRF from the measured interface length obtained by depth profiling (**Figure 2.3**).

At this stage, we emphasize a note of caution: atomic/molecular mixing and roughness cannot be completely disentangled. Within the MRI model, however, these two quantities are considered to be independent, thus one must clearly define the

roughness such that it is completely separated from atomic/molecular mixing. In this case, we define the roughness as the RMS roughness given by a scanning probe microscopy tool, i.e. AFM. More often, the roughness is measured before and after a depth profile through an interface.

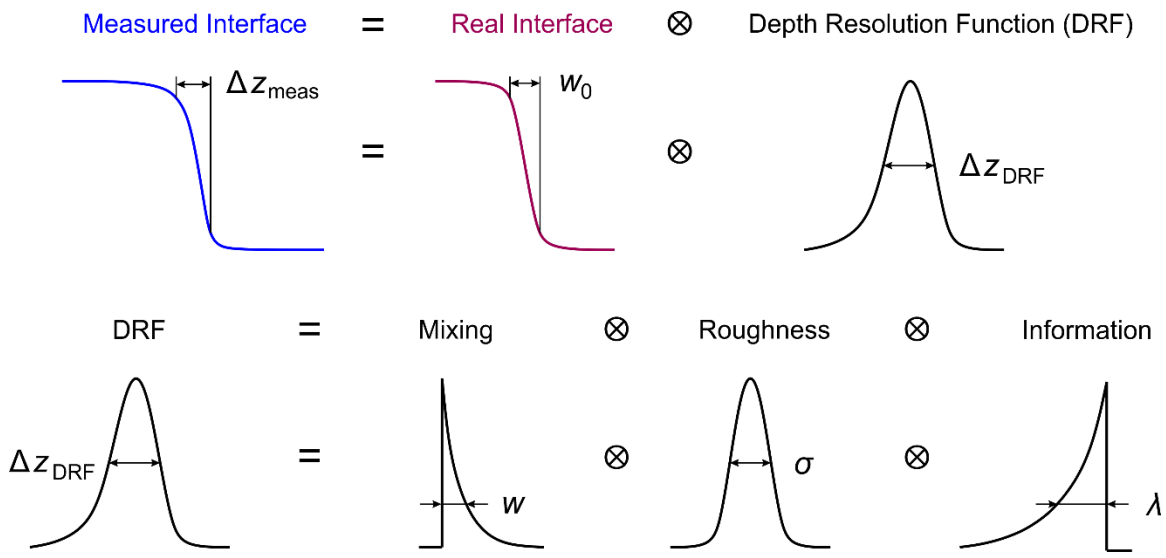

Figure 2.3 Mixing-Roughness-Information (MRI) model. A measured depth profile through a bilayer interface is the convolution of the real interface and the depth resolution function (DRF). The DRF is a convolution of three factors: mixing, roughness and information, discussed in the text.

Following the work of Hofmann[136,141,142] the functions representing the mixing, roughness and information factors can be written as:

$$g_w(z - z_0) = A_w \exp\left[-\frac{(z - z_0 + w)}{w}\right] \theta(z - z_0 + w) \tag{2.4}$$

$$g_\sigma(z - z_0) = A_\sigma \exp\left[-\frac{(z - z_0)^2}{2\sigma^2}\right] \tag{2.5}$$

$$g_\lambda(z - z_0) = A_\lambda \exp\left[\frac{(z - z_0)}{\lambda}\right] \theta(z_0 - z) \tag{2.6}$$

where z is the sputtered depth, z_0 is the running depth for which the contributions are calculated, A_w, A_σ and A_λ are some normalization constants such that $\int_{-\infty}^{\infty} dz\, g_{w,\sigma,\lambda}(z) = 1$, w, σ and λ are the mixing, roughness and information parameters, respectively, and $\theta(z)$ is the Heaviside step function (equal with 1 if $z \geq 0$ and 0 otherwise). The mixing and information parameters, w and λ, represent the length to which their respective contributions (g_w and g_λ, respectively) drop by a factor of $1/e$. The standard deviation of the corrugation contribution, g_σ, that is σ, represents the RMS of the corrugation at the z_0 plane. The DRF reads then:

$$g_{DRF}(z) = \int_{-\infty}^{\infty} dz' \int_{-\infty}^{\infty} dz''\, g_w(z' - z'') g_\sigma(z'') g_\lambda(z - z') \tag{2.7}$$

Finally, the normalized depth profile of a certain species (to the maximum secondary ion yield, I_0) can be written as:

$$\frac{I(z)}{I_0} = \int_{-\infty}^{\infty} dz' g_{DRF}(z' - z) \chi(z') \tag{2.8}$$

where $\chi(z)$ represents the species' *real* normalized (to its maximum) profile. For a given interface represented by the edge of the profile $I(z)$ (see **Figure 2.2**) the depth comprised between the 84.13 % and 15.87 % of the $I(z)$ edge height provides the measured interface length. Consequently, after the DRF deconvolution from $I(z)$, the depth comprised between the 84.13 % and 15.87 % of the resulting $\chi(z)$ edge provides the fabrication induced atomic/molecular mixing length (i.e. the *real* atomic/molecular mixing length, w_0). The 84 to 16 % levels are standard in the SIMS community but are meaningful only if the DRF is a Gaussian.[143]

To simulate a given interface, we use a forward calculation procedure[144], where we assume some starting values for the real atomic/molecular mixing, sputtering-induced mixing, roughness and information parameters and convolute the associated functions to obtain the simulated profile, which is then compared to the actual data points.

During the calculation of the simulated profile the normalized real interface is considered of sigmoid form,

$$\chi_s(z) = \left\{1 + \exp\left[2\ln\left(\frac{1}{0.1587} - 1\right)\frac{z}{w_0}\right]\right\}^{-1} \tag{2.9}$$

defined such that the depth between its 0.1587 and 0.8413 height levels is w_0, that is, the real atomic/molecular mixing length at the interface. Since both the DRF function and the simulated real interface, χ_s, are normalized to 1, the resulting simulated depth profile, $I_s(z)$, will also be normalized to unity:

$$I_s(z) = \int_{-\infty}^{\infty} dz' g_{DRF}(z' - z)\chi_s(z') \tag{2.10}$$

It is this simulated profile (**Equation 2.10**) that is compared to the actual data points, that is, the normalized depth profile (**Equation 2.8)**. Here, the fitting procedure minimizes the deviation between the simulated and actual profiles by using a genetic algorithm that optimizes all parameters sequentially in steps of ±0.1 nm from their starting values. In selecting starting parameters, it is important to select values which are physically meaningful and are in the neighborhood of the true values. Once a global minimum is found via the fitting procedure, the optimized values for the parameters (w_0, w, σ and λ) represent the values of their respective physical phenomenon, with the importance on the extracted intrinsic atomic/molecular mixing length.

2.2 INCORPORATING ATOMIC FORCE MICROSCOPY (AFM) WITH TOF-SIMS

Combining Atomic Force Microscopy (AFM) with ToF-SIMS takes advantage of AFM's high lateral resolution as well as the high chemical sensitivity and high depth resolution of ToF-SIMS. Basic AFM theory and the combination of the two techniques will be discussed here.

2.2.1 Tapping Mode AFM Basics

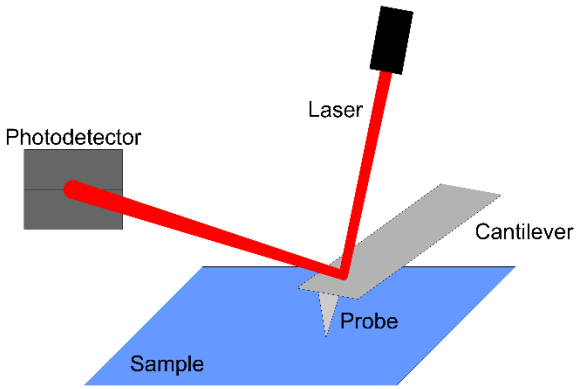

Figure 2.4 Basic AFM Set-up using Optical Level Method. A laser is reflected off the backside of a metal-coated cantilever near the attached probe. Changes in surface topography are recorded by changes in laser deflection on the photodetector.

Atomic Force Microscopy (AFM) is a technique used to measure surface topography and is part of a larger class of Scanning Probe Microscopy (SPM) techniques. With AFM, a sharp probe is raster scanned over a sample's surface and due to interactions between the probe and surface, a topography image is created. A basic set-up using an optical lever method is given in **Figure 2.4**. For operation, a probe, mounted on a thin cantilever, is brought into contact with the sample's surface and a laser is reflected off the backside of the cantilever near the probe onto a multi-quadrant photodetector. Vertical deflection of the laser beam on the photodetector maps out changes in height, due to changes in tip-sample interactions, as the probe is scanned over the surface. Probes

are typically made of silicon (Si) or silicon nitride (Si_3N_4) and the back of the cantilever is typically metal-coated in aluminum (Al).

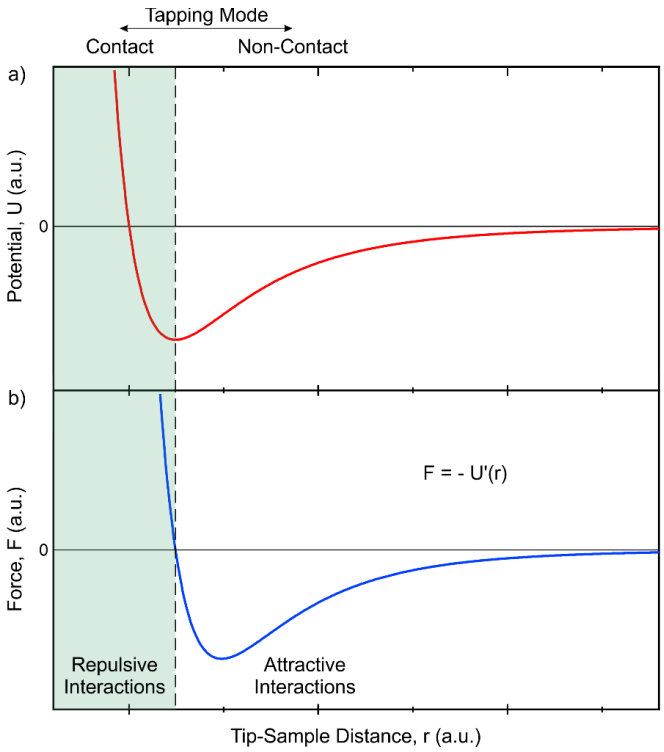

Figure 2.5 Tip-Sample interactions in AFM. (a) A general intermolecular potential as a function of tip-sample distance, *U(r)*, and associated (b) force curve depicting the regimes where repulsive interactions ($F > 0$) or attractive interactions ($F < 0$) dominate. Contact mode AFM occurs at distances where the tip and sample are in the repulsive region; non-contact mode AFM occurs at distances where attractive interactions dominate. Tapping mode AFM occurs at distances where tip-sample interactions fluctuate between repulsive and attractive.

AFM imaging commonly occurs in three modes corresponding to three force regimes of tip-sample interaction: contact mode, tapping (intermittent contact) mode, and non-contact mode. A generic intermolecular potential and associated force curve is given in **Figure 2.5**, showing the corresponding regions for each mode. Contact mode occurs

when the tip is in close contact to the surface and repulsive interactions dominate; conversely, non-contact mode occurs when the tip is relatively far away from the surface and attractive (van der Waals) interactions dominate. Tapping mode (or intermittent contact mode) occurs when the tip oscillates between the attractive and repulsive interaction regimes.

In tapping mode, an AC bias is applied to the cantilever causing it to oscillate near its resonance frequency, determining its free amplitude of oscillation. When the probe is near the surface, it oscillates between attractive and repulsive interactions with the surface, restricting its amplitude. A change in this amplitude as the probe is scanned and encounters regions of different height, causes a deflection of the laser beam. An electronic feedback loop (typically, a proportional-integral-derivative (PID) loop) moves the z-height of the tip to restore the previous amplitude and the height change is recorded, generating the topography map.

Tapping mode is a versatile mode. It exerts less force on the sample than contact mode allowing for imaging of softer materials such as polymers[62,114,145] as well as biological systems.[146,147] An added advantage of tapping mode is the ability to collect phase images, due to a shift in the phase angle of the AC driven oscillating cantilever as it encounters regions of different mechanical properties and thus different tip-sample interactions.[145,148,149] Phase imaging, specifically in polymer systems, has led to visualizing nanoscale material phase differences (i.e. amorphous versus crystalline phases) even when changes in topography are minimal.[62,114,145,149] It is also easier to use and faster than non-contact mode, which requires careful sample preparation and slow speeds to minimize surface contamination and measure only long-range van der Waals forces.[148,149] Lastly, it is a mode that can be used on samples in a number of media, including air[150] as well as liquids.[147,150]

2.2.2 ToF-SIMS/AFM

As discussed previously in this chapter, ToF-SIMS is a very powerful analytical technique capable of analyzing surface composition with high sensitivity and selectivity. Moreover, chemical imaging with ToF-SIMS can be done with moderate lateral resolution (~100 nm[132], although sub 100 nm resolution is possible[151]) Combining chemical imaging with depth profiling in the ToF-SIMS allows for building 3D chemical maps of a film with high depth resolution (<1 nm). However, in studies in which topography is important, ToF-SIMS fails to provide accurate information with regards to height and when sample feature sizes are smaller than the lateral resolution. Here is where AFM can add – in theory, AFM has atomic resolution, but even at more practical limits (nm),[146,149] its resolution is better than the ToF-SIMS. In addition, AFM provides height information that cannot be obtained from ToF-SIMS imaging.

The combination of ToF-SIMS/AFM is not new to our work – a select number of researchers have combined ToF-SIMS with AFM either *ex situ*[144,152–157] in air or *in situ*[158,159] within the ToF-SIMS chamber in vacuum. Progress with such combinations has been to understand the change in topography before and after SIMS sputtering[144,155,156,159] as well as to try and properly reconstruct chemical images with varying topography.[152–154,157,158] Most, if not all, of this work has been on systems with feature sizes greater than the lateral resolution of the SIMS allowing for easy correlation of images obtained by both methods. Previous to my work, my colleagues here at The University of Texas at Austin, have employed ToF-SIMS/AFM to determine both the chemical composition and the atomic/molecular mixing length at buried interfaces, including two-dimensional heterostructures[144] and atomic layer deposited (ALD) ultrathin films.[156] We will present an *ex situ* method in an inert (anoxic) atmosphere in order to

study buried morphologies in OPVs whose feature sizes are much less than the SIMS lateral resolution.

2.2.3 AFM in an Inert Atmosphere

For our measurements, in which *in situ* AFM was not possible, we performed AFM measurements in a glove box with an inert atmosphere of either nitrogen or argon gas. After sputtering in the ToF-SIMS, the sample surface can remain highly reactive either due to fragmentation/ionization of the surface material but also due to ion implantation from the analysis/sputtering beams. Exposure to air can cause surface oxidation and reorganization,[158] especially in organic systems. Early experiments with Drs. Andrei Dolocan and Raluca Gearba recognized the need for air-free sample transfer after ToF-SIMS sputtering as well as air-free AFM. Within minutes, surface topography can change when exposed to air. Placing an AFM in a glove box is non-trivial due to the need to remove vibrational background noise. Dr. Alex Veneman started the work of transferring our Veeco Digitial Instruments Dimension 3100 AFM into an Inert PureLab He glovebox. He applied Dynamat Xtreme to the outside of the glove box to minimize vibrations/noise from the box itself. Inside the glove box, the stage was place on a vibration isolation stage (Herzan TS-150). During operation of the AFM, it is sometimes necessary to turn the blower of the box down/off as well as turning off the vacuum pump to prevent unnecessary turbulence within the box. It is also important to minimize any physical contact with the box and to allow for plenty of equilibration after a disturbance before scanning. Fortunately, our box is used solely for scanning and no solvents are allowed inside since it does not have a catalyst; therefore, we do not worry about chemical corrosion of parts and we can use thinner gloves for placing samples/tips, which is extremely more difficult inside the box. To perform physical sample transfer between

the glove box and ToF-SIMS, we used an in-house, custom designed air-free capsule/interface.[160] Although, we mainly used nitrogen gas for the OPV experiments, the glove box can be filled with other inert gases for other reactive samples/systems (i.e. argon for lithium samples).

2.3 SUMMARY

ToF-SIMS, being highly selective and sensitive, provides chemical information with high depth resolution and modest lateral resolution. In systems with features or changes over the resolution capable with ToF-SIMS, that is the perovskite photovoltaic systems, ToF-SIMS alone visualizes the necessary chemical composition. When combined with AFM, it becomes a much more powerful methodology capable of providing the same chemical selectivity and sensitivity while also providing high lateral resolution topography information from the AFM. In systems where buried topographic information has lateral features less than the resolution of the ToF-SIMS or in which height information is important, that is, the OPV systems, combining the two techniques provides a way of visualizing buried morphologies as well as determining chemical composition at the buried planes. The rest of this dissertation will show how these techniques are crucial in understanding chemistry and morphology of buried interfaces in OPVs (**Chapter 3**) and in perovskite photovoltaic systems (**Chapters 4 and 5**).

Chapter 3: Investigating Buried Interfaces in Organic Photovoltaics (OPVs)†

3.1 INTRODUCTION

With the global energy requirements reaching new heights each year, we are in dire need of efficient, robust, environmental-friendly and affordable technologies that harvest alternative energy sources (e.g., solar, hydro, wind and geo-thermal). In particular, emerging photovoltaics, such as organic based solar cells, hold great promise for mainstream applications that demand competent cost/performance and stability criteria. Unfortunately, wide OPV adoption is hampered by relatively low efficiencies and stability problems, when compared to inorganic solar cells, demanding a better understanding of the active layer and its composing interfaces. On the positive side, markets that require specific properties can accelerate their deployment. For instance, organic photovoltaics with record efficiencies of 11.7%[14] can be printed on flexible substrates, have the ability to be transparent (6% efficient cells with 50% light transmission have been reported by Heliatek[161]) and are lightweight making them a front candidate for building integrated power solutions and portable devices.

Currently, the most progress in PCE has been achieved in polymer(donor):fullerene(acceptor) bulk heterojunctions (BHJs) by synthesizing polymers with low band gap[19–23] and optimizing the device morphology.[25–30] The "desirable" morphology is commonly attained by trial-and-error, employing a battery of preparation procedures that can include thermal[11,25,55] or solvent vapor[26,56,57] annealing, and choice of solvent,[29,58] rate of solvent removal,[59,60] relative volume fraction of the donor and acceptor,[29,30,61] and use of chemical additives.[27,28,62] However, these strategies

† Portions of this chapter were published in Griffin, M. P., Gearba, R., Stevenson, K. J., Vanden Bout, D. A., Dolocan, A. *J. Phys. Chem. Lett.* **2017**, *8*, 2764-2773 for which M. Griffin prepared the samples, carried out the measurements, analyzed and interpreted the data.

lead to complex and largely unknown morphologies that require detailed analysis with ultra-sensitive, spatially and chemically resolving tools. To date, extensive research on the BHJ structure and morphology has been performed on various systems, including poly (3-hexylthiophene-2-5-diyl): [6,6]-phenyl-C61-Butyric acid methyl ester (P3HT (donor):PCBM (acceptor)) blends, using an array of techniques such as x-ray scattering and diffraction,[71,162] transmission electron microscopy (TEM),[25,55,57,123,124] atomic force microscopy (AFM),[28,62] and neutron scattering and reflection,[67,115,163] none of which possess the simultaneous chemical and spatial sensitivity required to provide a clear correlation between energy conversion capabilities and compositional and morphological parameters essential for rational device optimization.

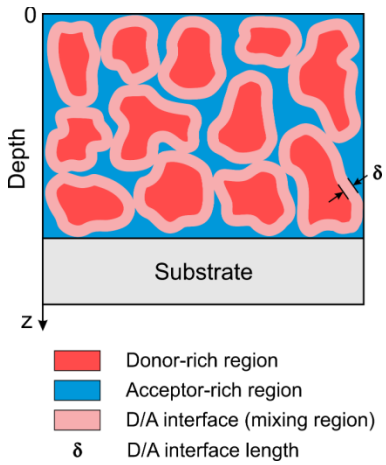

Figure 3.1 Schematic of a bulk heterojunction (BHJ) film. A BHJ film is composed of electron donor-rich (red) and acceptor-rich (blue) regions. In between these regions, the mixed, composite phase (pink color) represents the donor/acceptor (D/A) interface, with an average thickness defined by the length, δ.

Functionally, the common understanding in these systems is that phase segregation results in the formation of relatively pure donor (D) and acceptor (A)

nanometer size domains (**Figure 3.1**),[63,64] where light absorption mostly in the donor material creates excitons that dissociate into free charges at the D/A interface and the transport of the resulting free charges towards the electrodes occurs in the relatively pure domains. Recently, the presence of a third, intermixed (at molecular level) composite phase between the pure phases has been identified and there is compelling evidence that the extent of this mixed phase controls the charge separation and therefore the device efficiency.[64,66–73] Although this mixed phase represents the D/A interface, that is, the region between the relatively pure phases, it has never been properly identified as such nor studied in detail. So far, attempts at identifying and quantifying the mixed phase physical properties have provided estimates of the diffusion coefficients[64,67] between the BHJ components, and of the purities[14,64,71,72] and size distributions[64,66] of the relatively pure domains. However, these studies are unable to extract the detailed morphological signature of the mixed phase, namely the length of molecular mixing at the buried D/A interface, that is, the D/A interface length (**Figure 3.1**). To avoid any ambiguities, we spatially define the D/A interface length (or thickness) as the average of the shortest distances between the relatively pure donor and acceptor phases throughout the BHJ film, denoted hereafter as δ (**Figure 3.1**). This D/A interface length plays a crucial role in device operation, in particular controlling the exciton dissociation and subsequent free charge transport/recombination.

Since the ability to interrogate complex buried interfaces is currently the main hindrance in designing materials with improved performance, stability and lifetime, new state-of-the-art chemical imaging tools that combine both high spatial sensitivity and chemical selectivity are needed.[127] Previously, due to their ultra-high chemical sensitivity and selectivity, dynamic[67,126] (D-) and static[135,164] secondary ion mass spectrometry (SIMS – in particular time-of-flight SIMS, that is, ToF-SIMS), depth profiling have been

used to qualitatively demonstrate the long-range miscibility in multicomponent BHJs. Compared to D-SIMS, static SIMS operates in the so-called static SIMS regime, offering sub-nanometer depth resolution given the far weaker analysis ion beam currents.[144] However, identifying the D/A interface and measuring its length require precise measurement of both morphology and composition as functions of depth, which demands the addition of a topography-sensitive technique, such as scanning probe microscopy, to ToF-SIMS depth profiling. In this regard, we have previously demonstrated that, in conjunction with AFM, ToF-SIMS (in the static regime) can determine both the chemical composition and the atomic/molecular mixing length at buried interfaces, including two-dimensional heterostructures[144] and atomic layer deposited (ALD) ultra-thin films.[165] Such fundamental features are currently unavailable by applying TEM or scanning electron microscopy (SEM) with electron energy loss spectroscopy (EELS) or energy-dispersive X-ray spectroscopy (EDS) on cross-sectional samples,[122,165] given the intrinsically low chemical sensitivity and selectivity of these techniques when compared to SIMS. On the other hand, x-ray absorption and microscopy techniques[14,71,72,121,166] allow the identification of relatively pure phases of organic films, yet they lack the depth resolution while probing the whole thickness of the film. Consequently, while measuring some relative purities and domain sizes of the relatively pure phases, these techniques are unable to provide absolute concentrations of the BHJ composing species with depth, nor identify and extract a meaningful D/A interface length. Another very powerful technique, that is, neutron reflectivity (NR), is capable of chemically separating the BHJ composing materials with excellent depth resolution;[115,130] however, it does not provide the spatial sensitivity necessary for morphology or domain size identification.

Moreover, a direct visualization of the buried morphology in OPVs has not yet clearly been achieved, although attempts using TEM[25,114,123,124] and electron

tomography[123,125] have provided, arguably, indirect evidence of these complex morphologies. Other techniques, such as AFM,[28,62,114,115] have been employed to investigate the topography of various OPVs; however not as function of depth, therefore only probing the very top film morphology.

Here, we develop a robust, ultra-sensitive chemical imaging methodology that combines ToF-SIMS (in the static regime) and air-free (anoxic) AFM, together with depth profile modeling, to determine the chemical composition and morphology of a model polymer(D):fullerene(A) BHJ system, P3HT:PCBM, prior to and after thermal annealing, a post-preparation procedure known to substantially (however limited) increase the PCE by phase segregation.[25,63,64] Besides demonstrating the direct visualization of morphology as a function of depth, our approach is able to identify, locate and quantify the composing BHJ species throughout the film and gives access to fundamental morphology metrics, such as the molecular mixing length at the D/A interface, that is, the D/A interface length, a critical parameter for device performance. We show the annealing process creates partially mixed P3HT/PCBM domains that enhance exciton dissociation and free charge transport. Moreover, our results indicate these domains are in fact mostly mixed, allowing only for a small volume of pure P3HT to participate in the free charge transport, thus explaining the limited PCE improvement upon annealing.

3.2 CHEMISTRY AND MORPHOLOGY OF P3HT:PCBM BHJS

The proposed methodology is schematically depicted in **Figure 3.2**a, with *z* denoting the depth measured from the sample surface. ToF-SIMS depth profiling is used to investigate the chemical composition and expose select planes throughout the depth of the sample, which are further characterized by AFM, revealing the morphology of the

P3HT/PCBM buried interfaces. To separate the P3HT and PCBM ToF-SIMS signals, we chemically highlight the PCBM by employing isotope labeling, that is, we use deuterated PCBM (dPCBM).[67,122,167] **Figure 3.2**b,c present the ToF-SIMS depth profiles of a ~100 nm thick P3HT:dPCBM BHJ before and after thermal annealing for 30 minutes at 150°C, respectively. Specific secondary ion fragments, $^{34}S^-$ and $^{2}H^-$, representing P3HT and dPCBM, respectively, are used to monitor the relative chemical composition change in the BHJ upon thermal annealing. While in the unannealed case the P3HT and dPCBM signals are mostly constant throughout the film indicating a fully mixed blend (**Figure 3.1**b), long-range chemical segregation occurs within the annealed BHJ, with P3HT segregating mainly to the top and dPCBM to the middle of the film (**Figure 3.2**c). Chen *et al* have observed similar vertical segregation,[67] attributed to both phase segregation and favorable surface energy of either P3HT and PCBM with respect to the film surfaces.[115,168]

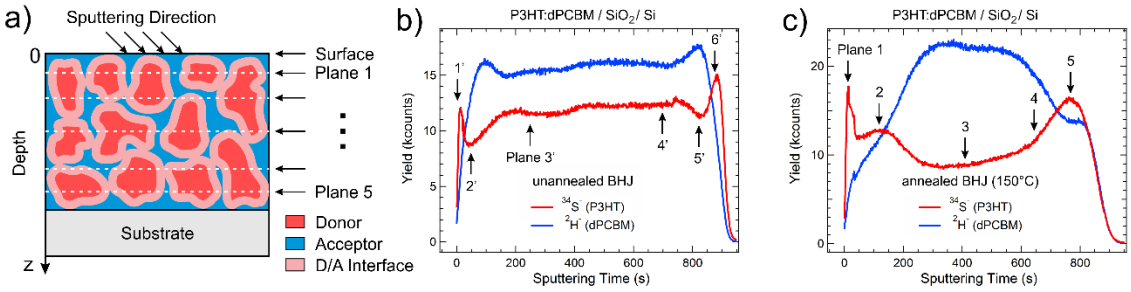

Figure 3.2 ToF-SIMS/AFM principle and depth profiles through P3HT:PCBM BHJs. (a) ToF-SIMS/AFM principle applied to a P3HT:PCBM BHJ. ToF-SIMS depth profiling is used to identify and reveal planes of chemical interest throughout the film while AFM is used to determine their morphology. The schematic indicates the D/A interface in pink. (b, c) ToF-SIMS depth profiles of $^{34}S^-$ and $^{2}H^-$ secondary ion fragments, representing P3HT and dPCBM, respectively, for unannealed (b) and fully annealed at 150°C for 30 minutes (c) P3HT:dPCBM BHJs. The profiles in (c) indicate the phase segregation in the BHJ upon annealing. The planes of interest indicated in the unannealed (b) and in the annealed (c) profiles are used in Figures 3.3 and 3.4, respectively.

AFM imaging at various depths, chosen to sample key points in the relative chemical composition change along the depth profile of the unannealed BHJ (**Figure 3.3**) indicate little change in morphology; whereas, in the annealed BHJ (**Figure 3.4**), suggests a dramatic morphology evolution with depth, with large structures appearing towards the bottom of the film. This provides, to our knowledge, the first direct visualization of the P3HT:PCBM BHJ morphology as function of depth.

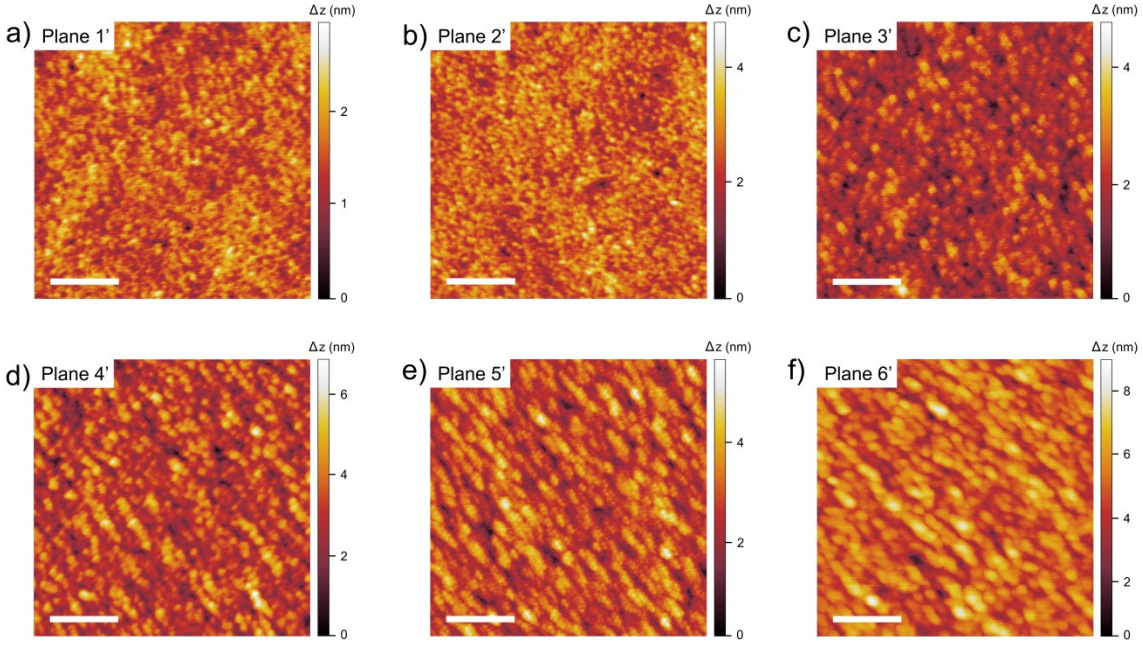

Figure 3.3 AFM topography images for the unannealed BHJ. (a-f) Images taken at the planes of interest indicated in Figure 3.2b, showing the unannealed BHJ morphology evolution as a function of depth. All AFM images are 1μm x 1μm; scale bars are 250 nm.

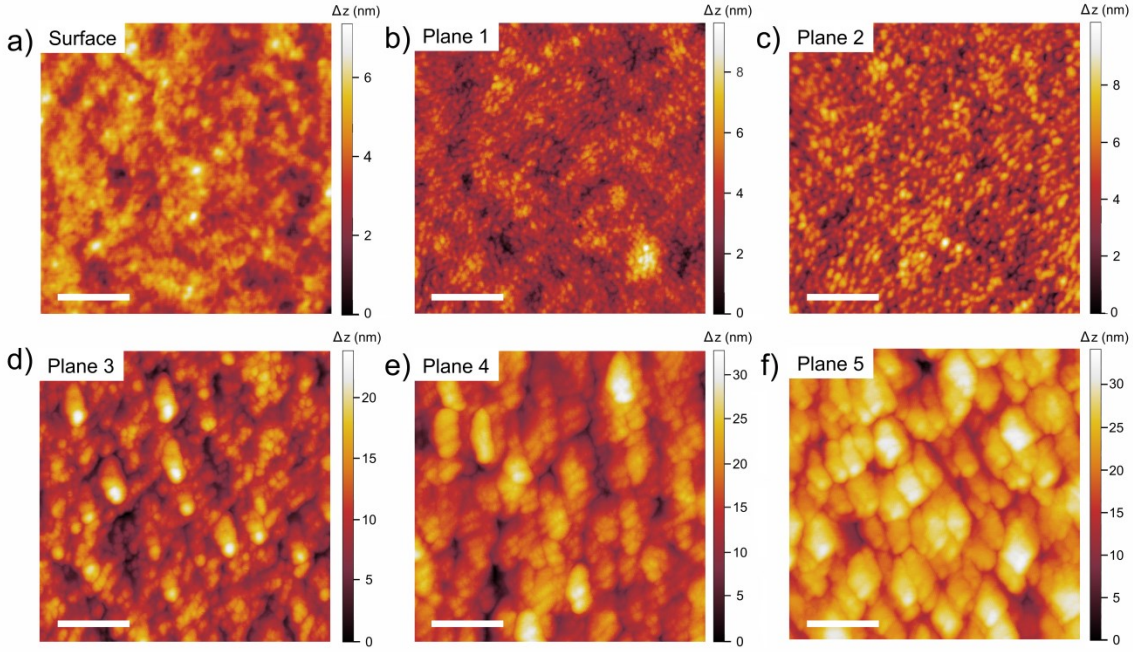

Figure 3.4 AFM topography images for the annealed BHJ. (a-f) Images taken at the planes of interest indicated in Figure 3.2c, showing the annealed BHJ morphology evolution as a function of depth. All AFM images are 1μm x 1μm; scale bars are 250 nm.

Morphologies obtained by AFM are often subject to qualitative interpretation and cannot infer chemical composition. To quantitatively compare the AFM maps recorded from different surfaces in a systematic way we employ image autocorrelation analysis (see **Section 3.2.1** for more details). Among other parameters, such as, the next nearest neighbor distance and the correlation length, the radially averaged autocorrelation of an image (that is, the radial autocorrelation) reveals the average domain size of the composing features (that is, the average particle distance). Most often, prior to autocorrelation analysis, an AFM image requires background subtraction to remove the vertical offset variations among its composing features, which are thus given a similar weight in the autocorrelation. **Figure 3.5**a shows two AFM topographic images acquired at similar depths (~75 nm, depths determined from method described in **Section 3.3**)

from two BHJs (unannealed and annealed) that were initially identically prepared (**Figure 3.2**b,c, **Figure 3.3**d, and **Figure 3.4**e). Depending on the amount of data smoothing (that is, consecutive horizontal and vertical line-by-line, pre-averaged spline interpolations) applied to an AFM image to generate the background used for subtraction, the radial autocorrelation of the resulting background-subtracted image is sensitive to either the fine (with less smoothing) or the large (with more smoothing) structures (**Figure 3.5**b and **Figure 3.6**). In the unannealed case, with no apparent large structures, we find a single radial autocorrelation per image regardless of the subtracted background smoothing, giving a relatively constant average domain size (~30 nm) with depth (**Figure 3.5**c, top). Based on the current understanding[55,64,71,169] and the depth profiles in **Figure 3.2**b, we consider these P3HT/dPCBM domains, defining the fine structure, to be fully mixed at the molecular level. In contrast, for the annealed BHJ, at larger depths, two radial autocorrelations can be obtained, one showing the fine structure increasing slightly to ~37 nm in domain size throughout the film, while the other demonstrating the formation of aggregates that expand strongly with depth, reaching >100 nm in size at the bottom of the film (**Figure 3.5**c, top). We attribute the slight increase in the fine structure size upon annealing to the partial P3HT crystallization[169,170] in the fully mixed domains observed in the unannealed BHJ. Given the virtually constant root mean square (RMS) corrugation (< 1 nm) measured throughout the unannealed film (**Figure 3.5**c, bottom), we conclude the sputtering conditions do not alter the film's intrinsic morphologies during depth profiling. That preferential sputtering does not affect the film's morphology and composition is also supported by both the flat profiles of P3HT and dPCBM in the unannealed BHJ (**Figure 3.2**b) and the decrease of the dPCBM signal towards the Si interface in the annealed BHJ (**Figure 3.2**c), in spite of the largely different sputtering rates (see **Section 3.2.2**). For the annealed blend, the corrugation has a larger initial offset

and increases strongly with depth, a result of the P3HT phase change and the aggregation process, respectively (**Figure 3.5**c, bottom).

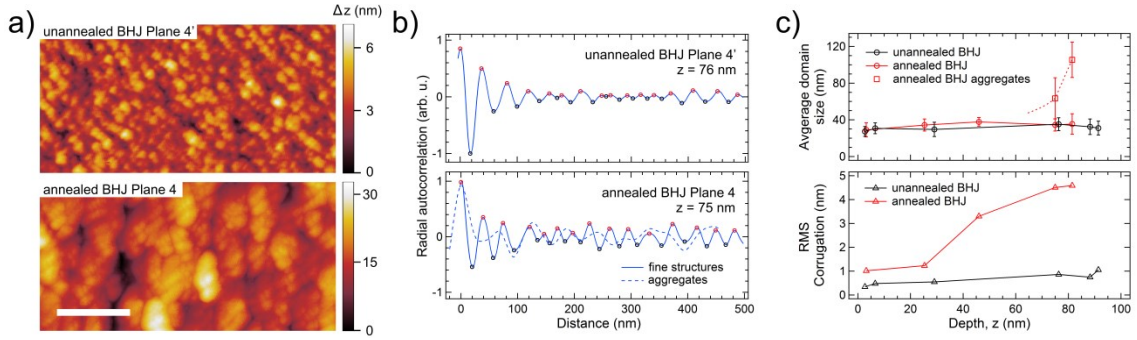

Figure 3.5 Domain sizes in unannealed and annealed BHJ. (a) AFM topography images for Plane 4' of the unannealed P3HT:dPCBM BHJ (top) and Plane 4 of the fully annealed BHJ (bottom) given in Figures 3.3d and 3.4e, respectively. Both planes are exposed at a vertical depth of ~75 nm from the surface of the BHJ film. Scale bar is 250 nm. (b) Radial autocorrelation distributions for Plane 4' of the unannealed BHJ (top) and Plane 4 of the annealed BHJ (bottom). Depending on the amount of initial smoothing applied to the AFM image of the annealed BHJ to generate the background used for subtraction, the radial autocorrelation of the resulting background-subtracted image provides the average size of either the small structures or the larger aggregates. (c) Calculated average domain size (that is, average particle distance) determined from the radial autocorrelations (top) and RMS corrugations (bottom) as a function of depth for the unannealed and annealed BHJ AFM images (Figures 3.3 and 3.4). The average aggregate size can only be extracted for the two deepest planes in the annealed BHJ (dotted line to guide eye). All depths were determined by the method outlined in Section 3.3.

3.2.1 Image Autocorrelation

The autocorrelation function for images is generated from the convolution of the two-dimensional image function with itself, $f(x,y)$:

$$f(x,y) \otimes f(x,y) = \int_{-\infty}^{\infty} \int_{-\infty}^{\infty} f(x',y') f(x'-x, y'-y)\, dx'\, dy' \qquad (3.1)$$

Image autocorrelation is able to extract domain sizes from data. To do image autocorrelation for domain size analysis, it is important to remove any vertical offsets, that is background, which can convolute with particle size in the correlation. To determine the background to remove reducing vertical offsets, we employed line-by-line x- and y-direction spline interpolations, having the effect of smoothing out the data. For "5-point smoothing," the spline interpolations pass through a number of equally spaced nodes determined by 5-point averaging of the data points. **Figure 3.6**a shows the AFM image for Plane 4' after background subtraction by 5-point smoothing. **Figure 3.6**b shows the image autocorrelation from the background subtracted image. Lastly, the radial distribution function is determined by taking the average of all points at discrete distances from the center of the image. From the radial distribution, the distance between the first peak and the second peak can be taken as the average domain size of the image. In the case of the annealed BHJ films where visible aggregates formed, a less averaged background subtraction (5-point) reveals the fine structure (**Figure 3.6**d-f) and a more averaged background subtraction (50-point) reveals the larger, aggregated structures (**Figure 3.6**g-i).

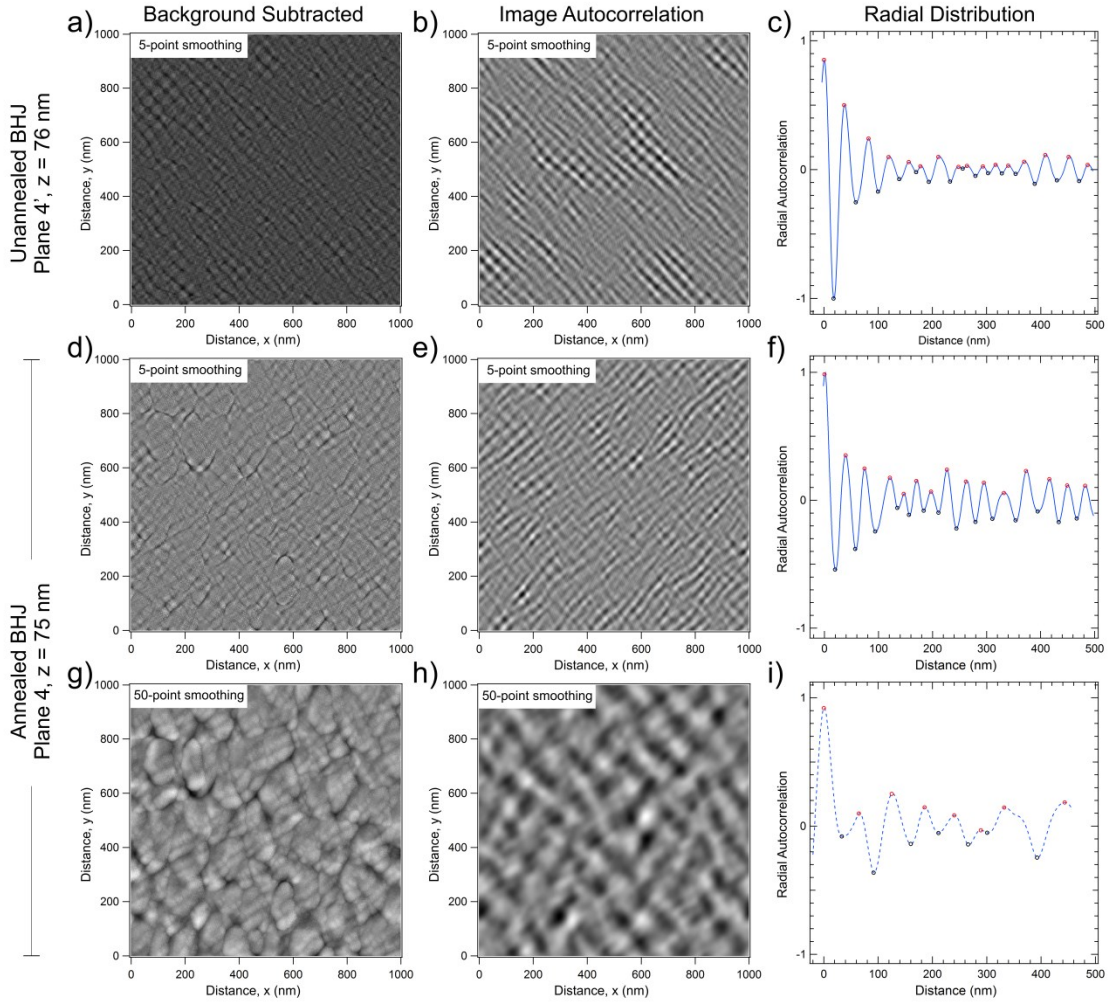

Figure 3.6 Image Autocorrelation. (a-c) Image autocorrelation analysis for the Plane 4' (z = 76 nm) AFM image of the unannealed BHJ. (a) The background subtracted image. (b) Image autocorrelation of the initial image with the 5-point-averaged interpolated background subtracted. (c) The corresponding radial distribution of the image autocorrelation in (b). (d-i) Image autocorrelation for the annealed Plane 4 (z = 75 nm) AFM image. (d-f) A less averaged background (line-by-line 5-point-averaged spline interpolation on both horizontal and vertical directions) subtraction reveals the BHJ fine structure. (g-i) In contrast, a more averaged background (line-by-line 50-point-averaged spline interpolation on both horizontal and vertical directions) subtraction reveals the larger, aggregated structures.

3.2.2 Sputtering Induced Morphology

One major issue when dealing with ToF-SIMS depth profiling is preferential sputtering due to different sputtering rates of the ablated compounds. This phenomenon induces a larger surface corrugation with sputtering time (that is, depth) and, as a result, changes in the real morphology with depth. Other side effects of this issue include loss of mass resolution (due to increased corrugation) and a continuous increase or decrease of a species' signal with depth (due to the loss of the material that sputters faster) depending on the species' lower or higher sputtering rate, respectively.

In our case, although we cannot completely rule out this effect, it does not influence the results. Preferential sputtering would affect the surface corrugation of the unannealed BHJ as much as for the annealed one since we expect P3HT and dPCBM to exhibit nanodomains in both cases. In other words, we expect the surface corrugation of the unannealed BHJ to increase significantly with sputtering time if preferential sputtering is severely affecting the surface morphology. Since we observe a minimal increase of corrugation with sputtering time (**Figure 3.5**c) for the unannealed BHJ, we think this effect is negligible. Another interesting observation is that for the unannealed BHJ both P3HT and dPCBM signals are mostly flat (**Figure 3.2**b) with sputtering time, which would not be the case if the preferential sputtering would be an issue. Even more, for the annealed BHJ although at first the signal of the dPCBM goes up while the one of P3HT down with sputtering time, towards the end of the profile the trend is reversed (**Figure 3.2**c), which is not consistent with preferential sputtering. If P3HT were preferentially removed with respect to dPCBM, we should see a continuous decrease in the P3HT signal with sputtering time and the opposite for the dPCBM.

Lastly, we collect all depth profiles in static SIMS mode, that is, with very low sputtering current (<1 pA) for the analysis beam (Bi_3^+). Simultaneously, we use a very

low energy (500 eV) for the sputtering beam (Cs^+), which was particularly chosen to minimize any sputtering effects. The sputtered samples are brought to the AFM in vacuum and AFM is performed under a nitrogen (N_2) environment, in a glove box, to minimize any effects from O_2 or H_2O on the sputtered surfaces. (See **Section 3.7.2** for more ToF-SIMS experimental details)

3.3 Depth and Concentration Conversion in Complex Binary Films

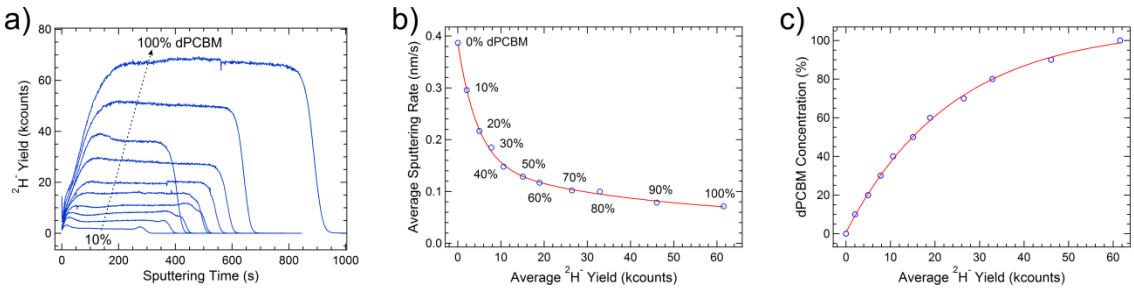

Figure 3.7 PCBM calibration depth profiles leading to depth and concentration conversion curves. Calibration depth profiles (a) for a series of P3HT:dPCBM unannealed BHJs (10%-100% dPCBM concentrations) leading to calibration curves that relate the average $^2H^-$ yield from a profile to a local, average sputtering rate (b) or to a dPCBM concentration (c).

Given the complexity of the sputtering process, especially for the annealed BHJ where the composing materials, P3HT and dPCBM, are unevenly mixed throughout the film (**Figure 3.2**c) and possess largely different sputtering rates, 0.4 and 0.07 nm/s, respectively, both converting sputtering time to depth and relating secondary ion signals to material concentrations are nontrivial. For this purpose, we record a series of depth profiles from BHJ blends that have known thicknesses and contain different weight fractions of P3HT and dPCBM spanning all combinations between 0 and 100% in discrete 10% steps (**Figure 3.7**a), to generate calibration curves that correlate the sputtering-time-averaged $^2H^-$ secondary ion yields in these blends with the average film

sputtering rates (**Figure 3.7**b) and the dPCBM concentrations (**Figure 3.7**c). A double exponential in **Figure 3.7**b and a single exponential in **Figure 3.7**c were empirically fit to the experimental data. For P3HT, similar curves were obtained using the $^{34}S^-$ signal (**Figure 3.8** in **Section 3.3.1**). The calibration curves are further applied to the depth profiles acquired from films containing *only* P3HT and dPCBM to convert the sputtering time to depth and to extract the absolute concentrations of P3HT and dPCBM with depth. For more complicated systems containing > 2 components, assuming each has a unique secondary ion marker, a similar calibration procedure can be employed that explores all compositional permutations among the composing materials.

3.3.1 Details on Conversion

The individual sputtering rates of P3HT and dPCBM, 0.4 and 0.07 nm/s, respectively, were calculated based on the thicknesses (determined ellipsometry) and the corresponding times needed to sputter through the respective pure films. To convert sputtering time into depth as well as extract the concentration (that is, weight percent) of P3HT and dPCBM throughout the film, we employ calibration curves. These curves are required to account for the nonlinear dependence between the sputtering rate of a binary blend containing materials with large differences in individual sputtering rates and the concentration of either one of the components. To solve this issue, we record a series of depth profiles from unannealed (**Figure 3.8**a,d) and annealed (**Figure 3.8**b,e) BHJ blends of known thickness containing different weight fractions of P3HT and dPCBM spanning all combinations from 0 to 100% in discrete 10% steps.

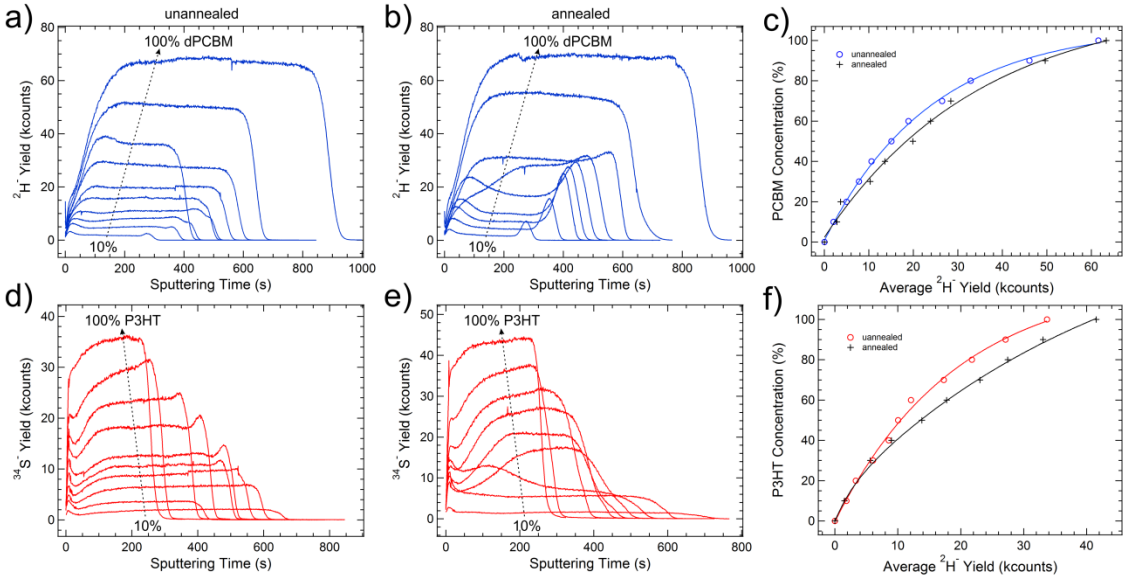

Figure 3.8 dPCBM and P3HT concentration calibration curves. (a-c) dPCBM calibration depth profiles for a series of P3HT:dPCBM unannealed (a) and annealed for 30mins at 150°C (b) BHJs (10%-100% dPCBM concentrations) leading to calibration curves relating the average $^2H^-$ yield in a profile to a dPCBM concentration (c); unannealed data in blue, annealed in black. (d-f) P3HT calibration depth profiles from the same series in (a,b) for the unannealed (d) and annealed (e) BHJs leading to calibration curves relating the average $^{34}S^-$ yield in a profile to a P3HT concentration (c); unannealed data in red, annealed in black. The annealed 20%:80% P3HT:dPCBM calibration sample was not used due to accidental contamination during annealing.

For depth conversion, we generate a calibration curve relating the sputtering-time-averaged $^2H^-$ ion yield, $\overline{I}$, to the average sputtering rate, $\overline{R}$, for each BHJ calibration sample. For clarity, the depth profile of a given secondary ion fragment is defined as the instantaneous ToF-SIMS yield of that fragment as a function of sputtering time, $I(t)$. We use the average $^2H^-$ signal since the depth profiles of the calibration films deviate, sometimes largely, from the pure rectangular shape. The average $^2H^-$ ion yield for each sample was calculated by integrating the $^2H^-$ yield, $I(t)$, over the sputtering time, t, and dividing it by the total sputtering time, $\Delta t = t_f - t_i$, determined as the difference

between the half-way points for the initial signal rise (at the surface, t_i) and final signal fall (at the silicon dioxide (SiO_2) interface, t_f):

$$\overline{I} = \frac{1}{\Delta t}\int_{t_i}^{t_f} dt\, I(t) \tag{3.2}$$

The average sputtering rate, $\overline{R}$, for a given film was calculated by dividing the film thickness, d, determined by ellipsometry, by the total sputtering time, Δt. The depth conversion calibration curve (**Figure 3.7**b) was determined from the unannealed calibration samples and empirically fit by a double exponential:

$$\begin{aligned}\overline{R} = 0.04512 + 0.10771 \exp\left(-2.3536 \times 10^{-5}\,\overline{I}\right) \\ +0.23455 \exp\left(-2.1964 \times 10^{-4}\,\overline{I}\right)\end{aligned} \tag{3.3}$$

For an arbitrary P3HT:dPCBM blend with a $^2H^-$ depth profile $I(t)$, the depth conversion until the SiO_2 interface assumes the instantaneous sputtering rate, $R(t)$, at a given sputtering time, t, corresponding to a sputtering depth $z(t)$, to be the average sputtering rate of a calibration blend, $\overline{R}$, that would give an average $^2H^-$ yield, $\overline{I}$, equal with the instantaneous $^2H^-$ yield at t, that is, $\overline{I} = I(t)$:

$$R(t) = \overline{R}[I(t)] = \frac{dz}{dt}\,, t_0 \le t \le t_{SiO_2} \tag{3.4}$$

where t_0 is the initial sputtering time and t_{SiO_2} is the sputtering time at the middle of the blend/SiO_2 interface. For $t > t_{SiO_2}$, since the depth conversion calibration curve is only defined for the blend, we use a sputtering rate model that assumes the instantaneous sputtering rate, $R(t)$, at the blend/SiO_2 interface as a linear combination of the individual sputtering rates:[135,136]

$$R(t) = \left|\frac{I(t)}{I(t_{SiO_2})}\right| R(t_{SiO_2}) + \left|\frac{I(t) - I(t_{SiO_2})}{I(t_{SiO_2})}\right| R_{SiO_2} = \frac{dz}{dt}, t > t_{SiO_2} \quad (3.5)$$

where $R_{SiO_2} = 0.15$ nm/s is the SiO_2 sputtering rate, which was calculated by completely sputtering a SiO_2 film with a known thickness (300 nm).

Thus, the sputtering depth, $z(t)$ corresponding to sputtering time, t, is expressed as:

$$z(t) = \int_{t_0}^{t} dt' R(t') \quad (3.6)$$

For concentration conversions, we relate the averaged $^2H^-$, (**Figure 3.8**c) or the average $^{34}S^-$ (**Figure 3.8**f) yields ($\bar{I}_{^2H}$ or $\bar{I}_{^{34}S}$, respectively) to the weight percent in the BHJ calibration samples. Four calibration curves were empirically fit to the data:

$$\bar{\rho}_{dPCBM,\,an} = 106.78 - 106.16 \exp\left(-4.1833 \times 10^{-5}\, \bar{I}_{^2H,an}\right) \quad (3.7)$$

$$\bar{\rho}_{dPCBM,\,un} = 119.03 - 116.71 \exp\left(-2.8527 \times 10^{-5}\, \bar{I}_{^2H,un}\right) \quad (3.8)$$

$$\bar{\rho}_{P3HT,\,an} = 158.34 - 11.563 \exp\left(-3.7171 \times 10^{-4}\, \bar{I}_{^{34}S,an}\right) - 146.92 \exp\left(-2.245 \times 10^{-5}\, \bar{I}_{^{34}S,an}\right) \quad (3.9)$$

$$\bar{\rho}_{P3HT,\,un} = 120.38 - 120.73 \exp\left(-5.1664 \times 10^{-5}\, \bar{I}_{^{34}S,un}\right) \quad (3.10)$$

where $\bar{\rho}_{dPCBM}$ and $\bar{\rho}_{P3HT}$ are the (weight percent) concentrations of the dPCBM and P3HT in the calibration films, respectively, for the annealed and unannealed samples (represented by the "an" and "un" subscripts, respectively). For an arbitrary P3HT:dPCBM blend with $^2H^-$ and $^{34}S^-$ depth profiles, $I_{^2H}(t)$ and $I_{^{34}S}(t)$, the complete concentration conversion assumes the instantaneous individual concentrations, $\rho_{dPCBM}(t)$ and $\rho_{P3HT}(t)$, at a given sputtering time, t, to be the concentrations of calibration blends,

$\overline{\rho}_{\mathrm{dPCBM}}$ or $\overline{\rho}_{\mathrm{P3HT}}$, that would give an average $^{2}H^{-}$ or $^{34}S^{-}$ yield equal with the instantaneous $^{2}H^{-}$ or $^{34}S^{-}$ yield at t, that is, $\overline{I}_{^{2}\mathrm{H}} = I_{^{2}\mathrm{H}}(t)$ and $\overline{I}_{^{34}\mathrm{S}} = I_{^{34}\mathrm{S}}(t)$:

$$\rho_{\mathrm{dPCBM}}(t) = \overline{\rho}_{\mathrm{dPCBM}}\left[I_{^{2}\mathrm{H}}(t)\right] \text{ and } \rho_{\mathrm{P3HT}}(t) = \overline{\rho}_{\mathrm{P3HT}}\left[I_{^{34}\mathrm{S}}(t)\right] \tag{3.11}$$

To account for the sputtering conditions slightly changing over time, we scale the $^{2}H^{-}$ and $^{34}S^{-}$ profiles by factors (around unity) before applying both the depth and concentration conversions, which ensures the data conversions are physically correct. For example, in the unannealed bilayer case, we know that each layer contains at most 100% material; therefore, the corresponding profiles are scaled such that the concentrations for each layer would not exceed 100%. Further, these factors are used to scale the $^{2}H^{-}$ and $^{34}S^{-}$ profiles of all the annealed bilayers that were recorded in the same day with the unannealed BL. For the 50%:50% dPCBM:P3HT BHJs, we calculate the scaling factors such that they give 50% concentrations for each component after the concentration conversion in the middle of the unannealed BHJ. Similar to the BL case, we use these factors to scale the annealed BHJ data acquired in the same day with the unannealed BHJ. The factors vary but are reasonably close to unity which proves the sample preparation and sputtering conditions do not change but minimally over time.

3.4 ANNEALED BILAYERS (BLS) TO MIMIC ANNEALED BHJS

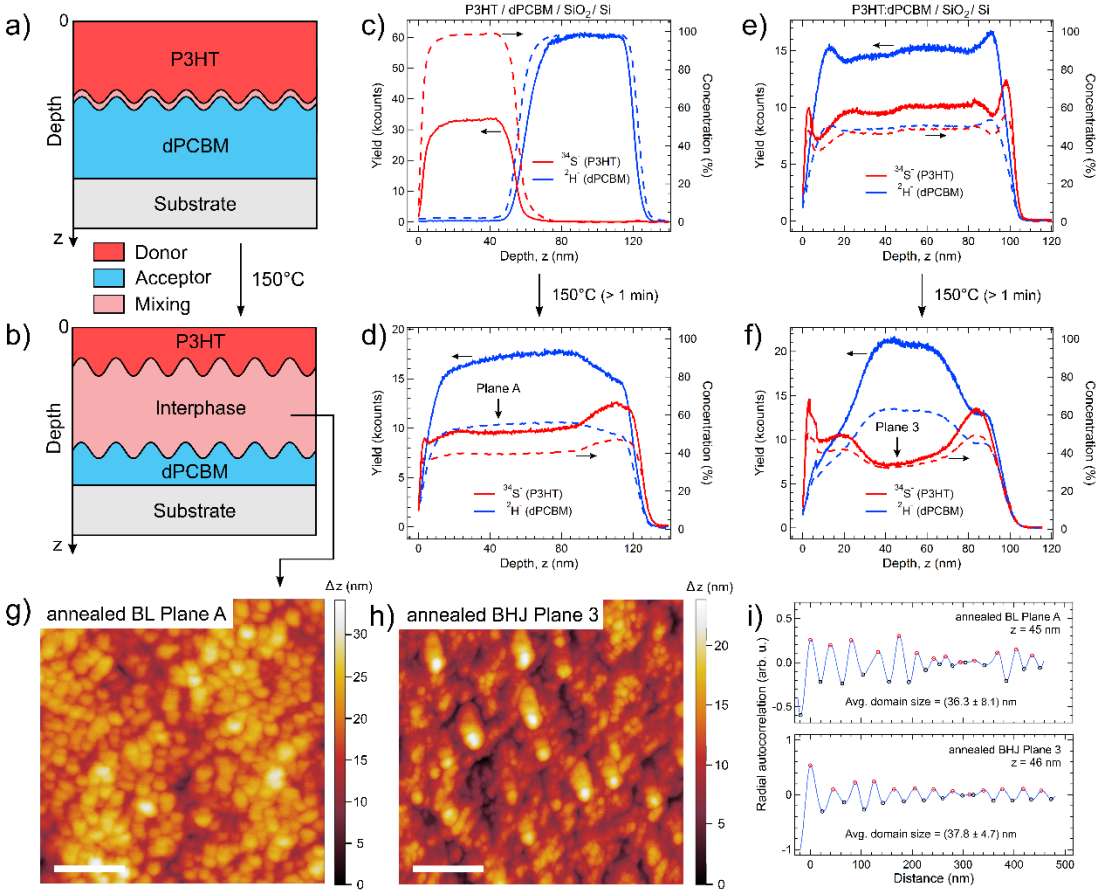

Figure 3.9 Annealed bilayers (BLs) mimicking annealed BHJs. (a, b) Schematic of the unannealed (a) and partially annealed (b) P3HT/dPCBM BLs. The annealing time controls the interphase length between the P3HT and dPCBM pure films. (c, d) ToF-SIMS depth profiles of $^{34}S^-$ and $^2H^-$ secondary ion fragments (continuous curves) and corresponding P3HT and dPCBM concentrations (dashed curves), respectively, for the unannealed (c) and fully annealed for 10 minutes at 150°C (d) P3HT/dPCBM BLs. (e, f) ToF-SIMS depth profiles of $^{34}S^-$ and $^2H^-$ secondary ion fragments and corresponding P3HT and dPCBM concentrations, respectively, for the unannealed (e) and fully annealed for 30 minutes at 150°C (f) P3HT:dPCBM BHJ. (g, h) Comparison between the AFM topography images at Plane A of the annealed BL (g) and Plane 3 of the annealed BHJ (h). Both planes are located at a depth of ~45 nm. Scale bars are 250 nm. (i) Radial autocorrelation distributions for Plane A of the annealed BL (top) and Plane 3 of the annealed BHJ (bottom) showing similar domain sizes.

Our working hypothesis is that during annealing, when the BHJ undergoes long-range (that is, throughout the film) chemical speciation and mixing, and phase segregation consisting of simultaneous P3HT crystallization and partial dPCBM demixing in the fine structure, short-range mixed regions are generated at the edges of the annealed domains (that is, the D/A interface, represented by the pink regions in **Figure 3.1** and **Figure 3.2**a). To verify and quantify the extent of this local, short-range mixing we employ a model system, that is, a P3HT/dPCBM bilayer (BL) with equally thick (~60 nm) pure films, prepared using a method previously described by Russell and co-workers,[167] which ensures the initial interface between P3HT and PCBM is molecularly sharp (< 1 nm). By controlling the BL interface morphology through precisely timed thermal annealing at 150°C, we are able to physically simulate the annealed BHJ morphology and, intrinsically, its short-range mixing, within a variable depth at the P3HT/dPCBM interface (**Figure 3.9**a-f). That the interphase produced by annealing the BL (**Figure 3.9**b) has a similar morphology with the annealed BHJ is demonstrated in **Figure 3.9**g-i, where the morphologies of two buried planes (at ~45 nm depth) in the BL (Plane A) and BHJ (Plane 3) are compared through radial autocorrelation, yielding virtually identical domain sizes (~37 nm). Additionally, we note similar chemical segregation trends of the P3HT and dPCBM signals in both annealed BL and BHJ films (**Figure 3.9**d,f). Moreover, device performance analysis demonstrates the PCE of an annealed BHJ formed starting from a bilayer made via the preparation method of Russel and co-workers is similar to the PCE of an annealed BHJ formed starting from spincoated P3HT:PCBM (50%:50%) mixed solution.[167] Finally, the calibration curves in **Figure 3.7**b,c and **Figure 3.8** are used to convert the sputtering time to depth and the $^{34}S^-$ and $^{2}H^-$ secondary ion yields to P3HT and dPCBM absolute concentrations, respectively (**Figure 3.9**c-f). This allows for a direct, quantitative

comparison between the chemical species throughout the films, showing the near perfect mixing in the unannealed (**Figure 3.9**e) and the long-range segregation in the annealed (**Figure 3.9**f) BHJs.

3.5 CALCULATING EXTENT OF MIXING FROM BILAYER INTERPHASE

Intrinsically, the interface between the two composing organic materials of a BL is defined by a molecular mixing region that follows the interface corrugation resulting from fabrication (**Figure 3.9**a). Upon annealing, the P3HT/PCBM mixed region expands with annealing time, creating an interphase that resembles the annealed BHJ (**Figure 3.9**b). Complete BL mixing can be achieved after a few minutes of annealing at 150°C (**Figure 3.9**c,d). However, if the annealing is incomplete the BL maintains two regions of pure material that form two short-range mixing regions with the interphase (**Figure 3.10**a). Since we expect the molecular mixing to occur at the boundaries of the domains composing the fine structure, the annealed BL interphase morphology should consist of core-shell spheroidal nanostructures that contain a core-like crystalline P3HT and a shell-like P3HT/PCBM mixed region (**Figure 3.10**b), similar with the morphology of the annealed BHJ.

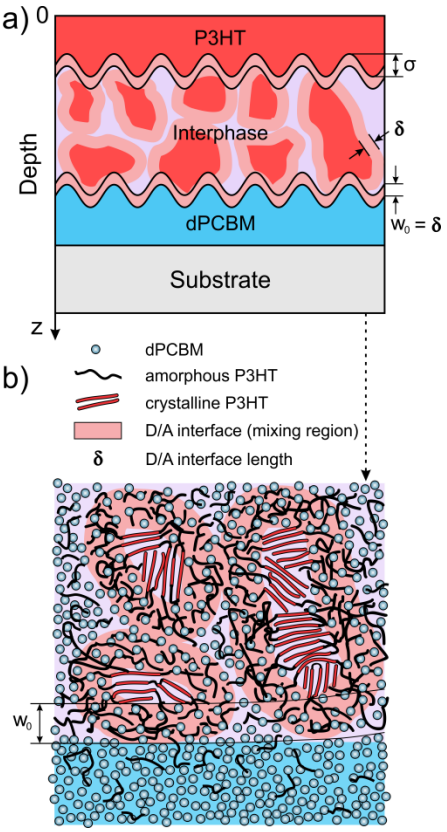

Figure 3.10 Schematic of partially annealed BL with a molecular picture of the mixed interphase. (a) Schematic of the partially annealed P3HT/dPCBM BL depicting the pure dPCBM (blue), relatively pure dPCBM (purple), pure P3HT (red) and mixing (pink) regions in the interphase. The mixing region represents the D/A interface. Its length (or thickness), δ, can be identified and quantified by measuring the real interface mixing length w_0 at the P3HT:dPCBM interphase / pure dPCBM interface. σ represents the variable RMS of the corrugation at the regressing surface. (b) Schematic of the interphase/pure dPCBM interface showing the detailed molecular picture of mixing between P3HT and dPCBM.

Figure 3.11a-c demonstrate partial BL annealing, where one second and, further, 10 seconds of annealing at 150°C cause diffusion of a limited amount of dPCBM throughout the P3HT layer and incomplete diffusion of P3HT into the dPCBM layer, as indicated by the $^{2}H^{-}$ signal reaching the top and the $^{34}S^{-}$ signal not reaching the bottom of the film, respectively. The latter observation opens up the possibility of measuring, via

the $^{34}S^-$ profile, the short-range P3HT/dPCBM mixing length in the core-shell nanostructures, that is, δ, at the interface between the interphase and the remaining pure dPCBM layer, as outlined in **Figure 3.10**. To estimate this short-range mixing length, that is, the D/A interface length, δ, we employ the mixing-roughness-information (MRI) model,[142,144] which describes the sputtering effects during depth profiling and can be used to simulate the profile of an interface. Considering an interface between two materials, the MRI model consists of three assumptions: (1) the real interface (that is, the intrinsic atomic/molecular mixing between the two materials following fabrication, described by a parameter w_0) will appear broader during depth profiling due to three fundamental factors: (a) sputtering induced mixing (described by a parameter w), (b) intrinsic and sputtering-induced corrugations (described in conjunction by a parameter σ) and (c) signal depth of origin (that is, the escape depth of the secondary ions, described by a parameter λ) at the regressing surface; (2) these three factors are independent from each other and (3) they can be described by analytical functions of depth whose convolution defines the so-called depth resolution function (DRF). Consequently, the real interface length (that is, the fabrication-induced atomic/molecular mixing length), w_0, can be extracted by deconvoluting the DRF from the measured interface length obtained by depth profiling (**Figure 3.13** and **Section 3.5.1**). Applying this model to our case, for a partially annealed BL, allows measuring the real interface length, w_0, between the interphase and remaining pure dPCBM layer, which essentially gives the P3HT/dPCBM D/A interface length, δ (**Figure 3.10**).

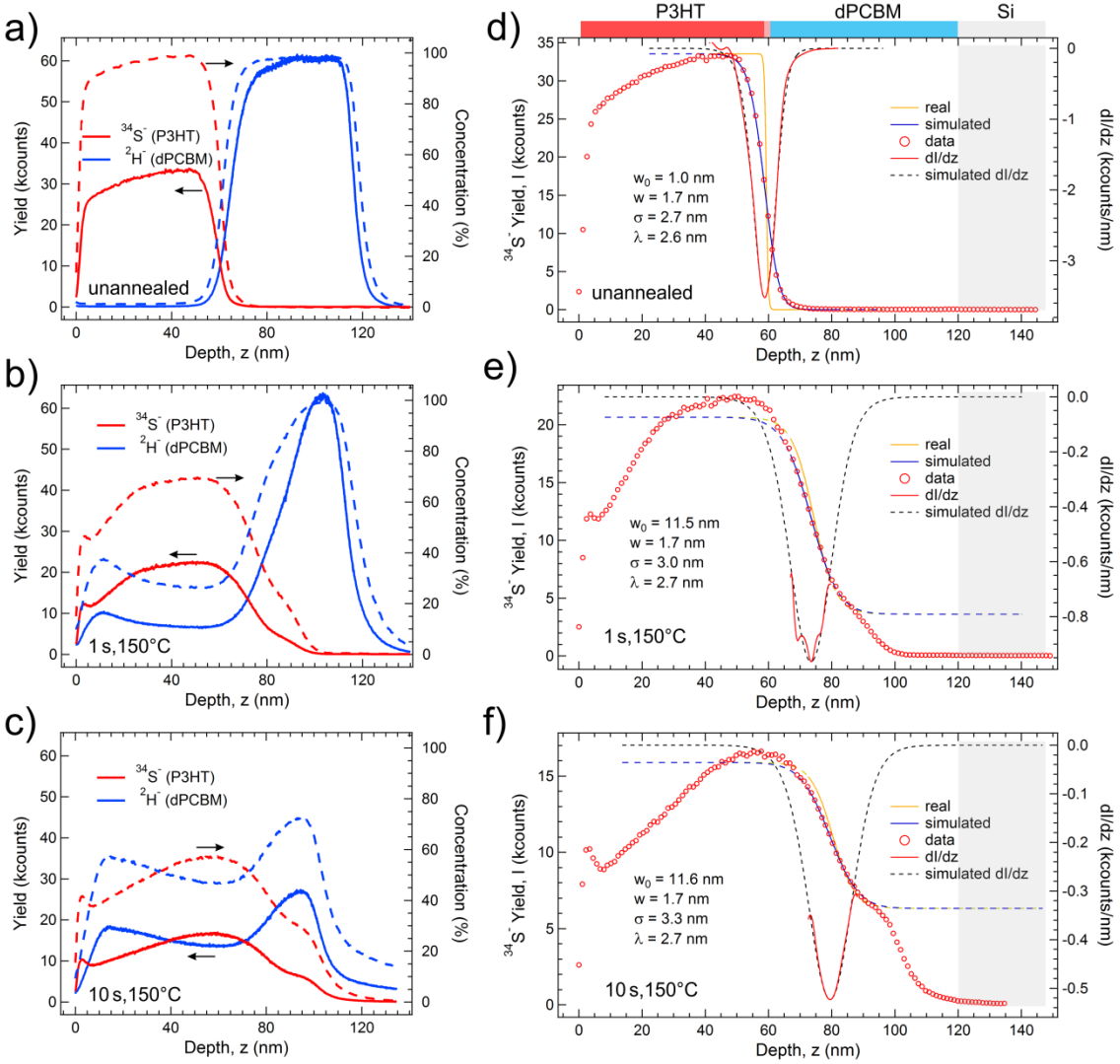

Figure 3.11 ToF-SIMS depth profiles and MRI modelling of annealed BLs. (a – c) ToF-SIMS depth profiles of $^{34}S^-$ and $^2H^-$ and corresponding P3HT and dPCBM calculated concentrations, respectively, for the unannealed (c), flash annealed for 1 second at 150°C (d) and flash annealed for 10 seconds at 150°C (e) P3HT/dPCBM BLs. (d – f) The evolution of the molecular mixing at the P3HT/dPCBM interface following annealing can be extracted from the $^{34}S^-$ profile. The D/A interface length plateaus at ~11.5 nm after 1 second of annealing. The fitting procedure is discussed in this section and Section 3.5.1.

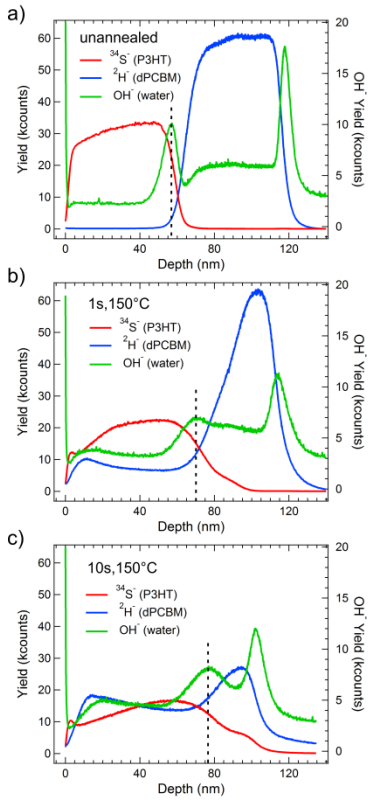

Figure 3.12 Locating the BL interfaces. (a-c) ToF-SIMS depth profiles of $^{34}S^-$ (P3HT), $^2H^-$ (dPCBM) and OH^- (water) for the (a) unannealed, (b) flash annealed for 1 second at 150°C and (c) flash annealed for 10 seconds at 150°C P3HT/dPCBM BLs. The residual water trapped at the BL interface follows its location upon annealing. Consequently, the vertical dotted lines (representing the water signal peak position) indicate either the P3HT/dPCBM interface in the unannealed BL or the P3HT:dPCBM interphase/dPCBM interface in the partially annealed BLs.

To simulate the P3HT/dPCBM interface in the unannealed BL and the P3HT:dPCBM interphase/dPCBM interfaces in the partially annealed BLs, we use the forward calculation procedure,[142,144] where we assume some starting values for the real atomic mixing, sputtering-induced mixing, roughness and information parameters and convolute the associated functions to obtain the simulated profile, which is then fit to the actual $^{34}S^-$ data points (**Figure 3.11**d-f). Since annealing causes the physical migration

and broadening of the interfaces, we use the residual water signal, represented by the OH^- secondary ion fragment, to track their locations (**Figure 3.12**).

Notably, the concentration curves of P3HT (obtained by converting the $^{34}S^-$ profiles via the calibration curve in **Figure 3.8**f) and the corresponding $^{34}S^-$ profiles are almost identical at the P3HT/dPCBM interfaces, when represented on the same scale, implying a minimal matrix effect (**Figure 3.11**a-c and **Figure 3.14** in **Section 3.5.2** and text in **Section 3.5.2**). Also, as the these interfaces have arbitrary baselines in the depth profiles once the materials start mixing, we match both the $^{34}S^-$ yield (denoted as I) and its first derivative (dI/dz) at the inflection point with the corresponding values of the simulated curve. The fitting procedure minimizes the deviation between the simulated and $^{34}S^-$ profiles by using a genetic algorithm that optimizes all parameters sequentially in steps of ±0.1 nm from their starting values (see **Section 3.5.1**). In **Figure 3.11**d, since minimal molecular mixing is expected for the unannealed BL, constraining w_0 to 1 nm gives, besides a reasonable RMS corrugation (σ = 2.7 nm), the w and λ parameters that are specific to our samples and sputtering conditions and that are further used to fit the partially annealed BLs. The resulting simulated profiles reveal a similar P3HT/dPCBM short-range mixing length ($\delta = w_0 \cong$ 11.5 nm) for both 1-s and 10-s annealed BLs (**Figure 3.11**e,f), demonstrating that the annealed D/A interface is produced in a matter of seconds and does not evolve with annealing time.

3.5.1 MRI Model for P3HT/dPCBM Bilayers

In this section, we take the basic principles of the MRI model, presented in this chapter as well at **Section 2.1.3**, and adapt them to our P3HT/PCBM bilayers. Because the annealed bilayer depth profiles have arbitrary base lines (i.e. normalization would distort the data), it is necessary to vertically scale and horizontally shift the simulated

depth profiles in order to compare them to the actual depth profiles. This process is shown in the text corresponding to **Equations 3.19 - 3.22** below. Much of this chapter is duplicated from **Section 2.1.3** for ease and clarity of understanding in this section.

The mixing-roughness-information (MRI) model was employed to determine the molecular mixing, that is, the short-range mixing length, at the P3HT:dPCBM interphase/dPCBM interface following TOF-SIMS depth profiling of the annealed BLs.[136,141,142,165] Considering an interface between two materials, the MRI model consists of three assumptions: (1) the real interface (that is, the intrinsic atomic/molecular mixing between the two materials following fabrication, described by a parameter w_0) will appear broader during depth profiling due to three fundamental factors: (a) sputtering induced mixing (described by a parameter w), (b) intrinsic and sputtering-induced corrugations (described in conjunction by a parameter σ) and (c) signal depth of origin (that is, the escape depth of the secondary ions, described by a parameter λ) at the regressing surface; (2) these three factors are independent from each other and (3) they can be described by analytical functions of depth whose convolution defines the so-called depth resolution function (DRF). Consequently, the real interface length (that is, the fabrication-induced atomic/molecular mixing length) can be extracted by deconvoluting the DRF from the measured interface length obtained by depth profiling (**Figure 3.13**).

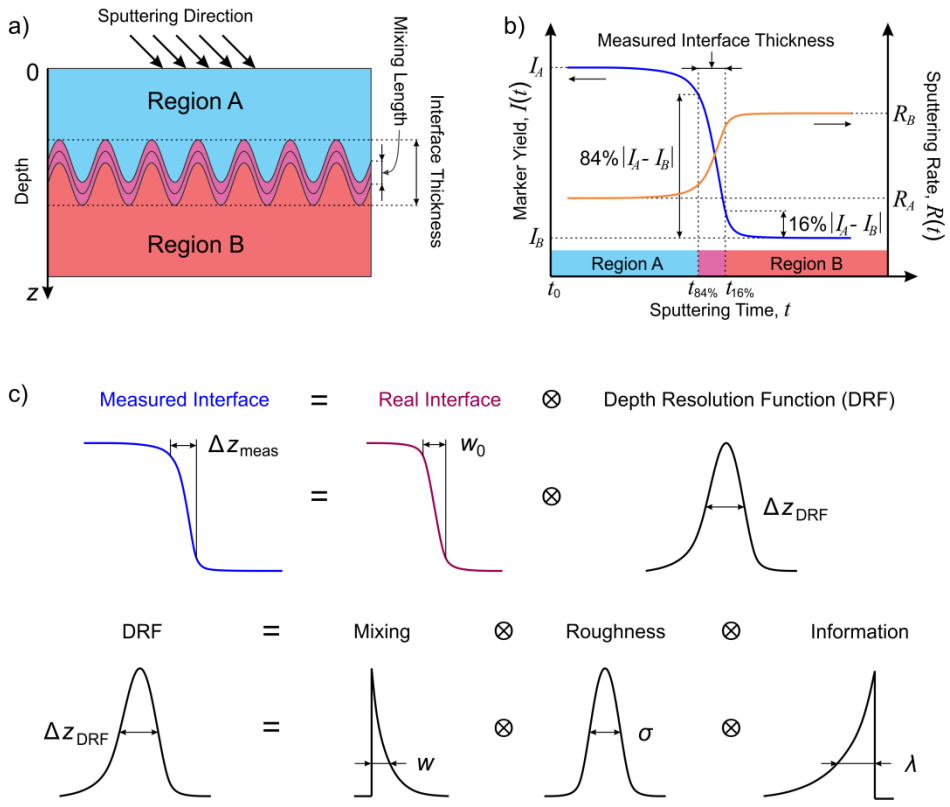

Figure 3.13 MRI model. (a) Schematic of an interface between two materials, A and B, that consists of atomic mixing and corrugation, the latter represented here by the RMS of the roughness. (b) Depth profiling through such interface adds sputtering effects that, together with corrugation, can be deconvoluted from the measured interface length to give the atomic mixing length. (c) Mixing roughness information (MRI) model: the measured profile of a secondary ion fragment is a convolution between the real profile and a depth resolution function (DRF) that accounts for sputtering induced and corrugation effects.

At this stage, we emphasize a note of caution: atomic mixing and roughness cannot be completely disentangled. Within the MRI model, however, these two quantities are considered to be independent, thus one must clearly define the roughness such that it is completely separated from atomic mixing. In this case, we define the roughness as the

RMS roughness given by a scanning probe microscopy tool, i.e. AFM. More often the roughness is measured before and after a depth profile through an interface.

Following the work of Hofmann[136,141,142] the functions representing the mixing, roughness and information factors can be written as:

$$g_w(z - z_0) = A_w \exp\left[-\frac{(z - z_0 + w)}{w}\right] \theta(z - z_0 + w) \tag{3.12}$$

$$g_\sigma(z - z_0) = A_\sigma \exp\left[-\frac{(z - z_0)^2}{2\sigma^2}\right] \tag{3.13}$$

$$g_\lambda(z - z_0) = A_\lambda \exp\left[\frac{(z - z_0)}{\lambda}\right] \theta(z_0 - z) \tag{3.14}$$

where z is the sputtered depth, z_0 is the running depth for which the contributions are calculated, A_w, A_σ and A_λ are some normalization constants such that $\int_{-\infty}^{\infty} dz\, g_{w,\sigma,\lambda}(z) = 1$, w, σ and λ are the mixing, roughness and information parameters, respectively, and $\theta(z)$ is the Heaviside step function (equal with 1 if $z \geq 0$ and 0 otherwise). The mixing and information parameters, w and λ, represent the length to which their respective contributions (g_w and g_λ, respectively) drop by a factor of $1/e$. The standard deviation of the corrugation contribution, g_σ, that is σ, represents the RMS of the corrugation at the z_0 plane. The DRF reads then:

$$g_{DRF}(z) = \int_{-\infty}^{\infty} dz' \int_{-\infty}^{\infty} dz''\, g_w(z' - z'') g_\sigma(z'') g_\lambda(z - z') \tag{3.15}$$

Finally, the normalized depth profile of a certain species (to the maximum secondary ion yield, I_0) can be written as:

$$\frac{I(z)}{I_0} = \int_{-\infty}^{\infty} dz' g_{DRF}(z' - z)\, \chi(z') \tag{3.16}$$

where $\chi(z)$ represents the species' *real* normalized (to its maximum) profile. For a given interface represented by the edge of the profile $I(z)$ (see **Figure 3.13**) the depth comprised between the 84.13 % and 15.87 % of the $I(z)$ edge height provides the measured interface length. Consequently, after the DRF deconvolution from $I(z)$, the depth comprised between the 84.13 % and 15.87 % of the resulting $\chi(z)$ edge provides the fabrication induced atomic mixing length (i.e. the *real* atomic mixing length, w_0). The 84 to 16 % levels are standard in the SIMS community but are meaningful only if the DRF is a Gaussian.

To simulate the P3HT/dPCBM interface in the unannealed BL and the P3HT:dPCBM interphase/dPCBM interfaces in the partially annealed BLs, we use the forward calculation procedure,[144] where we assume some starting values for the real atomic mixing, sputtering-induced mixing, roughness and information parameters and convolute the associated functions to obtain the simulated profile, which is then fit to the actual $^{34}S^-$ data points. We choose the $^{34}S^-$ depth profile to represent the BL interfaces since 1 second and 10 seconds of annealing show incomplete diffusion of P3HT into the dPCBM layer (**Figure 3.11**a-c), which opens up the possibility of measuring the short-range P3HT:dPCBM mixing length in the core-shell nanostructures at the interface between the interphase and the remaining pure dPCBM layer (**Figure 3.10**b). During the calculation of the $^{34}S^-$ simulated profile the normalized real interface is considered of sigmoid form,

$$\chi_s(z) = \left\{1 + \exp\left[2\ln\left(\frac{1}{0.1587} - 1\right)\frac{z}{w_0}\right]\right\}^{-1} \tag{3.17}$$

defined such that the depth between its 0.1587 and 0.8413 height levels is w_0, that is, the real molecular mixing length at the P3HT/dPCBM BL interface. Since both the DRF function and the simulated real interface, χ_s, are normalized to 1, the resulting simulated depth profile, $I_s(z)$, will also be normalized to unity:

$$I_s(z) = \int_{-\infty}^{\infty} dz' g_{DRF}(z' - z)\, \chi_s(z') \tag{3.18}$$

Moreover, the z axis in eq. (12) is arbitrarily defined, with χ_s, and therefore I_s, centered around $z = 0$. As a result, in order to fit the simulated profile, $I_s(z)$, to the actual $^{34}S^-$ profile, $I(z)$, which is not generally normalized and has a fixed, well defined z axis, the simulated profile has to be both vertically-expanded (along the yield axis) and horizontally-offset (along the z axis) to fit the data correctly. For this, we assume a linear vertical expansion,

$$I(z) = \alpha\, I_s(z) + \beta \tag{3.19}$$

with α, and β some real constants, and match both the $^{34}S^-$ yield, I, and its first derivative (dI/dz) at the inflection point with the corresponding values of the simulated profile. The resulting α and β read:

$$\alpha = \frac{dI}{dz}(z_c)\left[\frac{dI_s}{dz}(z_c')\right]^{-1} \tag{3.20}$$

$$\beta = I(z_c) - \alpha\, I_s(z_c') \tag{3.21}$$

where z_c and z_c' are the inflection points of the real and simulated profiles, respectively, that is,

$$\frac{d^2I}{dz^2}(z_c) = \frac{d^2I_s}{dz^2}(z_c') = 0 \tag{3.22}$$

Finally, to match the z axis for both real and simulated profiles, the z axis of the simulated profile is offset such that $z_c^{'} = z_c$.

This resulting vertically-scaled and horizontally-shifted, simulated profile is then fit to the actual data points of the measured $^{34}S^-$ profile of either the unannealed or annealed for 1-s or 10-s BLs. The fitting procedure minimizes the deviation between the simulated and $^{34}S^-$ profiles by using a genetic algorithm that optimizes all parameters sequentially in steps of ±0.1 nm from their starting values. In Figure 5f (main text), since minimal molecular mixing is expected for the unannealed BL, constraining w_0 to 1 nm gives, besides a reasonable RMS corrugation (σ = 2.7 nm), the w and λ parameters that are specific to our samples and sputtering conditions and that are further used to fit the partially annealed BLs. The resulting simulated profiles reveal a similar P3HT:dPCBM short-range mixing length ($w_0 \cong$ 11.5 nm) for both 1-s and 10-s annealed BLs (**Figure 3.11**e,f), demonstrating that the annealed D/A interface is produced in a matter of seconds and does not evolve with annealing time. Consequently, the calculated short-range mixing length holds also for the fully annealed BL and, as a result, for the annealed BHJ.

3.5.2 The Matrix Effect at the P3HT/dPCBM Interface

Another major issue with ToF-SIMS depth profiling is the so-called matrix effect, which is a result of the environment (that is, matrix) changing as function of depth. This issue affects the signals of a given species as function of sputtering time if the concentrations of the species composing the film vary significantly with depth. This is a result of the different ionization probability of the given species with the changing environment (matrix).

Unfortunately, the matrix effect problem cannot be avoided. However, to overcome this issue we have designed a calibration experiment where we have taken profiles of blends with different concentrations of P3HT and dPCBM (see **Figure 3.8** and **Section 3.3.1**). The signals obtained this way account for all matrix effects that could be encountered while the P3HT and dPCBM concentrations vary with depth. The matrix effects can be observed in the calibration curves (**Figure 3.7**c and **Figure 3.8**c,f), which obviously deviate from a straight line. Therefore, they need to be alleviated by using these calibration curves when calculating the absolute concentrations as function of depth. The biggest issue, however, is using the P3HT/dPCBM interface profile to calculate the mixing length for the bilayer sample. Here, the interface could be severely affected by the matrix effect. Fortunately, when converting, for example, the $^{34}S^-$ signal to the P3HT concentration in **Figure 3.11**a-c by using the calibration curve in **Figure 3.8**f, we note that the P3HT/dPCBM interfaces remain virtually the same, that is, the $^{34}S^-$ profiles are almost identical with the P3HT concentration curves at the P3HT/dPCBM interfaces, when represented on the same scale (**Figure 3.14**).

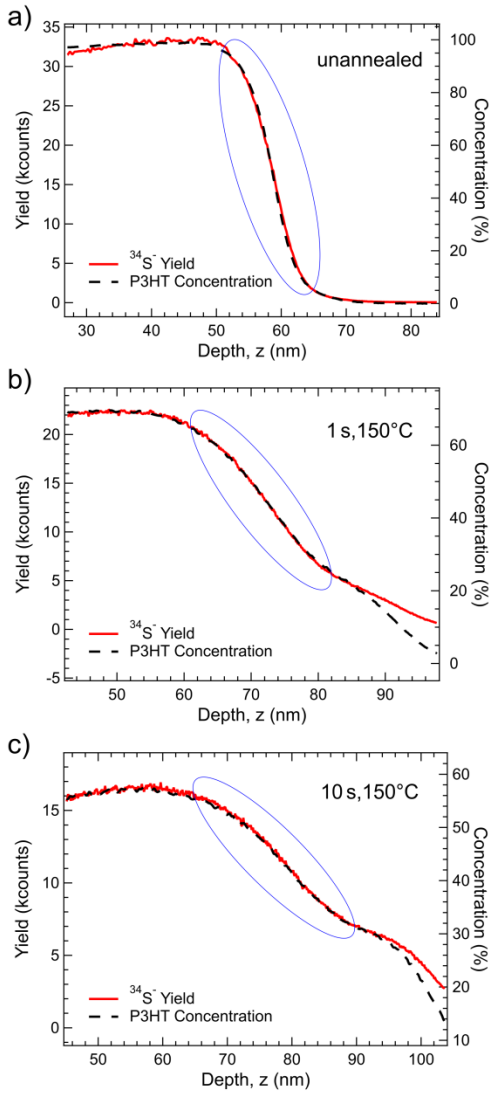

Figure 3.14 BL interface showing minimal matrix effect. (a-c) TOF-SIMS depth profile of $^{34}S^-$ (P3HT) secondary ion fragment (red, solid) and the corresponding P3HT concentration curve (black, dashed) for the unannealed (a), flash annealed for 1 second at 150°C (b) and flash annealed for 10 seconds at 150°C (c) P3HT/dPCBM BLs. For a given P3HT/PCBM interface both the $^{34}S^-$ depth profile and the resulting concentration curve match through the interface, when displayed on the same scale, indicating that the matrix effect is minimal and accounted for by the concentration conversion.

3.6 CONCLUSION/OUTLOOK

Consequently, the calculated short-range mixing length holds also for the fully annealed BL and, as a result, for the annealed BHJ. Assuming that the fine structure of the annealed BHJ consists of spheroidal-shaped domains (~37 nm diameter) with an outer shell thickness given by the 11.5 nm short-range mixing length, we estimate the crystalline P3HT core to be less than 14 nm in diameter. As a result, contrary to the general understanding that during annealing a BHJ forms largely pure domains[63,64] (required for efficient charge transport[25]), a simple geometrical calculation demonstrates the mixed regions account for >90% of the total volume of the domains, implying the annealing process leaves most of the BHJ in a mixed phase, therefore limiting the amount of free carrier pathways to the charge collectors, which explains the PCE limitation to ~5%.[25] These findings are consistent with previous theoretical calculations that show a high degree of mixing is detrimental to device performance, owing to the removal of beneficial conduction pathways formed at lower degrees of mixing.[73] However, when compared to the unannealed BHJ (PCE = 0.82%),[25] both the extracted short-range mixing length (~11.5 nm) and crystalline P3HT core radius (~7 nm) in the annealed domains are comparable with the exciton diffusion length,[63] suggesting the PCE improvement in the annealed BHJ is given by more efficient exciton transport in the P3HT core and mixed shell, followed by exciton dissociation in the mixed shell, and subsequent free charge transport through the crystalline P3HT core and the surrounding dPCBM.

Clearly, the BHJ PCE is directly linked to the ratio between the amounts of pure and mixed material, which can be estimated by knowing the D/A interface length. Balancing this ratio to the right value is essential in designing an optimal BHJ morphology. In a binary P3HT:PCBM blend we estimate a larger ratio than the one observed for the annealed BHJ (that is, ~1/9) should fundamentally increase the PCE due

to improved free charge transport in the pure phases while maintaining the exciton dissociation rate in the mixed phase.

To conclude, we demonstrate a robust, air-free ToF-SIMS/AFM methodology capable of probing in detail the buried chemical composition and morphology in binary D/A blends, with direct implications in their design optimization. Of note, our technique (i) directly measures and visualizes, respectively, the precise film composition and morphology as function of depth, and (ii) identifies and quantifies the D/A interface length, that is, the molecular mixing length at the D/A interface, a parameter that has never been measured while mostly overlooked despite its paramount influence on the device performance. In particular, for a P3HT:PCBM BHJ, our approach reveals the long-range (throughout the film) P3HT and PCBM segregation and the partial, short-range (local) PCBM demixing upon thermal annealing. We find the annealing process expands the P3HT/PCBM domains from ~30 nm to ~37 nm via partial P3HT crystallization and further aggregates them into larger structures with depth, thereby creating pathways for better carrier transport. Finally, by using an advanced sputtering model, we determine the D/A mixing length and show that the annealed P3HT/PCBM domains are mostly composed of mixed regions, which limit the PCE increase. Consequently, we expect the application of our methodology to various OPV configurations, including multicomponent blends,[171] to enhance the understanding of the complex relationship between device morphology, molecular mixing length at the D/A interface and device performance.

3.7 EXPERIMENTAL METHODS

3.7.1 Sample Preparation

Materials Regioregular poly(3-hexylthiophene-2,5-diyl) (P3HT) was acquired from 1-Material with a molecular weight of ~78kDa. [6,6]-phenyl C_{61} butyric acid methyl ester (PCBM) and pentadeuterophenyl-C_{61}-butyric acid methyl ester (dPCBM) were acquired from SES Research with purities of 99.5%. Poly(3,4-ethylenedioxythiophene)-poly(styrenesulfonate) (PEDOT:PSS) 1.3 wt % dispersion in H_2O, conductive grade and anhydrous chlorobenzene (CB) purity 99.8% were acquired from Sigma-Aldrich. Silicon wafers were purchased from University wafers.

BHJ preparation Normal (d)BHJs were prepared from a 1:1 mixture of 2% P3HT/CB and 2% (d)PCBM/CB. The 2% solutions were filtered through a 0.2 μm PTFE filter prior to mixing. The 1:1 mixture was spincoated at 700 RPM onto Si/SiO_2 wafers, previously cleaned by sonication in acetone, isopropanol, and water, individually for 15 min each. BHJ annealing was done on a hot plate in air for 30 min at 150°C. Calibration BHJs were made in a similar manner, starting with filtered 1.5% solutions of P3HT/CB and dPCBM/CB, mixing in appropriate ratios (that is, a ratio of 9:1 for a 10% dPCBM BHJ, etc.), and spin coating on Si/SiO_2 wafers at 700 RPM. All film thicknesses were characterized using a J. A. Wollam M2000 Spectroscopic Ellipsometer.

BL preparation P3HT/dPCBM bilayers (BLs) were produced by floating a pure P3HT film on nanopure water (18.2 MΩ·cm) and subsequent pick up onto a pure PCBM film. Pure P3HT films were produced by spin coating at 700 RPM from a filtered solution of 0.75% P3HT/CB onto a PEDOT:PSS-coated Si/SiO_2 wafer. PEDOT:PSS was sonicated for 1 hour, filtered through a 0.45 μm PVDF filter, and spincoated at 1000 RPM on previously cleaned Si/SiO_2 wafers. Pure PCBM films were made by spin coating a 1.75% solution at 700 RPM onto a Si/SiO_2 wafer cleaned in the same manner

with an added 5 min oxygen plasma etch prior to use. BL annealing (1 s, 10 s, 10 min at 150°C) was done on a flash heating/cooling stage inside the ToF-SIMS instrument.

3.7.2 ToF-SIMS Analysis

For depth profiling and chemical analysis we used a TOF.SIMS 5 instrument (ION-TOF GmbH, Germany, 2010). During depth profiling the sputtering ion beam (Cs^+ at 500 eV ion energy, ~40 nA measured sample current and ~1 μm beam size) was raster scanned over an area of 300 x 300 μm^2. The analysis ion beam consisting of Bi_3^+ pulses (30 keV ion energy, 20 ns pulse duration, 0.8 pA measured sample current) was set in the high current bunched (HC) mode and raster scanned over a 100 x 100 μm^2 area centered within the Cs^+ sputtered area at the regressing surface. Bi_3^+ was chosen to enhance the yield of organic secondary ions and to reduce the sputtering induced mixing.[135] The depth profiles were acquired in noninterlaced mode at a base pressure of 10^{-9} torr. All mass spectra were acquired in negative polarity while the mass resolution was >7000 ($m/\delta m$) for all fragments of interest. The sputtering rates were calculated at 0.39 nm/s and 0.07 nm/s for the pure P3HT and PCBM, respectively. For the AFM measurements, due to the high reactivity of the sputtered spots with air we used an in-house designed air-free capsule[160] to transfer the sputtered samples to and from a nitrogen-filled glove box (containing the AFM setup) in vacuum or nitrogen environment, respectively.

3.7.3 AFM Analysis

For surface mapping we used a Bruker Dimension 3100 AFM that was enclosed in a nitrogen-filled glove box (Innovative Technologies), to ensure the Cs^+ and Bi_3^+ sputtered spots were protected from any oxygen-related reactions. A MikroMasch HQ:NSC14/Al BS silicon probe was used to take tapping mode topography images, which were analyzed with image autocorrelation to extract domain size.

Chapter 4: Light- and Electric Field- Induced Interfacial Effects on Perovskite Degradation

4.1 Introduction to Light- and Electric Field- Induced Degradation Experiments

This chapter focuses on work in understanding light-induced degradation in $MAPbI_3$ perovskite devices as well as electric field-induced degradation in $MAPbI_3$ films. These degradation pathways result in chemical and morphological changes at device/film interfaces. Each subsection provides a brief introduction, followed by a summary of work done by our collaborators motivating the need for understanding the chemical and morphological changes under the external stress (either light or electric bias), and completed with my contributions and conclusions using ToF-SIMS to address the observed changes.

4.2 Light-Induced Degradation‡

4.2.1 Introduction

Perovskite solar cells based on the hybrid methylammonium or formamidinium lead iodides ($MA/FAPbI_3$) represent now the most rapidly developing photovoltaic technology, which has surpassed successfully the 20% efficiency threshold.[2,15] Practical implementation of perovskite solar cells is still hampered by their poor operation stability originating from multiple intrinsic and extrinsic degradation processes.[172–175] While the highest reported efficiencies were obtained for perovskite solar cells utilizing compact TiO_x layer and mesoporous oxide scaffold,[176,177] alternative planar junction devices attract swelling attention.[76,178] A simple solution-based technology used for fabrication of planar junction perovskite solar cells can be potentially easy up-scaled for their industrial

‡ Portions of this section were published in Akbulatov, A. F., Frolova, L.A., Griffin, M. P., Gearba, I. R., Dolocan, A., Vanden Bout, D. A., Tsarev, S., Katz, E. A., Shestakov, A. F., Stevenson, K. J., Troshin, P. A. *Adv. Energy Mater.* **2017**, 1700476 for which M. Griffin analyzed and interpreted the ToF-SIMS data.

production.[179] Planar junction devices can be also fabricated on flexible plastic substrates by growing the photoactive perovskite layer on top of the hole transport layer (HTL) material (e.g., commercial or modified poly(3,4-ethylenedioxythiophene):polystyrene sulfonate, PEDOT:PSS,[180] or other materials such as copper(I) iodide (CuI) or copper(I) oxide (Cu_2O)[181]), while the device stack is completed by coating with the electron transport layer (ETL) and depositing a top electron-collecting electrode.[182] This kind of "inverted device configuration" resembles closely the standard architecture of organic solar cells intensively investigated for more than a decade.[183]

Efficient inverted perovskite solar cells have been fabricated using different ETL materials such as conjugated n-type polymers,[184,185] zinc oxide,[186,187] functionalized perylene diimides,[188–194] and fullerene derivatives.[195,196] Among all these materials, readily available fullerene-based compound PCBM has been utilized most extensively either alone or in combination with various polymer binders.[197–201] Perovskite solar cells using PCBM as ETL deliver virtually hysteresis-free behavior in current-voltage characteristics and impressive power conversion efficiencies of 10-17%.[112,202,203] Unfortunately, inverted planar junction perovskite solar cells are generally prone to a rapid degradation under illumination. It has been shown recently that this kind of degradation is apparently related to the chemical reactivity of perovskite material with the metal top electrode.[92] However, the fundamental mechanism of this kind of degradation process and the role of the ETL material have not been clarified until now.

4.2.2 Motivation Based on Collaborators' Work

While designing planar junction perovskite solar cells based on methylammonium lead iodide ($MAPbI_3$), they were screening different ETL materials in order to achieve improved photovoltaic performance and stability. They paid special attention to perylene

diimide derivatives due to their excellent chemical resistance and good charge transport characteristics, as it was noticed previously.[185–191] A soluble perylene diimide derivative, N,N'-di-2-ethylhexyl-3,4,9,10-perylenetetracarboxylic diimide, PDI-EH (**Figure 4.1**a), which they designed previously as a solution processible n-type semiconductor for organic field-effect transistors,[204] was utilized as a ETL material along with PCBM (**Figure 4.1**b) for inverted planar junction perovskite solar cells (**Figure 4.1**).

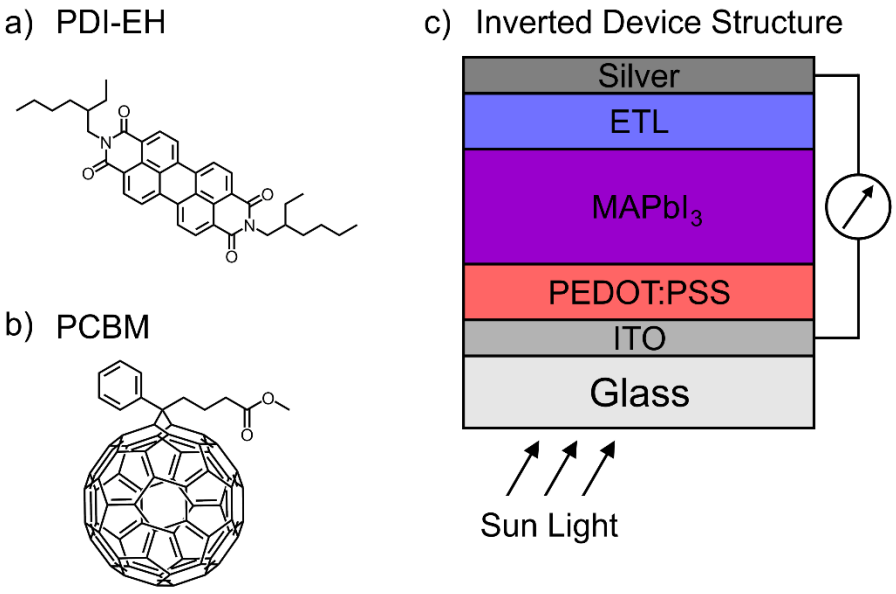

Figure 4.1 Materials and device structure. Electron transport layer (ETL) materials, (a) PDI-EH and (b) PCBM and (c) inverted device structure.

They noticed that both types of the photovoltaic devices incorporating PCBM and PDI-EH as ETL materials deliver very comparable initial power conversions efficiencies of ~10%. The device using PCBM resulted in slightly higher open circuit voltage (V_{OC}) and fill factor (FF), while devices comprising PDI-EH generated enhanced short circuit current density (J_{SC}) and external quantum efficiency (EQE). Regardless, this comparison demonstrates that the perylene diimide derivative PDI-EH indeed represents an improved

ETL material for inverted planar junction solar cells and can successfully replace PCBM with regards to device efficiency.

Furthermore, the inverted planar junction perovskite solar cells incorporating PCBM as the ETL material undergo rapid light induced degradation as their efficiency decreased to ~10% of the initial value just within 30 hr, and after 120 hr it dropped to zero. On the contrary, devices comprised of PDI-EH as ETL material maintained 97% and 72% of the initial efficiency after 30 hr and 120 hr of aging, respectively.

The obtained results strongly suggested that PCBM is the main cause for the observed rapid degradation of the perovskite solar cells. They initially assumed that a possible chemical reaction occurs at the interface between $MAPbI_3$ and PCBM. However, analysis of the aged bilayer $MAPbI_3$/PCBM films using high-performance liquid chromatography (HPLC) and Electrospray Ionization (ESI) mass spectrometry revealed no noticeable degradation or additional functionalization of the fullerene derivative, besides some photodimerization, which is known for PCBM.[205] Therefore, they surmised that there is no evident chemical reaction occurring between PCBM and $MAPbI_3$ under illumination.

4.2.3 Chemically Tracking ETL Dependent Light-Induced Degradation

In order to shed some light on the actual role of PCBM in the rapid degradation of inverted perovskite solar cells, we used Time-of-Flight Secondary Ion Mass Spectroscopy (ToF-SIMS), which is known as a powerful chemical analysis technique extensively used in the field of perovskite photovoltaics.[128,206–209] We profiled the perovskite solar cell stacks incorporating PCBM or PDI-EH layers before and after indoor illumination within 30 hrs. The power conversion efficiency (PCE) of investigated devices with the PCBM layer decreased almost completely to zero after aging, while the

cells comprising of PDI-EH aged under the same conditions sustained their initial performance.

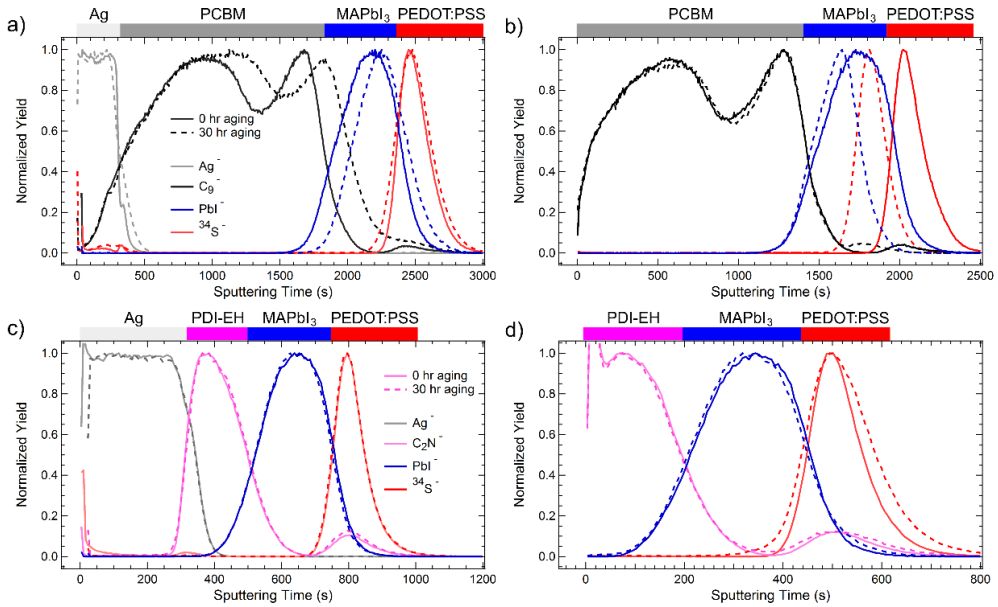

Figure 4.2 TOF-SIMS depth profiles of PCBM and PDI-EH devices. The depth profiles indicate the changes in the devices interfaces incorporating PCBM (a,b) or PDI-EH (c,d) as ETL material obtained for the sample areas covered (a, c) and non-covered with (b, d) silver contacts. The solid lines are without aging (0 hr) and the dashed lines indicate 30 hr aging. For the covered areas, the profiles were aligned at the Ag/ETL interface to highlight changes due to the slight difference in silver thickness.

The obtained TOF-SIMS depth profiles are presented in **Figure 4.2**. The depth profiles for the PCBM devices (**Figure 4.2**a,b) show a dramatic change upon light aging in both areas that are covered (**Figure 4.2**a) and non-covered (**Figure 4.2**b) by the silver contacts as opposed to the PDI-EH devices (**Figure 4.2**c,d). For all stacks, the 0 hr-aged profiles are given by solid lines and the 30 hr-aged profiles are given by dashed lines. In the covered stacks, we use the Ag^- ion fragment to locate the silver electrode. The ETLs are represented by the C_9^- and C_2N^- ion fragments for PCBM and PDI-EH, respectively.

We have selected the PbI^- and $^{34}S^-$ ion fragments to represent the $MAPbI_3$ perovskite and PEDOT:PSS layers, respectively. While analyzing the PbI^- ion fragment in the PCBM stacks, we conclude that $MAPbI_3$ undergoes a severe photoinduced decomposition when PCBM layer is deposited on top. The perovskite layer shrinks considerably, while the PCBM layer expands proportionally, thus keeping the total thickness of the stack almost unchanged. These data strongly suggest that some volatile components left the $MAPbI_3$ layer. However in the case of the PDI-EH stacks (**Figure 4.2**c,d), there are no noticeable changes in the $MAPbI_3$ or PDI-EH layers in either the covered (**Figure 4.2**c) or the non-covered (**Figure 4.2**d) areas. The changes in the PEDOT:PSS layers for both the PCBM and PDI-EH stacks suggest that there is possibly a structural change and/or notable mixing from $MAPbI_3$ or its degradation products with PEDOT:PSS. In the PDI devices, the intermixing at the PEDOT:PSS/$MAPbI_3$ interface did not result in any deterioration of the photovoltaic performance of the devices with PDI-EH electron-transport layer. Nevertheless, the effects observed near the ITO/PEDOT:PSS hole-collecting contact are minor in comparison with the effects at the electron-collecting contact.

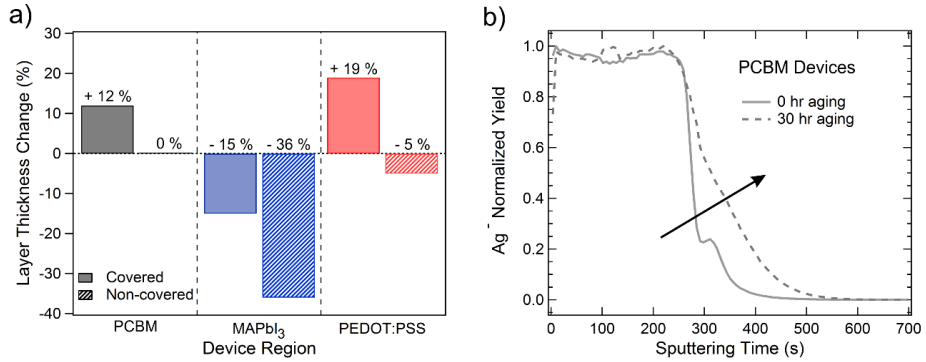

Figure 4.3 Detailing the observed changes in the PCBM device. (a) The quantification of the layer thickness changes upon aging and (b) the broadening of the Ag/PCBM interface. The layer thickness changes in (a) were calculated from the difference in layer sputtering time in the 30 hr-aged stacks versus the 0 hr-aged stacks.

The percent change of the layer thickness upon aging in the PCBM-based stack is given in **Figure 4.3**a. We clearly see that the perovskite layer shrinks upon aging in both the covered and non-covered areas. Interestingly, the effect is greater in the non-covered regions suggesting that the PCBM layer and/or silver contact slightly protect the device. The broadening of the silver interface (**Figure 4.3**b) suggests that aging the PCBM device causes mixing and/or a morphological change at the Ag/ETL interface.

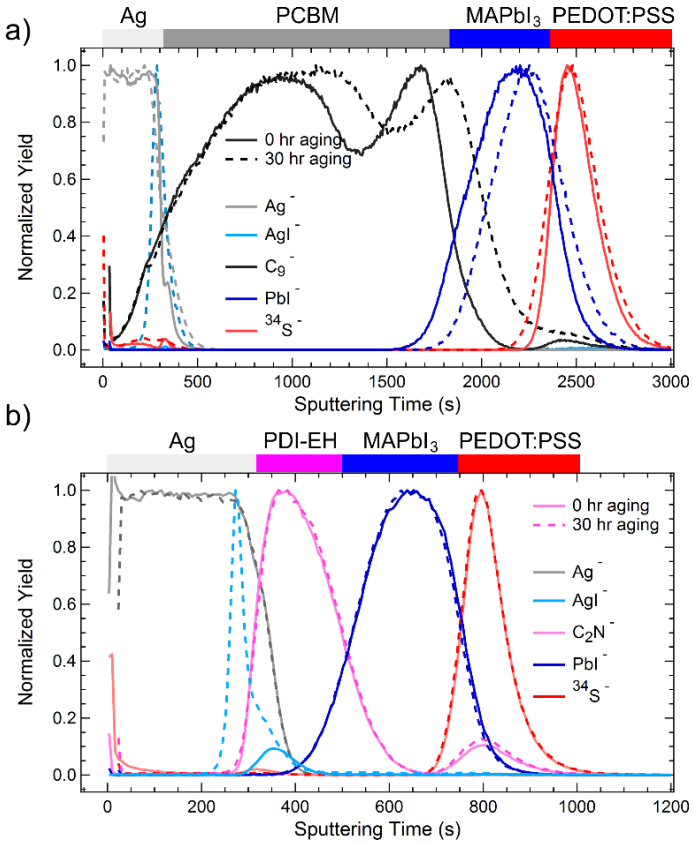

Figure 4.4 ToF-SIMS depth profiles showing silver iodide formation. The profiles show the formation of AgI layer at the interface between the ETL and top silver electrode for the PCBM (a) and PDI-EH (b) stacks. All profiles except the AgI^- ion fragment are normalized to their respective maxima. The AgI profiles are normalized to the maximum of the 30 hr-aged profile for each ETL material.

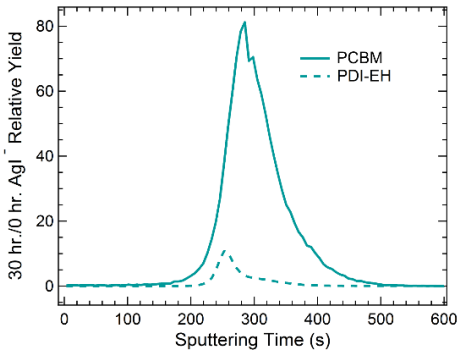

Figure 4.5 Silver iodide comparison upon aging in the devices. Comparison of the formation of silver iodide in the stacks comprising PCBM and PDI-EH as ETL materials.

The AgI^- ion fragment (**Figure 4.4**) indicates the formation of the interfacial AgI layer, which is fully consistent with the previous findings.[112,206,210–212] In both the PCBM and PDI-EH devices, we see the formation of the interfacial AgI layer. When we compare the 30 hr aging yield to the 0 hr yield in both devices (**Figure 4.5**), the relative AgI^- ion yield indicates that light aging in the PCBM devices produces much more AgI than in the PDI-EH devices. Therefore, we can conclude that aging of the $MAPbI_3$/PCBM stack results in the significant liberation of MAI (leaving solid PbI_2 behind), which diffuses through the PCBM layer and accumulates at the interface, if the Ag contact is deposited on top. In the areas, which were not protected with Ag, MAI diffuses all the way through the PCBM layer and evaporates. Therefore, liberation of MAI and formation of PbI_2 results in a dramatic shrinkage of the $MAPbI_3$ film.

In the case of the PDI-EH stacks, where the silver iodide interfacial layer was also formed at the Ag/PDI-EH junction, it is likely that that iodine (or iodide) might diffuse between the grain boundaries of PDI, which does not affect negatively the device performance at least in timescale of our experiments

Summarizing the results obtained using ToF-SIMS, we can conclude that the drastic difference in the operational stability of the planar junction perovskite solar cells incorporating PCBM or PDI-EH layers is exclusively related to the remarkably different physicochemical properties of these two electron transport materials.

4.2.4 ToF-SIMS Experimental Methods

For depth profiling and chemical analysis, we used a TOF.SIMS 5 instrument (ION-TOF GmbH, Germany, 2010). During depth profiling the sputtering ion beam (Cs^+ at 500 eV ion energy and ~40 nA measured sample current) was raster scanned over an area of 300 x 300 μm^2. The analysis ion beam consisting of Bi_1^+ pulses (30 keV ion energy, 100 ns pulse duration, 0.04 pA measured sample current) was set in the high current bunched (HC) mode and raster scanned over a 100 x 100 μm^2 area (256 pixels x 256 pixels) centered within the Cs^+ sputtered area at the regressing surface. The depth profiles were acquired in interlaced mode at a base pressure of 10^{-9} torr. All mass spectra were acquired in negative polarity while the mass resolution was >8000 (m/δm) for all fragments of interest.

4.3 ELECTRIC FIELD-INDUCED DEGRADATION[§]

4.3.1 Introduction

Exceptional photovoltaic properties of solution processed hybrid perovskite materials have spurred intensive investigations. Currently, the PCE of perovskite solar cells exceeds 22% on the best laboratory samples.[2,15] Despite the rapid PCE improvement, practical use of hybrid perovskite solar cells is hindered by fast environmental degradation.[213,214] While degradation from humid atmosphere can be

[§] Portions of this section were published in Luchkin, S. Y., Akbulatov, A. F., Frolova, L. A., Griffin, M. P., Dolocan, A., Gearba, R., Vanden Bout, D. A., Troshin, P. A., Stevenson, K. J. *ACS Appl. Mater. Interfaces,* **2017**, *9*, 33478-33483 for which M. Griffin analyzed and interpreted the ToF-SIMS data.

suppressed by proper cell encapsulation, degradation processes under photon flux and electric field (built-in, externally applied, or photoinduced) are intrinsic and can hardly be prevented. Elucidation of these degradation processes is an essential step to overcome current limitations. Additionally, there is the need to understand how these degradations occur throughout the entire 3D configuration and specifically at interfaces.

Electric field studies have reported to cause both functional and structural transformations of hybrid perovskite solar cell.[104,106] $MAPbI_3$ itself is thermodynamically unstable.[82] It is also kinetically unstable due to low activation energies for I^- and MA^+ migration.[97,105,215–217] Therefore, it is not surprising that under electric bias $MAPbI_3$ is subjected to irreversible decomposition, as previously reported.[96,106,218] Similar effects besides photolysis[219] may be caused by light generated photovoltage, which acts in similar ways as an externally applied voltage.[220,221] However, electric bias does not always cause irreversible degradation. For example, a switchable photovoltaic effect,[104] which is associated with migration of ions within the perovskite layer, can be reversed by applying opposite bias voltage. Reversible conversion between $MAPbI_3$ and PbI_2 was also experimentally observed at small voltages.[222] And, it has been shown that the I-V hysteresis has both irreversible and reversible parts[223] and that it also strongly depends on contact material.[101,102] These observations raise a question about the role of $MAPbI_3$ interfaces with contact materials in these processes.

4.3.2 Motivation Based on Collaborators' Work

To systematically study the irreversible degradation of $MAPbI_3$ perovskite films on ITO/glass, our collaborators used a conductive probe AFM technique to locally apply a bias to the sample. A depiction of the AFM technique is given in **Figure 4.6**a where a platinum (Pt) coated silicon tip (both front and back reflective coating) is grounded while

the ITO contact is biased during scanning. They systematically scanned 5 μm x 5 μm regions changing the applied voltage to the ITO electrode; creating different lithography regions (**Figure 4.6**b). In doing so, they noticed, in agreement with their previous conductive probe AFM point measurement experiments, large area surface transformations in regions with high negative bias (-4 V to -8 V). These regions are schematically shown in **Figure 4.6**b with blue shading.

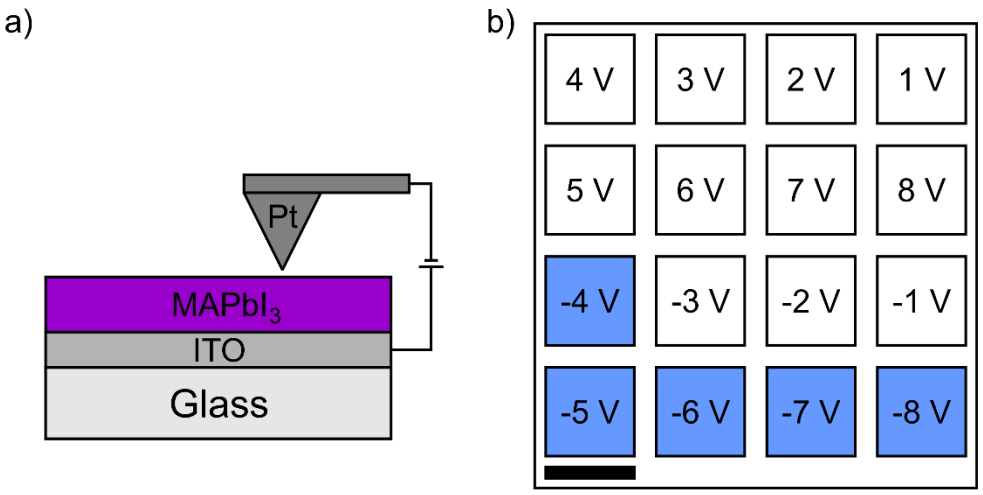

Figure 4.6 Schematic depictions of electric field-induced experiments. (a) An AFM technique where a conductive Pt-coated probe is grounded and the ITO electrode is biased. (b) Regions that were scanned by AFM applying different voltages with regions of visual transformations noted in blue. Scale bar is 5μm.

4.3.3 ToF-SIMS Imaging and Electric Field-Induced Mixing

In order to understand more fully the chemical/morphological origins of the topography changes observed by applying high electric bias, we performed ToF-SIMS measurements on the degraded perovskite film. The ToF-SIMS data are presented in **Figure 4.7**, where the PbI_2^- and SnO_2^- ion fragments represent the $MAPbI_3$ and ITO, respectively. To start, in the 3D reconstruction of the sputtered volume, we note

significant chemical variations appearing in the lithography regions at the $MAPbI_3$/ITO buried interface (**Figure 4.7**a). Regions of interest (ROIs) corresponding to the AFM lithography regions were identified based on the PbI_2^- secondary ion map (**Figure 4.7**b) and depth profiles (**Figure 4.7**c) for each of these ROIs were reconstructed. All profiles were normalized to their corresponding ROI area, while the depth conversion was calculated by employing a sputtering rate model that assumes the sputtering rate at the $MAPbI_3$/ITO interface as a linear combination between the individual sputtering rates.[156]

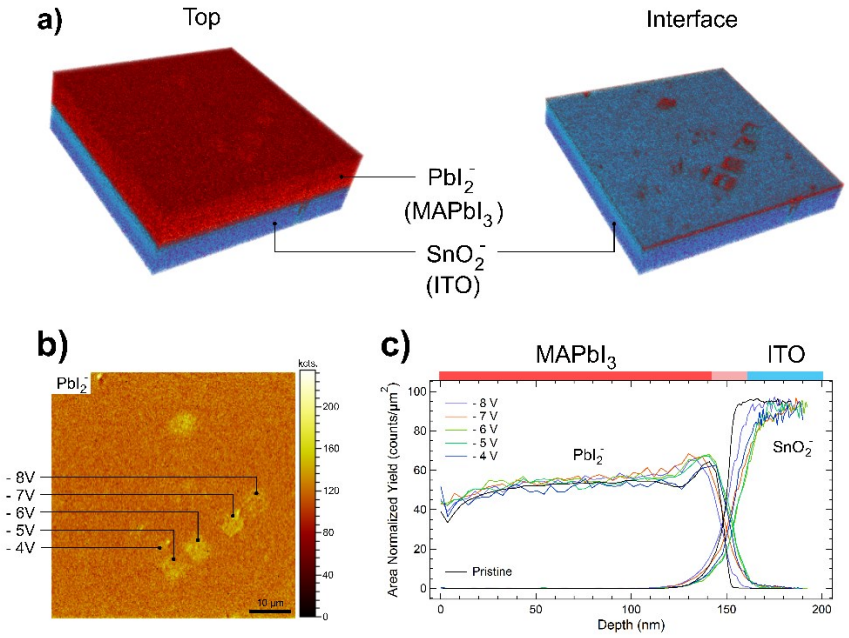

Figure 4.7 ToF-SIMS depth profiling of degraded perovskite film. (a) 3D reconstruction of the sputtered volume including the lithography regions. Representing the $MAPbI_3$ and ITO layers, respectively, the PbI_2^- (red) and SnO_2^- (blue) secondary ion fragments are displayed in a dual color overlay. A significant chemical variation is observed at the $MAPbI_3$/ITO buried interface in the lithography regions with respect to the pristine region. (b) The total PbI_2^- ion signal map indicates the lithography-modified areas and provides the regions of interest (ROIs) denoted in the individual depth profiles shown in (c). The pristine profile is taken from outside the modified regions in the 4 corners of the analyzed area. The unlabeled area corresponding to +1 V lithography area seems to be an artifact, since the other areas corresponding to +2 V to +8 V lithography do not show changes.

The broadening of the $MAPbI_3$/ITO interface suggests mutual diffusion (percolation) of the $MAPbI_3$-derived species into the ITO and vice versa. To quantify the extent of this molecular mixing, we use the so-called mixing-roughness-information (MRI) model,[142,144] which simulates depth profiles of interfaces while accounting for the sputtering induced mixing (w), the information depth (λ), and corrugation (σ) effects, to determine the molecular mixing length (w_0), that is, the length of the real interface. For the pristine case (**Figure 4.8**a), we simulate and fit the PbI_2^- ion fragment profile at the ITO interface to determine the w and λ parameters and calculate minimal molecular mixing (w_0 = 1.1 nm) with an interfacial corrugation, σ, of ~1.9 nm. When fitting the lithography regions, for example, the - 4 V ROI (**Figure 4.8**b), we fix the w and λ parameters to the values determined from the pristine profile, and allow the corrugation and real mixing parameters to vary freely. The calculations yield large corrugation increases in the lithography regions, as expected from the AFM surface topography measurements. Of note, the corrugation at an interface between two materials is, most times, an average between the corrugation of the substrate and that of the surface of the over layer. Even with the large corrugation change (~2 times pristine) we calculate a large extent of mixing, ~5 times the mixing in the pristine case for the - 4V ROI. A summary of the calculated molecular mixing length, w_0, is given in **Figure 4.8**c. The general trend in the forward direction is that mixing increases with applied voltage.

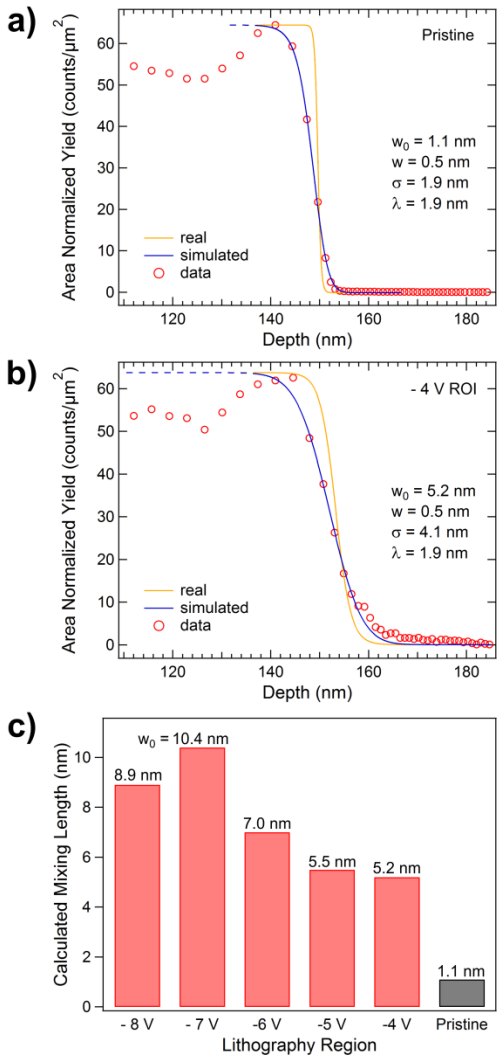

Figure 4.8 Atomic mixing at the buried $MAPbI_3$/ITO interface. (a, b) MRI simulations, using the PbI_2^- ion fragment, through the $MAPbI_3$/ITO interface for the pristine (a) and - 4 V (b) ROIs. The real interface is broadened by sputtering effects, which are accounted for in the simulated profile (see text). (c) A summary of the calculated mixing lengths for the pristine $MAPbI_3$/ITO interface versus the different areas of lithography performed at various bias voltages.

What is important here is that unlike the $MAPbI_3$/ITO interface, the Pt(tip coating)/$MAPbI_3$ interface was subjected to less significant chemical transformation

(**Figure 4.7**a) even though the electric field at the tip-sample contact was higher due to the electric field constraint at the tip. This observation is in agreement with their previously reported results. Indeed, the reversible reaction was reported in $MAPbI_3$ deposited on glass and when bias is applied between Au electrodes,[222] while the irreversible one was reported in $MAPbI_3$ sandwiched between ETL and HTL functional layers.[106] Thus, it is reasonable to suggest that the appearance and magnitude of the irreversible filed-induced chemical decomposition of $MAPbI_3$ depend on the used contact or functional ETL and HTL layers. These findings strongly suggest that the $MAPbI_3$ interfaces with adjacent functional layers predefine not only the solar cell efficiency, while controlling the extraction and surface recombination of charge carriers, but also the electrochemical stability of the perovskite absorber and the entire device. Improper choice of contact materials and HTL and ETL layers might significantly reduce the lifetime of perovskite solar cells.

4.3.4 ToF-SIMS Experimental Methods

For depth profiling and chemical analysis, we used a TOF.SIMS 5 instrument (ION-TOF GmbH, Germany, 2010). During depth profiling, the sputtering ion beam (Cs^+ at 500 eV ion energy and ~40 nA measured sample current) was raster scanned over an area of 300 × 300 μm^2. The analysis ion beam consisting of Bi_1^+ pulses (30 keV ion energy, 100 ns pulse duration, 0.04 pA measured sample current) was set in the burst alignment (BA) mode and raster scanned over a 60 × 60 μm^2 area (256 × 256 pixels) centered within the Cs^+ sputtered area at the regressing surface. The depth profiles were acquired in noninterlaced mode, that is, sequential sputtering and analysis, at a base pressure of 10^{-9} torr. All mass spectra were acquired in negative polarity while the mass resolution was >300 (m/δm) for all fragments of interest. After data collection, the

different ROIs, e.g., the −4 V lithography area, were individually reconstructed and analyzed. The reconstructed depth profiles were normalized to their corresponding ROI area to allow for a fair comparison of signal acquired from the different ROIs. The sputtering rates were calculated at 0.72 and 0.18 nm/s for the $MAPbI_3$ perovskite and ITO, respectively.

4.4 CHAPTER CONCLUSIONS

In this chapter, we have investigated changes in chemistry and morphology of $MAPbI_3$ perovskite films/devices based on two different degradation pathways: light-induced or electric field-induced degradation. In doing so, we focused on the role of interfaces in preventing or facilitating perovskite degradation.

We have shown the effects of light-induced degradation in inverted planar $MAPbI_3$ devices based on two different ETL materials. In these devices, initial device performance between the PDI-EH and PCBM ETLs were similar, however, stability over time with the PDI-EH ETL was much better. The ToF-SIMS data shows chemically that photoexposure in devices with PCBM as the ETL caused the $MAPbI_3$ perovskite layer to shrink, the PCBM layer to grow, and the formation of silver iodide at the top metal contact interface. In devices with PDI-EH as the ETL, these chemical and morphological changes did not occur. These phenomena indicate and confirm that PCBM facilitates degradation of the $MAPbI_3$ layer by allowing MAI to percolate through, collect at the silver contact interface, and form silver iodide; whereas, the PDI-EH layer provides a better barrier layer to this degradation pathway. This work has provided an alternative ETL material with enhanced device stability, showing the need for proper choice of device supporting layers as we look toward long term stability.

In understanding electrical degradation, we have also shown that electric field-induced degradation in $MAPbI_3$ perovskite films occurs at high bias. The observed changes at the top surface stem from induced mixing at the $MAPbI_3$/ITO bottom interface as opposed to the Pt/$MAPbI_3$ interface. The implications being that choice of contact material (that is, a platinum or ITO electrode) is key in facilitating or hindering perovskite/device long term performance under electrical bias.

Overall, the use of ToF-SIMS has provided a way to study the nanoscale chemical and morphological changes in these perovskite systems. Our method has shown the changes at these interfaces (ETL or contact) that happen on the nanoscale and which affect overall perovskite film/device long-term stability and thus performance.

Chapter 5: Ion Migration in Lateral $MAPbI_3$ Perovskite Devices via *In-situ* ToF-SIMS Electrical Biasing

5.1 Introduction to Ion Migration in $MAPbI_3$ Perovskites

The hybrid organic-inorganic perovskite, methylammonium lead iodide ($CH_3NH_3PbI_3$ or $MAPbI_3$), has been well studied for its use in photovoltaics with its downfall being long-term instability. One of the many explanations for electrical instability in $MAPbI_3$ perovskites is ion migration. Here, lattice vacancies/defects are created by removal of any of the ionic components (here, MA^+, Pb^{2+}, or I^-) from their respective sites within the crystal structure and ion drift occurs in the device electric field (either internal or applied) altering the steady state electrical properties.[96,104,105,215,224–226] Although ion migration stems from degradation of the perfect perovskite lattice, there is some evidence that it leads to "self-doping"[104,224] where an intrinsic n-i-p (or p-i-n) structure is formed within the perovskite layer itself, with minimal change in performance albeit with a simpler lateral device structure.[104] Moreover this self-doping effect has been shown to be both irreversible,[96,104] with permanent perovskite degradation, or reversible[104,105] opening up new applications for perovskites that could benefit from switched poling (i.e. memristors).

The understanding of self-doping in these systems is that charged lattice vacancies induce doping. For p-type doping, there would be more negatively charged vacancies, either from a Pb^{2+} or MA^+ deficiency; for n-type doping, there would be more positively charged vacancies from an I^- deficiency.[97,104,215,224–226] Self-doping can be induced via perovskite formation/processing[97,104] or electrical biasing[224–226]. When done electrochemically, I^- migration to the anode in the applied electric field creates positive charged vacancies, where proposed oxidation can occur of the iodide anion (I^-) to triiodide (I_3^-), which remains in the perovskite, or to molecular iodide (I_2), which can

evaporate.[96] Although having higher activation energies for ion migration[97,215] than I^-, MA^+ and potentially Pb^{2+} can also migrate to the cathode under the applied external bias. Photothermal Induced Resonance (PTIR) microscopy has provided evidence for MA^+ migration to the cathode.[105] It has been suggested that hydrogen species (H^+, H^0, H^-), either from residual moisture from preparation/fabrication or from decomposition of methylammonium, could account for some ion migration.[227] The ion migration activation energy of H^+ is similar to that of I^-,[227] suggesting that ion migration to and reduction of H^+ to hydrogen gas (H_2) at the cathode may be part of the irreversible degradation pathway.[96]

Most attempts to spatially visualize ion migration in $MAPbI_3$ perovskites have been conducted by others by first poling the device to some steady-state and analyzing the final result. To track MA^+ migration, Yuan *et al*. performed PTIR after different, discrete lengths of poling time (100 s steps), showing the progression of MA^+ to the cathode.[105] In tracking I^- migration to the anode, Frolova *et al.* performed Energy-Dispersive X-ray Spectroscopy (EDX) after irreversibly degrading the perovskite film under bias (~1 V/μm) for ~2 hrs.[96] Although these techniques are chemically sensitive to track certain species, they are (1) unable to track all of the species of interest (such as hydrogen) and (2) they have yet to be utilized to perform biasing *in situ*. Xiao *et al.* performed *in situ* biasing on a lateral perovskite device but used a non-chemically sensitive technique, transmission optical microscopy, to visualize changes in film composition and morphology, noticing a bleaching and attributing it to Pb^{2+} and/or MA^+ migration from the anode to the cathode.[104]

Here, we develop a method to do *in situ* biasing with Time-of-Flight Secondary Ion Mass Spectrometry (ToF-SIMS) to understand chemical changes due to electrical decomposition in $MAPbI_3$ perovskites. By using ToF-SIMS, we are able to detect all

species of interest with high sensitivity, including hydrogen, and by performing the measurements *in situ* we are able to immediately, without loss of any potential steady-state conditions, visualize chemical changes. *In situ* ToF-SIMS electrochemistry is a unique combination and its use has been previously limited to understanding model systems of liquid[228,229] and solid state[230] electrode-electrolyte chemistry. In this chapter, we will explore I^- migration by performing ToF-SIMS experiments in negative polarity with respect to the ToF-SIMS extractor; to access cation migration (H^+, MA^+, and potentially Pb^{2+}), future experiments should be performed in the same manner but in positive polarity.

5.2 Results and Discussion

The work presented in this chapter is in collaboration with the Mullins group here at The University of Texas at Austin. Bryan Wygant has graciously supplied the $MAPbI_3$ perovskite films and has ensured high quality perovskite by routinely checking $MAPbI_3$ perovskite photovoltaic device performance (see **Section 5.4.1**).

Lateral $MAPbI_3$ perovskite devices (schematic in **Figure 5.1**a,c) with 20 μm channel widths and 80 nm thick gold electrodes were fabricated on silicon substrates. **Figure 5.1**b presents a typical ToF-SIMS depth profile of a lateral device. The profile area encompasses the whole device, that is, across both gold electrodes and the channel (**Figure 5.1**c). The PbI_2^- ion fragment (red) tracks the perovskite film and the Au^- ion fragment (blue) represents the gold electrodes. At first, sputtering removes only $MAPbI_3$ perovskite until the interface at the gold electrodes is revealed (**Figure 5.1**a,b, dashed arrow). For the imaging experiments, it is important to stop at this plane to visualize the gold electrodes; above this plane, the electrodes are buried beneath perovskite. Further sputtering removes the rest of the perovskite and some of the gold due to the faster

sputtering rate of the perovskite compared to the gold. The increase in yield at the perovskite/gold interface is due to the previously mentioned matrix effect (**Chapters 2, 3 and 4**). Each lateral device is 20 µm and 1 mm long (**Figure 5.1**c) providing plenty of area for ToF-SIMS analysis on the same device (see **Section 5.4**).

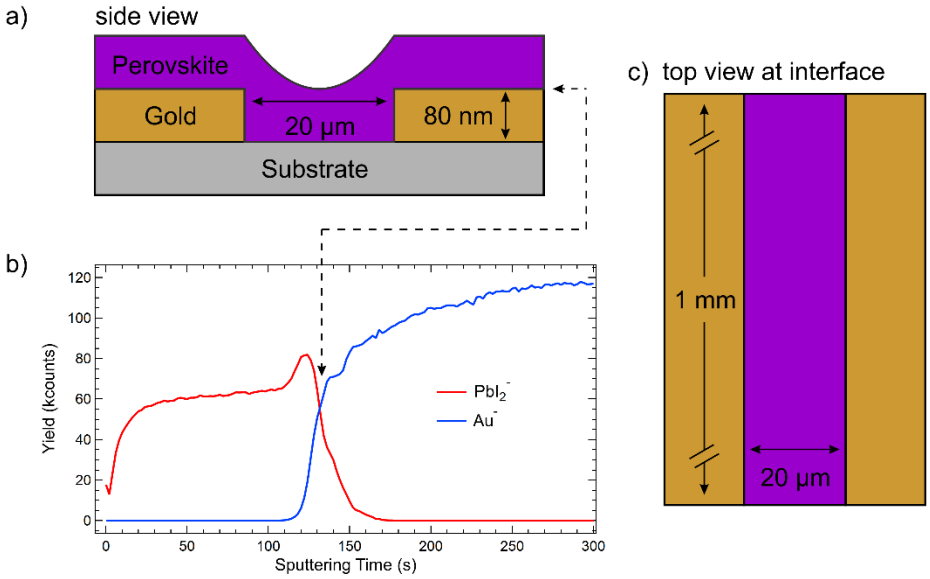

Figure 5.1 Lateral perovskite device architecture. (a) A schematic of the side view of the lateral devices, (b) a typical depth profile for lateral devices with the top perovskite/gold interface denoted with dashed arrows and (c) a top view of the lateral devices.

5.2.1 Unbiased Imaging

Figure 5.2 shows total image maps of the unbiased lateral $MAPbI_3$ perovskite devices. These images were taken at the perovskite/gold interface, that is, after ~120 s of sputtering (**Figure 5.1**), and show the total ion yield for each specific ion fragments (Au^-, I^-, PbI_2^-) summed over 200 s of imaging. In these images, the perovskite device is the area between the two electrodes: the anode, A, on the left and the cathode, C, on the right. The Au^- ion fragment map (**Figure 5.2**a) shows signal arising only from the gold electrodes, as expected. There is a difference in intensity that appears like a large X (or

cross) over the electrodes that results from uneven sputtering to the buried plane. The brighter area (the cross), showing a higher intensity of Au^- ion fragment yield, is a region where the perovskite sputtered faster than in the darker region. Nevertheless, the sputtering in the channel appears to be more even, given the results from the perovskite ion signals. **Figure 5.2**b shows the I^- ion fragment map. It appears that signal comes from both the perovskite in the device channel, as expected, as well as some from above the gold electrodes, pointing to the residual perovskite on top of the gold. The PbI_2^- ion map (**Figure 5.2**c) shows a similar trend with the I^- ion fragment map, being inverted to that of the Au^- ion map over the electrodes, due to the uneven sputtering to the buried plane. The Si^- ion fragment map (not shown) indicates that we have not sputtered through all of the perovskite material to the substrate. However, the homogenous distribution across the channel from the perovskite ion fragment maps (I^- and PbI_2^-) indicates that under no external bias, the perovskite is not underdoing decomposition and ion migration.

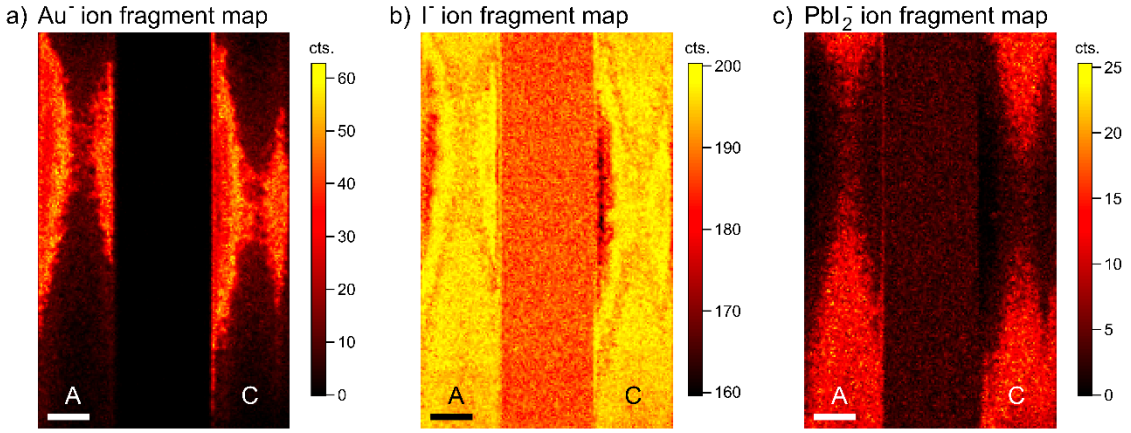

Figure 5.2 ToF-SIMS image maps for the unbiased device. ToF-SIMS ion fragment maps at the buried perovskite/gold interface for the unbiased lateral $MAPbI_3$ device for the (a) Au^-, (b) I^-, and (c) PbI_2^- ion fragments showing the gold anode (A) and cathode (C). Images are from 200 s of imaging; scale bar is 10 μm. The apparent X (or cross) on the electrodes is due to uneven sputtering to the buried plane.

To further see the homogeneity, **Figure 5.3**, gives summed line profiles across the whole image for each ion marker, each profile normalized to its maximum. In the device channel, the markers are relatively flat indicating a uniform matrix/composition. It is important to note that the changes in the Au^- line profile across the electrodes is due to uneven sputtering over the electrodes in revealing the buried perovskite/gold plane of interest. And, the spike at the edge of the cathode in the I^- ion fragment map is due to the same effect. The unbiased imaging confirms that under no external bias, the perovskite film does not degrade.

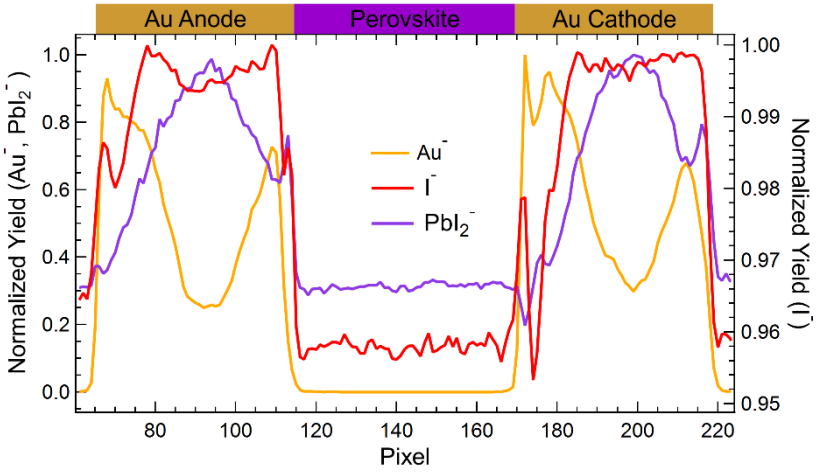

Figure 5.3 Line profiles for unbiased $MAPbI_3$ perovskite lateral devices. The profiles are the summed line scans across the whole image, normalized to each profile's maximum value.

5.2.2 Biased Imaging

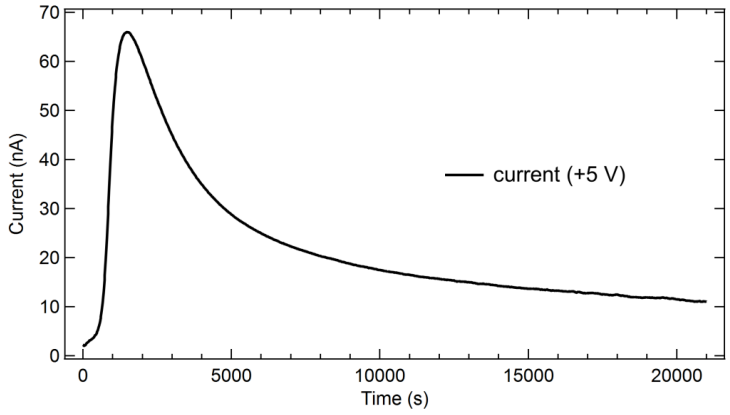

Figure 5.4 Non-uniform device current under bias. The lateral $MAPbI_3$ device current under bias (V = + 5 V) over time indicating ion migration.

In order to visualize ion migration, we then applied an external bias (+5 V = 0.25 V/μm) and imaged for ~21,000 s. **Figure 5.4** shows the current response over time. The shape of the curve is in agreement with previous studies,[96,104] where it is believed that ion migration causes the non-uniform current. As ions start to drift in the external bias and charge vacancies appear, the perovskite undergoes self-doping, which improves charge transport, increasing the external current collected. Over time as the availability of mobile ions decreases, the current plateaus and reduces to some final equilibrium state with no mobile ions.

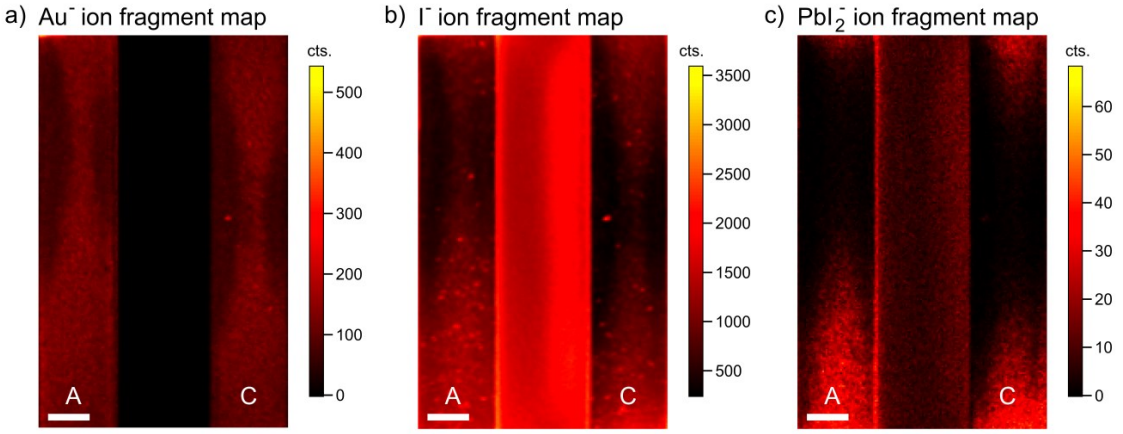

Figure 5.5 ToF-SIMS image maps for the biased device. ToF-SIMS ion fragment maps for biased (0.25 V/µm) lateral $MAPbI_3$ devices for the (a) Au^-, (b) I^-, and (c) PbI_2^- ion fragments showing the gold anode (A) and cathode (C) taken after ~21,000 s of imaging. Scale bar is 10 µm.

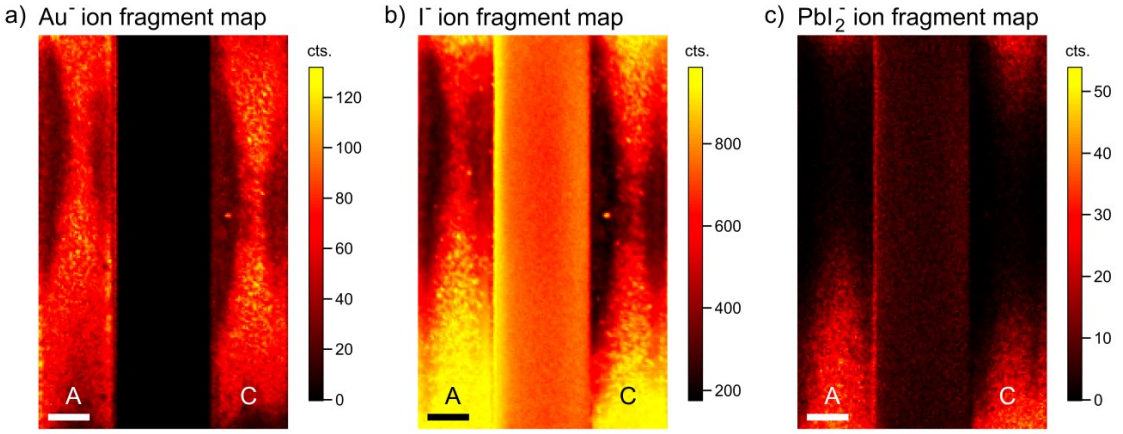

Figure 5.6 ToF-SIMS image maps for the biased device (first ~5000 s). ToF-SIMS ion fragment maps for biased (0.25 V/µm) lateral $MAPbI_3$ devices for the (a) Au^-, (b) I^-, and (c) PbI_2^- ion fragments showing the gold anode (A) and cathode (C) taken after the first ~5,000 s. Scale bar is 10 µm.

After biasing for ~21,000 s, the total image maps summed over the complete biasing time (**Figure 5.5**) now show a change in the perovskite layer. The Au^- ion fragment map (**Figure 5.5**a) shows no change in the gold electrodes, except for the removal of some of the previously exposed gold in the apparent cross. The other ion

fragment maps (I^-, PbI_2^-) show the non-uniformity (or inhomogeneity) in the perovskite layer indicating ion migration. Since the spike in current is believed to be from ion migration,[96,104] looking at the first ~5,000 s provides insight into this behavior. **Figure 5.6** gives the same image maps, but now just for the *first* ~5,000 s of imaging. Here, the gold signal is the same (Au^- ion fragment, **Figure 5.6**a) But, the perovskite ion fragment signals (I^- and PbI_2^-, **Figure 5.6**a,b) show that the inhomogeneity is already present, within the first ~5,000 s. Line profiles through these images, normalized to maximum, (**Figure 5.7**) show the extent of the inhomogeneity, where there is an increase in I^- and PbI_2^- near the anode and some depletion in the middle of the channel. These changes are in-line with iodide migration from the bulk perovskite to the anode in the applied electric field. Moreover, line profiles at different time points within the first 5,000 s show this migration. **Figure 5.8**a provides (*non*-normalized) line profiles and shows the progression of the I^- ion fragment image map over time with each line representing ~100 s of biasing corresponding to the dashed time intervals and color scheme depicted in **Figure 5.8**b. The decrease in signal over the electrodes shows the removal of perovskite from the electrodes over time. Interestingly, the intensity of the I^- ion fragment does not decrease at the anode at all, however it does in the center, showing the progression of I^- migration in the external electric field.

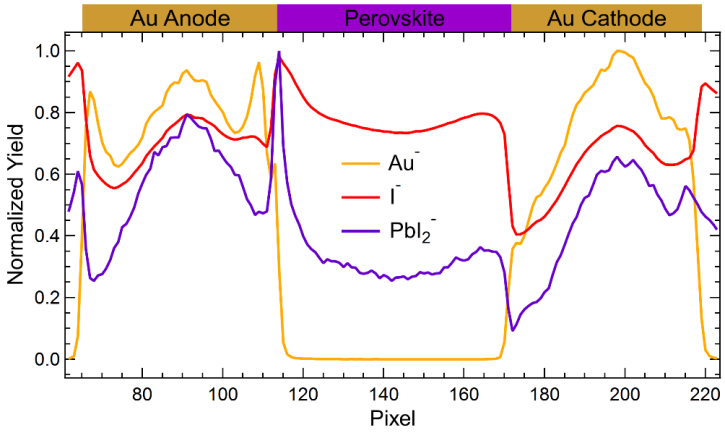

Figure 5.7 Line profiles through ion maps for biased $MAPbI_3$ lateral device after ~5000 s. The profiles are the summed line scans across the whole image, normalized to each profile's maximum value.

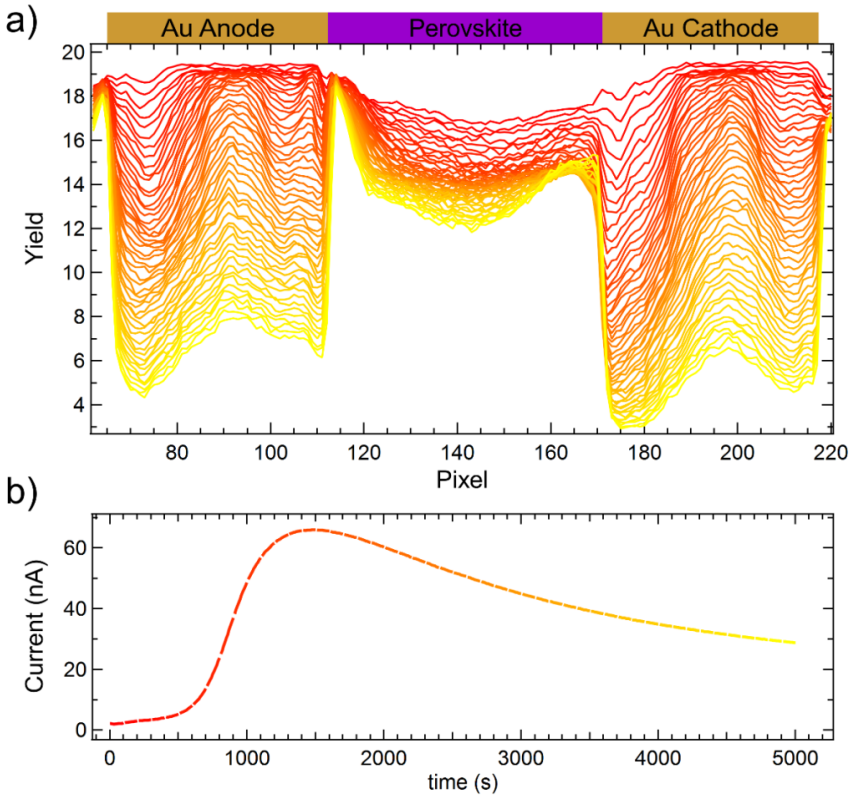

Figure 5.8 Time progression of I^- line profiles. Line profiles through I^- ion image map for the first ~5000 s, each line profile is 100 s of imaging showing the progression of the I^- signal over time.

Figure 5.9a shows select line profiles normalized to their intensity at the middle of the channel to exaggerate ion migration. The color scheme and selected time profiles (Profiles 0, 6, 11, 20, 30, 40, 49) correspond to the time intervals in **Figure 5.9**b. In this manner, the I^- ion yield at the anode continually increases over the whole ~5,000 s of biasing due to ion migration and proposed I^-/I^0 oxidation.[96] Maybe more intriguing is the increase of I^- yield at the cathode, which appears to occur at the end of the ~5,000 s (after time profiles 40). In combination with the working theory that the decrease in external current is due to the reduction in mobile ions in the device, it would suggest that the process at the cathode at this time is from electron injection at the cathode, creating I^-.

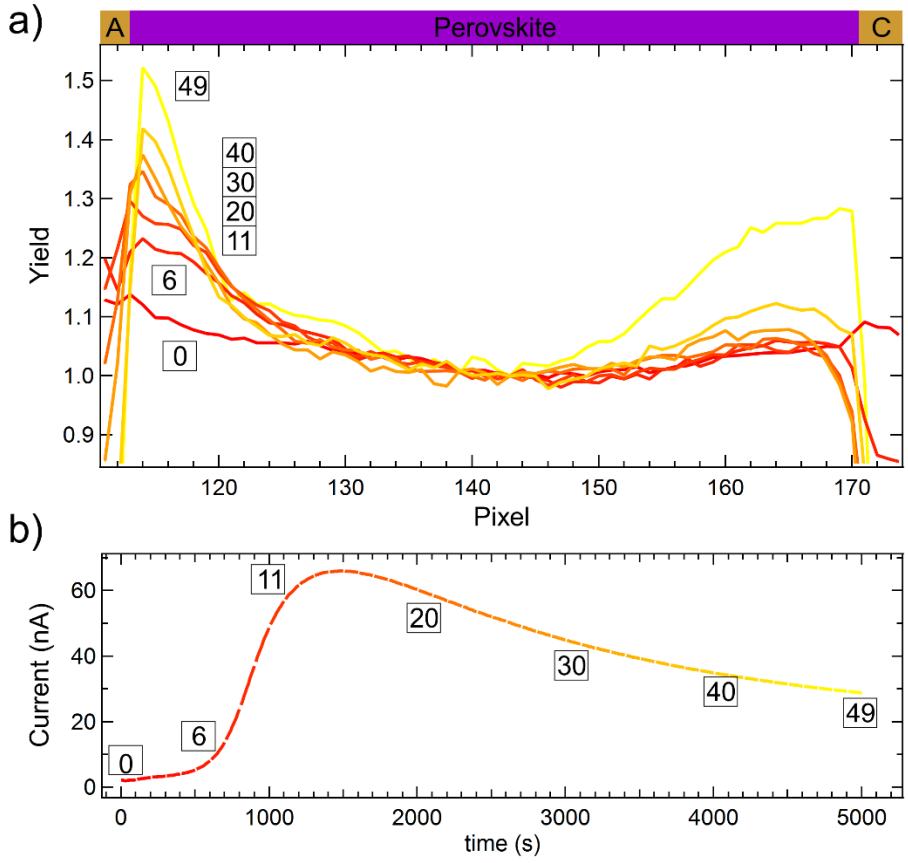

Figure 5.9 Select I^- line profiles. Select normalized line profiles through the biased I^- ion image maps showing progression of I^- ion migration to the anode.

5.3 CONCLUSIONS/OUTLOOK

Here, we have provided for a method to visualize *in situ* ion migration and electric field induced degradation in $MAPbI_3$ perovskites. Under no external bias, we see no signs of ion migration. However, under bias, we clearly see a chemical change in the perovskite. The ion migration that we see corresponds to I^- migration from the bulk of the perovskite channel to the device anode that progresses over time as the device permanently degrades. Our work shows this migration and supports the theory that iodide movement induces a non-uniform current in the device and that oxidation at the anode causes permanent degradation to the perovskite film.

Currently, we have shown only the response for collecting data in negative node, that is, negative polarity with respect to the ToF-SIMS extractor, which limits analysis to species that readily from negative ions. Continuing this study in positive mode in which other species of interest, that is, hydrogen cations or even methylammonium cations, could be analyzed, would give a more complete picture of ion migration in $MAPbI_3$ perovskite films. This work and future studies like it can help explain the nanoscale degradation pathways in these systems by directly visualizing in situ electric field induced degradation and ion migration.

5.4 MATERIALS AND METHODS

5.4.1 $MAPbI_3$ Perovskite Synthesis

Films of methylammonium lead iodide perovskite ($CH_3NH_3PbI_3$) were deposited onto the lateral devices according to a common antisolvent deposition procedure.[231] Briefly, the devices were first washed in dilute detergent solution (Contrex, 1% in water), then acetone, then isopropanol before being treated under UV/ozone for 25 min to

improve the hydrophilicity of the surface. The treated substrates were then immediately brought into a nitrogen glovebox (O_2 < 10 ppm, H_2O < 5 ppm) for perovskite deposition.

A 0.75 M solution of PbI_2 (TCI, 99.99%) and methylammonium iodide (GreatCell Solar) in a 4:1 (v/v) solution of dimethyl formamide (Acros Organics, 99.8%, extra dry) and dimethylsulfoxide (Acros Organics, 99.7%, extra dry) was prepared at least two days prior to film synthesis. Molarity is given in terms of lead content, and a stoichiometric ratio of 1:1 between lead iodide and methylammonium iodide was maintained. After loading the substrate onto the spin coater (Ossila) chuck, two drops of the above solution was filtered through a 0.2 μm PTFE filter and deposited onto the substrate, taking care to cover the entire surface. The spin coater was then ramped to 1000 rpm for 3 seconds, before ramping to 6000 rpm for 30s. At 6 s from the starts of the 6000 rpm step (9 s total) 150 μL of chlorobenzene (Acros Organics, 99.8%, extra dry) was deposited onto the substrate in one smooth movement.

After the end of the final spin coater step, the substrate was heated at 75 °C hotplate for roughly 1 min before being transferred to a 130 °C hotplate for a final 5 min of annealing, giving a final film thickness of ~170 nm. Surface coverage on electrodes was determined by AFM (Dimension 3100).

5.4.2 Lateral Device Fabrication

Lateral devices were fabricated using a method outlined previously[232] with some modifications. Each gold electrode (~ 80 nm thick) was fabricated individually to form a 20 μm channel. Our masks were developed for asymmetric electrodes so we had to perform two fabrication steps, first for the cathode and then for the anode, but the process is the same. We selected this order to make the second alignment step easier (it can be easier to align *to* the crosses in the second step). A silicon wafer (with ~300 nm thick

oxide) was piranha cleaned (3:1 sulfuric acid to 30% hydrogen peroxide) for 15 mins and rinsed with deionized (DI) water, then acetone, then isopropanol (IPA) and dried with house nitrogen. The electrodes were fabricated using an Image Reversal procedure to minimize edge sloping. To start, the wafer was O_2 plasma cleaned (50 ppm O_2, 120 W, 120 s) to remove any residual organic contaminants. Photoresist (AZ 5209E) was spun onto the wafer, ~1 um thick via spin-coating at 500 rpm (100 rpm/s) for 5 s and increasing to 4000 rpm (1000 rpm/s) for 60 s, and baked (90 °C for 150 s). Photolithography (Suss MA6 Mask Aligner) was performed with 2 exposures: (1) in hard contact mode for 3.2 s followed by a bake (115 °C for 150 s) and (2) a flood exposure of 18.4 s. Development was done using MF-26A developer for 1 min, agitating the solution every 20 s, followed by a thorough rinse with DI water. Here, a quick O_2 plasma clean (50 ppm O_2, 120 W, 15 s) was performed to tidy up development. To make the contacts, a thin layer of chromium (45 Å at 0.1 Å/s) was deposited followed by gold (first, 50 Å at 0.1 Å/s then, the remaining 750 Å at 0.1 Å/s) using e-beam deposition (Cooke EBeam). Lift-off was performed using piranha solution, adding the wafer *carefully* to freshly made solution, followed by rinses in DI water, then acetone, then IPA, and dried with nitrogen. Other solvents can be used for lift-off, if desired, such as acetone, then IPA, then water. The second electrode was deposited in the same manner, carefully aligning the mask markers. A dicing saw (Disco 321) was used to dice the completed wafer.

5.4.3 Electrical Measurements

All electrical measurements were performed using a Keithley 2400 sourcemeter with connections into either a N_2 filled glovebox or the ToF-SIMS analysis chamber and attached to a custom ToF-SIMS analysis stage with cooper wire connections to the

mounted device. The stage was purchased from ION-TOF and used with minor modifications.

5.4.4 ToF-SIMS Analysis/Imaging

For depth profiling and chemical analysis we used a TOF.SIMS 5 instrument (ION-TOF GmbH, Germany, 2010). During depth profiling the sputtering ion beam (Cs^+ at 500 eV ion energy and ~40 nA measured sample current) was raster scanned over an area of 300 x 300 μm^2. The analysis ion beam consisting of Bi_1^+ pulses (30 keV ion energy, 20 ns pulse duration, 3 pA measured sample current) was set in the high current bunched (HC) mode and raster scanned (random) over a 100 x 100 μm^2 area (256 pixels x 256 pixels) centered within the Cs^+ sputtered area at the regressing surface. The depth profiles were acquired in non-interlaced mode at a base pressure of 10^{-9} torr. All mass spectra were acquired in negative polarity while the mass resolution was >8000 ($m/\delta m$) for all fragments of interest.

For imaging, the analysis beam, Bi_1^+ pulses (30 keV ion energy, 50 ns pulse duration, ~0.3 pA sample current), was set in the Burst Alignment (BA) mode and raster scanned (sawtooth) over a 100 x 100 μm^2 area (256 pixels x 256 pixels) centered within the previously sputtered area. Imaging occurred at a base pressure of 10^{-9} torr. All mass spectra were acquired in negative polarity while the mass resolution was >300 ($m/\delta m$) for all fragments of interest.

References

(1) *International Energy Outlook 2017*; DOE/EIA-0484(2017); U.S. Energy Information Administration, 2017.

(2) Green, M. A.; Hishikawa, Y.; Dunlop, E. D.; Levi, D. H.; Hohl-Ebinger, J.; Ho-Baillie, A. W. Y. Solar Cell Efficiency Tables (Version 51). *Prog. Photovolt. Res. Appl.* **2018**, *26* (1), 3–12.

(3) *International Technology Roadmap for Photovoltaic (ITRPV)*; 8th ed.; Mechanical Engineering Industry Association (VDMA), 2017.

(4) Bagher, A. Comparison of Organic Solar Cells and Inorganic Solar Cells. *Int. J. Renew. Sustain. Energy* **2014**, *3* (3), 53–58.

(5) Green, M. A. Commercial Progress and Challenges for Photovoltaics. *Nat. Energy* **2016**, *1*, 15015.

(6) Habisreutinger, S. N.; McMeekin, D. P.; Snaith, H. J.; Nicholas, R. J. Research Update: Strategies for Improving the Stability of Perovskite Solar Cells. *APL Mater.* **2016**, *4* (9), 091503.

(7) Søndergaard, R.; Hösel, M.; Angmo, D.; Larsen-Olsen, T. T.; Krebs, F. C. Roll-to-Roll Fabrication of Polymer Solar Cells. *Mater. Today* **2012**, *15* (1), 36–49.

(8) Tzounis, L.; Stergiopoulos, T.; Zachariadis, A.; Gravalidis, C.; Laskarakis, A.; Logothetidis, S. Perovskite Solar Cells from Small Scale Spin Coating Process towards Roll-to-Roll Printing: Optical and Morphological Studies. *Mater. Today Proc.* **2017**, *4* (4, Part B), 5082–5089.

(9) Park, N.-G. Perovskite Solar Cells: An Emerging Photovoltaic Technology. *Mater. Today* **2015**, *18* (2), 65–72.

(10) De Wolf, S.; Holovsky, J.; Moon, S.-J.; Löper, P.; Niesen, B.; Ledinsky, M.; Haug, F.-J.; Yum, J.-H.; Ballif, C. Organometallic Halide Perovskites: Sharp Optical Absorption Edge and Its Relation to Photovoltaic Performance. *J. Phys. Chem. Lett.* **2014**, *5* (6), 1035–1039.

(11) Hoppe, H.; Sariciftci, N. S. Morphology of Polymer/Fullerene Bulk Heterojunction Solar Cells. *J. Mater. Chem.* **2006**, *16* (1), 45–61.

(12) Fakharuddin, A.; Schmidt-Mende, L.; Garcia-Belmonte, G.; Jose, R.; Mora-Sero, I. Interfaces in Perovskite Solar Cells. *Adv. Energy Mater.* **2017**, *7* (22), 1700623.

(13) Lunt, R. R.; Bulovic, V. Transparent, near-Infrared Organic Photovoltaic Solar Cells for Window and Energy-Scavenging Applications. *Appl. Phys. Lett.* **2011**, *98* (11), 113305.

(14) Zhao, J.; Li, Y.; Yang, G.; Jiang, K.; Lin, H.; Ade, H.; Ma, W.; Yan, H. Efficient Organic Solar Cells Processed from Hydrocarbon Solvents. *Nat. Energy* **2016**, *1*, 15027.

(15) Yang, W. S.; Park, B.-W.; Jung, E. H.; Jeon, N. J.; Kim, Y. C.; Lee, D. U.; Shin, S. S.; Seo, J.; Kim, E. K.; Noh, J. H.; et al. Iodide Management in

Formamidinium-Lead-Halide–based Perovskite Layers for Efficient Solar Cells. *Science* **2017**, *356* (6345), 1376–1379.
(16) Qiu, L.; Ono, L. K.; Qi, Y. Advances and Challenges to the Commercialization of Organic–inorganic Halide Perovskite Solar Cell Technology. *Mater. Today Energy* **2017**, 1–21.
(17) Jodlowski, A. D.; Roldán-Carmona, C.; Grancini, G.; Salado, M.; Ralaiarisoa, M.; Ahmad, S.; Koch, N.; Camacho, L.; de Miguel, G.; Nazeeruddin, M. K. Large Guanidinium Cation Mixed with Methylammonium in Lead Iodide Perovskites for 19% Efficient Solar Cells. *Nat. Energy* **2017**, *2* (12), 972–979.
(18) Li, D.; Liao, P.; Shai, X.; Huang, W.; Liu, S.; Li, H.; Shen, Y.; Wang, M. Recent Progress on Stability Issues of Organic–inorganic Hybrid Lead Perovskite-Based Solar Cells. *RSC Adv.* **2016**, *6* (92), 89356–89366.
(19) Liang, Y.; Yu, L. A New Class of Semiconducting Polymers for Bulk Heterojunction Solar Cells with Exceptionally High Performance. *Acc. Chem. Res.* **2010**, *43* (9), 1227–1236.
(20) Blouin, N.; Michaud, A.; Leclerc, M. A Low-Bandgap Poly(2,7-Carbazole) Derivative for Use in High-Performance Solar Cells. *Adv. Mater.* **2007**, *19* (17), 2295–2300.
(21) Scharber, M. C.; Koppe, M.; Gao, J.; Cordella, F.; Loi, M. A.; Denk, P.; Morana, M.; Egelhaaf, H.-J.; Forberich, K.; Dennler, G.; et al. Influence of the Bridging Atom on the Performance of a Low-Bandgap Bulk Heterojunction Solar Cell. *Adv. Mater.* **2010**, *22* (3), 367–370.
(22) Bronstein, H.; Chen, Z.; Shahid Ashraf, R.; Zhang, W.; Du, J.; Durrant, J. R.; Shakya Tuladhar, P.; Song, K.; Watkins, S. E.; Geerts, Y.; et al. Thieno[3,2-b]Thiophene−Diketopyrrolopyrrole-Containing Polymers for High-Performance Organic Field-Effect Transistors and Organic Photovoltaic Devices. *J. Am. Chem. Soc.* **2011**, *133* (10), 3272–3275.
(23) Liu, C.; Wang, K.; Gong, X.; Heeger, A. J. Low Bandgap Semiconducting Polymers for Polymeric Photovoltaics. *Chem. Soc. Rev.* **2016**, *45* (17), 4825–4846.
(24) Kan, B.; Li, M.; Zhang, Q.; Liu, F.; Wan, X.; Wang, Y.; Ni, W.; Long, G.; Yang, X.; Feng, H.; et al. A Series of Simple Oligomer-like Small Molecules Based on Oligothiophenes for Solution-Processed Solar Cells with High Efficiency. *J. Am. Chem. Soc.* **2015**, *137* (11), 3886–3893.
(25) Ma, W.; Yang, C.; Gong, X.; Lee, K.; Heeger, A. J. Thermally Stable, Efficient Polymer Solar Cells with Nanoscale Control of the Interpenetrating Network Morphology. *Adv. Funct. Mater.* **2005**, *15* (10), 1617–1622.
(26) Zhao, Y.; Xie, Z.; Qu, Y.; Geng, Y.; Wang, L. Solvent-Vapor Treatment Induced Performance Enhancement of Poly(3-Hexylthiophene):Methanofullerene Bulk-Heterojunction Photovoltaic Cells. *Appl. Phys. Lett.* **2007**, *90* (4), 043504.
(27) Peet, J.; Kim, J. Y.; Coates, N. E.; Ma, W. L.; Moses, D.; Heeger, A. J.; Bazan, G. C. Efficiency Enhancement in Low-Bandgap Polymer Solar Cells by Processing with Alkane Dithiols. *Nat. Mater.* **2007**, *6* (7), 497–500.

(28) Lee, J. K.; Ma, W. L.; Brabec, C. J.; Yuen, J.; Moon, J. S.; Kim, J. Y.; Lee, K.; Bazan, G. C.; Heeger, A. J. Processing Additives for Improved Efficiency from Bulk Heterojunction Solar Cells. *J. Am. Chem. Soc.* **2008**, *130* (11), 3619–3623.
(29) Park, S. H.; Roy, A.; Beaupré, S.; Cho, S.; Coates, N.; Moon, J. S.; Moses, D.; Leclerc, M.; Lee, K.; Heeger, A. J. Bulk Heterojunction Solar Cells with Internal Quantum Efficiency Approaching 100%. *Nat. Photonics* **2009**, *3* (5), 297–302.
(30) van Bavel, S. S.; Bärenklau, M.; de With, G.; Hoppe, H.; Loos, J. P3HT/PCBM Bulk Heterojunction Solar Cells: Impact of Blend Composition and 3D Morphology on Device Performance. *Adv. Funct. Mater.* **2010**, *20* (9), 1458–1463.
(31) Sista, S.; Park, M.-H.; Hong, Z.; Wu, Y.; Hou, J.; Kwan, W. L.; Li, G.; Yang, Y. Highly Efficient Tandem Polymer Photovoltaic Cells. *Adv. Mater.* **2010**, *22* (3), 380–383.
(32) You, J.; Dou, L.; Yoshimura, K.; Kato, T.; Ohya, K.; Moriarty, T.; Emery, K.; Chen, C.-C.; Gao, J.; Li, G.; et al. A Polymer Tandem Solar Cell with 10.6% Power Conversion Efficiency. *Nat. Commun.* **2013**, *4*, 1446.
(33) Xiao, X.; Lee, K.; Forrest, S. R. Scalability of Multi-Junction Organic Solar Cells for Large Area Organic Solar Modules. *Appl. Phys. Lett.* **2015**, *106*, 213301.
(34) Jeon, N. J.; Noh, J. H.; Yang, W. S.; Kim, Y. C.; Ryu, S.; Seo, J.; Seok, S. I. Compositional Engineering of Perovskite Materials for High-Performance Solar Cells. *Nature* **2015**, *517* (7535), 476–480.
(35) Eperon, G. E.; Paternò, G. M.; Sutton, R. J.; Zampetti, A.; Haghighirad, A. A.; Cacialli, F.; Snaith, H. J. Inorganic Caesium Lead Iodide Perovskite Solar Cells. *J. Mater. Chem. A* **2015**, *3* (39), 19688–19695.
(36) Kulbak, M.; Gupta, S.; Kedem, N.; Levine, I.; Bendikov, T.; Hodes, G.; Cahen, D. Cesium Enhances Long-Term Stability of Lead Bromide Perovskite-Based Solar Cells. *J. Phys. Chem. Lett.* **2016**, *7* (1), 167–172.
(37) Sutton, R. J.; Eperon, G. E.; Miranda, L.; Parrott, E. S.; Kamino, B. A.; Patel, J. B.; Hörantner, M. T.; Johnston, M. B.; Haghighirad, A. A.; Moore, D. T.; et al. Bandgap-Tunable Cesium Lead Halide Perovskites with High Thermal Stability for Efficient Solar Cells. *Adv. Energy Mater.* **2016**, *6* (8), 1502458.
(38) Pellet, N.; Gao, P.; Gregori, G.; Yang, T.-Y.; Nazeeruddin, M. K.; Maier, J.; Grätzel, M. Mixed-Organic-Cation Perovskite Photovoltaics for Enhanced Solar-Light Harvesting. *Angew. Chem. Int. Ed.* **2014**, *53* (12), 3151–3157.
(39) Abate, A. Perovskite Solar Cells Go Lead Free. *Joule* **2017**, *1* (4), 659–664.
(40) Noh, J. H.; Im, S. H.; Heo, J. H.; Mandal, T. N.; Seok, S. I. Chemical Management for Colorful, Efficient, and Stable Inorganic-Organic Hybrid Nanostructured Solar Cells. *Nano Lett.* **2013**, *13* (4), 1764–1769.
(41) Jiang, Q.; Rebollar, D.; Gong, J.; Piacentino, E. L.; Zheng, C.; Xu, T. Pseudohalide-Induced Moisture Tolerance in Perovskite CH3NH3Pb(SCN)2I Thin Films. *Angew. Chem. Int. Ed.* **2015**, *54* (26), 7617–7620.
(42) Tombe, S.; Adam, G.; Heilbrunner, H.; Apaydin, D. H.; Ulbricht, C.; Sariciftci, N. S.; Arendse, C. J.; Iwuoha, E.; Scharber, M. C. Optical and Electronic

Properties of Mixed Halide (X = I, Cl, Br) Methylammonium Lead Perovskite Solar Cells. *J. Mater. Chem. C* **2017**, *5* (7), 1714–1723.
(43) Tai, Q.; You, P.; Sang, H.; Liu, Z.; Hu, C.; Chan, H. L. W.; Yan, F. Efficient and Stable Perovskite Solar Cells Prepared in Ambient Air Irrespective of the Humidity. *Nat. Commun.* **2016**, *7*, 11105.
(44) Colella, S.; Mosconi, E.; Fedeli, P.; Listorti, A.; Gazza, F.; Orlandi, F.; Ferro, P.; Besagni, T.; Rizzo, A.; Calestani, G.; et al. MAPbI3-XClx Mixed Halide Perovskite for Hybrid Solar Cells: The Role of Chloride as Dopant on the Transport and Structural Properties. *Chem. Mater.* **2013**, *25* (22), 4613–4618.
(45) Kim, H.-S.; Lee, C.-R.; Im, J.-H.; Lee, K.-B.; Moehl, T.; Marchioro, A.; Moon, S.-J.; Humphry-Baker, R.; Yum, J.-H.; Moser, J. E.; et al. Lead Iodide Perovskite Sensitized All-Solid-State Submicron Thin Film Mesoscopic Solar Cell with Efficiency Exceeding 9%. *Sci. Rep.* **2012**, *2*, 591.
(46) Lee, M. M.; Teuscher, J.; Miyasaka, T.; Murakami, T. N.; Snaith, H. J. Efficient Hybrid Solar Cells Based on Meso-Superstructured Organometal Halide Perovskites. *Science* **2012**, *338* (6107), 643–647.
(47) Yang, W. S.; Noh, J. H.; Jeon, N. J.; Kim, Y. C.; Ryu, S.; Seo, J.; Seok, S. I. High-Performance Photovoltaic Perovskite Layers Fabricated through Intramolecular Exchange. *Science* **2015**, *348* (6240), 1234–1237.
(48) Jeon, N. J.; Noh, J. H.; Kim, Y. C.; Yang, W. S.; Ryu, S.; Seok, S. I. Solvent Engineering for High-Performance Inorganic–organic Hybrid Perovskite Solar Cells. *Nat. Mater.* **2014**, *13* (9), 897–903.
(49) Mei, A.; Li, X.; Liu, L.; Ku, Z.; Liu, T.; Rong, Y.; Xu, M.; Hu, M.; Chen, J.; Yang, Y.; et al. A Hole-Conductor–free, Fully Printable Mesoscopic Perovskite Solar Cell with High Stability. *Science* **2014**, *345* (6194), 295–298.
(50) Heo, J. H.; Im, S. H.; Noh, J. H.; Mandal, T. N.; Lim, C.-S.; Chang, J. A.; Lee, Y. H.; Kim, H.; Sarkar, A.; Nazeeruddin, M. K.; et al. Efficient Inorganic–organic Hybrid Heterojunction Solar Cells Containing Perovskite Compound and Polymeric Hole Conductors. *Nat. Photonics* **2013**, *7* (6), 486–491.
(51) Green, M. A.; Ho-Baillie, A.; Snaith, H. J. The Emergence of Perovskite Solar Cells. *Nat. Photonics* **2014**, *8* (7), 506–514.
(52) Akbulatov, A. F.; Frolova, L. A.; Griffin, M. P.; Gearba, I. R.; Dolocan, A.; Vanden Bout, D. A.; Tsarev, S.; Katz, E. A.; Shestakov, A. F.; Stevenson, K. J.; et al. Effect of Electron-Transport Material on Light-Induced Degradation of Inverted Planar Junction Perovskite Solar Cells. *Adv. Energy Mater.* **2017**, *7*, 1700476.
(53) Zhao, Z.; Gu, F.; Li, Y.; Sun, W.; Ye, S.; Rao, H.; Liu, Z.; Bian, Z.; Huang, C. Mixed-Organic-Cation Tin Iodide for Lead-Free Perovskite Solar Cells with an Efficiency of 8.12%. *Adv. Sci.* **2017**, *4* (11), 1700204.
(54) Nelson, J. Polymer:Fullerene Bulk Heterojunction Solar Cells. *Mater. Today* **2011**, *14* (10), 462–470.

(55) Yang, X.; Loos, J.; Veenstra, S. C.; Verhees, W. J. H.; Wienk, M. M.; Kroon, J. M.; Michels, M. A. J.; Janssen, R. A. J. Nanoscale Morphology of High-Performance Polymer Solar Cells. *Nano Lett.* **2005**, *5* (4), 579–583.
(56) van Bavel, S. S.; Sourty, E.; With, G. de; Loos, J. Three-Dimensional Nanoscale Organization of Bulk Heterojunction Polymer Solar Cells. *Nano Lett.* **2009**, *9* (2), 507–513.
(57) Jo, J.; Na, S.-I.; Kim, S.-S.; Lee, T.-W.; Chung, Y.; Kang, S.-J.; Vak, D.; Kim, D.-Y. Three-Dimensional Bulk Heterojunction Morphology for Achieving High Internal Quantum Efficiency in Polymer Solar Cells. *Adv. Funct. Mater.* **2009**, *19* (15), 2398–2406.
(58) Kim, Y.; Choulis, S. A.; Nelson, J.; Bradley, D. D. C.; Cook, S.; Durrant, J. R. Device Annealing Effect in Organic Solar Cells with Blends of Regioregular Poly(3-Hexylthiophene) and Soluble Fullerene. *Appl. Phys. Lett.* **2005**, *86* (6), 063502.
(59) Li, G.; Shrotriya, V.; Huang, J.; Yao, Y.; Moriarty, T.; Emery, K.; Yang, Y. High-Efficiency Solution Processable Polymer Photovoltaic Cells by Self-Organization of Polymer Blends. *Nat. Mater.* **2005**, *4* (11), 864–868.
(60) Mihailetchi, V. D.; Xie, H.; Boer, B. de; Popescu, L. M.; Hummelen, J. C.; Blom, P. W. M.; Koster, L. J. A. Origin of the Enhanced Performance in Poly(3-Hexylthiophene): [6,6]-Phenyl C61-Butyric Acid Methyl Ester Solar Cells upon Slow Drying of the Active Layer. *Appl. Phys. Lett.* **2006**, *89* (1), 012107.
(61) Mayer, A. C.; Toney, M. F.; Scully, S. R.; Rivnay, J.; Brabec, C. J.; Scharber, M.; Koppe, M.; Heeney, M.; McCulloch, I.; McGehee, M. D. Bimolecular Crystals of Fullerenes in Conjugated Polymers and the Implications of Molecular Mixing for Solar Cells. *Adv. Funct. Mater.* **2009**, *19* (8), 1173–1179.
(62) Chen, H.-Y.; Yang, H.; Yang, G.; Sista, S.; Zadoyan, R.; Li, G.; Yang, Y. Fast-Grown Interpenetrating Network in Poly(3-Hexylthiophene): Methanofullerenes Solar Cells Processed with Additive. *J. Phys. Chem. C* **2009**, *113* (18), 7946–7953.
(63) Hoppe, H.; Sariciftci, N. S. Organic Solar Cells: An Overview. *J. Mater. Res.* **2004**, *19* (07), 1924–1945.
(64) Chen, W.; Xu, T.; He, F.; Wang, W.; Wang, C.; Strzalka, J.; Liu, Y.; Wen, J.; Miller, D. J.; Chen, J.; et al. Hierarchical Nanomorphologies Promote Exciton Dissociation in Polymer/Fullerene Bulk Heterojunction Solar Cells. *Nano Lett.* **2011**, *11* (9), 3707–3713.
(65) Brütting, W. Introduction to the Physics of Organic Semiconductors. In *Physics of Organic Semiconductors*; Wiley-VCH: Germany, 2005; pp 1–14.
(66) Pfannmöller, M.; Flügge, H.; Benner, G.; Wacker, I.; Sommer, C.; Hanselmann, M.; Schmale, S.; Schmidt, H.; Hamprecht, F. A.; Rabe, T.; et al. Visualizing a Homogeneous Blend in Bulk Heterojunction Polymer Solar Cells by Analytical Electron Microscopy. *Nano Lett.* **2011**, *11* (8), 3099–3107.

(67) Chen, D.; Nakahara, A.; Wei, D.; Nordlund, D.; Russell, T. P. P3HT/PCBM Bulk Heterojunction Organic Photovoltaics: Correlating Efficiency and Morphology. *Nano Lett.* **2011**, *11* (2), 561–567.
(68) Son, H. J.; Wang, W.; Xu, T.; Liang, Y.; Wu, Y.; Li, G.; Yu, L. Synthesis of Fluorinated Polythienothiophene-Co-Benzodithiophenes and Effect of Fluorination on the Photovoltaic Properties. *J. Am. Chem. Soc.* **2011**, *133* (6), 1885–1894.
(69) Scarongella, M.; De Jonghe-Risse, J.; Buchaca-Domingo, E.; Causa', M.; Fei, Z.; Heeney, M.; Moser, J.-E.; Stingelin, N.; Banerji, N. A Close Look at Charge Generation in Polymer:Fullerene Blends with Microstructure Control. *J. Am. Chem. Soc.* **2015**, *137* (8), 2908–2918.
(70) Zhong, C.; Bartelt, J. A.; McGehee, M. D.; Cao, D.; Huang, F.; Cao, Y.; Heeger, A. J. Influence of Intermixed Donor and Acceptor Domains on the Ultrafast Charge Generation in Bulk Heterojunction Materials. *J. Phys. Chem. C* **2015**, *119* (48), 26889–26894.
(71) Collins, B. A.; Gann, E.; Guignard, L.; He, X.; McNeill, C. R.; Ade, H. Molecular Miscibility of Polymer−Fullerene Blends. *J. Phys. Chem. Lett.* **2010**, *1* (21), 3160–3166.
(72) Liu, Y.; Zhao, J.; Li, Z.; Mu, C.; Ma, W.; Hu, H.; Jiang, K.; Lin, H.; Ade, H.; Yan, H. Aggregation and Morphology Control Enables Multiple Cases of High-Efficiency Polymer Solar Cells. *Nat. Commun.* **2014**, *5*, 5293.
(73) Finck, B. Y.; Schwartz, B. J. Drift-Diffusion Studies of Compositional Morphology in Bulk Heterojunctions: The Role of the Mixed Phase in Photovoltaic Performance. *Phys. Rev. Appl.* **2016**, *6* (5), 054008.
(74) Chakhmouradian, A. R.; Woodward, P. M. Celebrating 175 Years of Perovskite Research: A Tribute to Roger H. Mitchell. *Phys. Chem. Miner.* **2014**, *41* (6), 387–391.
(75) Kojima, A.; Teshima, K.; Shirai, Y.; Miyasaka, T. Organometal Halide Perovskites as Visible-Light Sensitizers for Photovoltaic Cells. *J. Am. Chem. Soc.* **2009**, *131* (17), 6050–6051.
(76) Kim, H.; Lim, K.-G.; Lee, T.-W. Planar Heterojunction Organometal Halide Perovskite Solar Cells: Roles of Interfacial Layers. *Energy Environ. Sci.* **2016**, *9* (1), 12–30.
(77) Stranks, S. D.; Eperon, G. E.; Grancini, G.; Menelaou, C.; Alcocer, M. J. P.; Leijtens, T.; Herz, L. M.; Petrozza, A.; Snaith, H. J. Electron-Hole Diffusion Lengths Exceeding 1 Micrometer in an Organometal Trihalide Perovskite Absorber. *Science* **2013**, *342* (6156), 341–344.
(78) D'Innocenzo, V.; Grancini, G.; Alcocer, M. J. P.; Kandada, A. R. S.; Stranks, S. D.; Lee, M. M.; Lanzani, G.; Snaith, H. J.; Petrozza, A. Excitons versus Free Charges in Organo-Lead Tri-Halide Perovskites. *Nat. Commun.* **2014**, *5*, 3586.
(79) Chen, Y.; He, M.; Peng, J.; Sun, Y.; Liang, Z. Structure and Growth Control of Organic–Inorganic Halide Perovskites for Optoelectronics: From Polycrystalline Films to Single Crystals. *Adv. Sci.* **2016**, *3* (4), 1500392.

(80) Fan, R.; Huang, Y.; Wang, L.; Li, L.; Zheng, G.; Zhou, H. The Progress of Interface Design in Perovskite-Based Solar Cells. *Adv. Energy Mater.* **2016**, *6* (17), 1600460.
(81) Luchkin, S. Y.; Akbulatov, A. F.; Frolova, L. A.; Griffin, M. P.; Dolocan, A.; Gearba, R.; Vanden Bout, D. A.; Troshin, P. A.; Stevenson, K. J. Reversible and Irreversible Electric Field Induced Morphological and Interfacial Transformations of Hybrid Lead Iodide Perovskites. *ACS Appl. Mater. Interfaces* **2017**, *9* (39), 33478–33483.
(82) Nagabhushana, G. P.; Shivaramaiah, R.; Navrotsky, A. Direct Calorimetric Verification of Thermodynamic Instability of Lead Halide Hybrid Perovskites. *Proc. Natl. Acad. Sci.* **2016**, *113* (28), 7717–7721.
(83) Niu, G.; Li, W.; Meng, F.; Wang, L.; Dong, H.; Qiu, Y. Study on the Stability of CH3NH3PbI3 Films and the Effect of Post-Modification by Aluminum Oxide in All-Solid-State Hybrid Solar Cells. *J. Mater. Chem. A* **2013**, *2* (3), 705–710.
(84) Christians, J. A.; Miranda Herrera, P. A.; Kamat, P. V. Transformation of the Excited State and Photovoltaic Efficiency of CH3NH3PbI3 Perovskite upon Controlled Exposure to Humidified Air. *J. Am. Chem. Soc.* **2015**, *137* (4), 1530–1538.
(85) Frost, J. M.; Butler, K. T.; Brivio, F.; Hendon, C. H.; van Schilfgaarde, M.; Walsh, A. Atomistic Origins of High-Performance in Hybrid Halide Perovskite Solar Cells. *Nano Lett.* **2014**, *14* (5), 2584–2590.
(86) Hu, Q.; Liu, Y.; Li, Y.; Ying, L.; Liu, T.; Huang, F.; Wang, S.; Huang, W.; Zhu, R.; Gong, Q. Efficient and Low-Temperature Processed Perovskite Solar Cells Based on a Cross-Linkable Hybrid Interlayer. *J. Mater. Chem. A* **2015**, *3* (36), 18483–18491.
(87) Cao, J.; Yin, J.; Yuan, S.; Zhao, Y.; Li, J.; Zheng, N. Thiols as Interfacial Modifiers to Enhance the Performance and Stability of Perovskite Solar Cells. *Nanoscale* **2015**, *7* (21), 9443–9447.
(88) Zhang, J.; Hu, Z.; Huang, L.; Yue, G.; Liu, J.; Lu, X.; Hu, Z.; Shang, M.; Han, L.; Zhu, Y. Bifunctional Alkyl Chain Barriers for Efficient Perovskite Solar Cells. *Chem. Commun.* **2015**, *51* (32), 7047–7050.
(89) Zhao, Y.; Wei, J.; Li, H.; Yan, Y.; Zhou, W.; Yu, D.; Zhao, Q. A Polymer Scaffold for Self-Healing Perovskite Solar Cells. *Nat. Commun.* **2016**, *7*, 10228.
(90) Li, X.; Ibrahim Dar, M.; Yi, C.; Luo, J.; Tschumi, M.; Zakeeruddin, S. M.; Nazeeruddin, M. K.; Han, H.; Grätzel, M. Improved Performance and Stability of Perovskite Solar Cells by Crystal Crosslinking with Alkylphosphonic Acid ω-Ammonium Chlorides. *Nat. Chem.* **2015**, *7* (9), 703–711.
(91) Leijtens, T.; Eperon, G. E.; Pathak, S.; Abate, A.; Lee, M. M.; Snaith, H. J. Overcoming Ultraviolet Light Instability of Sensitized TiO_2 with Meso-Superstructured Organometal Tri-Halide Perovskite Solar Cells. *Nat. Commun.* **2013**, *4*, 2885.

(92) Guerrero, A.; You, J.; Aranda, C.; Kang, Y. S.; Garcia-Belmonte, G.; Zhou, H.; Bisquert, J.; Yang, Y. Interfacial Degradation of Planar Lead Halide Perovskite Solar Cells. *ACS Nano* **2016**, *10* (1), 218–224.
(93) Ito, S.; Tanaka, S.; Manabe, K.; Nishino, H. Effects of Surface Blocking Layer of Sb2S3 on Nanocrystalline TiO2 for CH3NH3PbI3 Perovskite Solar Cells. *J. Phys. Chem. C* **2014**, *118* (30), 16995–17000.
(94) Li, C.-Z.; Chang, C.-Y.; Zang, Y.; Ju, H.-X.; Chueh, C.-C.; Liang, P.-W.; Cho, N.; Ginger, D. S.; Jen, A. K.-Y. Suppressed Charge Recombination in Inverted Organic Photovoltaics via Enhanced Charge Extraction by Using a Conductive Fullerene Electron Transport Layer. *Adv. Mater.* **2014**, *26* (36), 6262–6267.
(95) Li, W.; Zhang, W.; Reenen, S. V.; Sutton, R. J.; Fan, J.; Haghighirad, A. A.; Johnston, M. B.; Wang, L.; Snaith, H. J. Enhanced UV-Light Stability of Planar Heterojunction Perovskite Solar Cells with Caesium Bromide Interface Modification. *Energy Environ. Sci.* **2016**, *9* (2), 490–498.
(96) Frolova, L. A.; Dremova, N. N.; Troshin, P. A. The Chemical Origin of the P-Type and n-Type Doping Effects in the Hybrid Methylammonium–lead Iodide (MAPbI3) Perovskite Solar Cells. *Chem. Commun.* **2015**, *51* (80), 14917–14920.
(97) Eames, C.; Frost, J. M.; Barnes, P. R. F.; O'Regan, B. C.; Walsh, A.; Islam, M. S. Ionic Transport in Hybrid Lead Iodide Perovskite Solar Cells. *Nat. Commun.* **2015**, *6*, 7497.
(98) Shao, Y.; Xiao, Z.; Bi, C.; Yuan, Y.; Huang, J. Origin and Elimination of Photocurrent Hysteresis by Fullerene Passivation in CH3NH3PbI3 Planar Heterojunction Solar Cells. *Nat. Commun.* **2014**, *5*, 5784.
(99) Juarez-Perez, E. J.; Sanchez, R. S.; Badia, L.; Garcia-Belmonte, G.; Kang, Y. S.; Mora-Sero, I.; Bisquert, J. Photoinduced Giant Dielectric Constant in Lead Halide Perovskite Solar Cells. *J. Phys. Chem. Lett.* **2014**, *5* (13), 2390–2394.
(100) Wei, J.; Zhao, Y.; Li, H.; Li, G.; Pan, J.; Xu, D.; Zhao, Q.; Yu, D. Hysteresis Analysis Based on the Ferroelectric Effect in Hybrid Perovskite Solar Cells. *J. Phys. Chem. Lett.* **2014**, *5* (21), 3937–3945.
(101) Kim, H.-S.; Jang, I.-H.; Ahn, N.; Choi, M.; Guerrero, A.; Bisquert, J.; Park, N.-G. Control of I–V Hysteresis in CH3NH3PbI3 Perovskite Solar Cell. *J. Phys. Chem. Lett.* **2015**, *6* (22), 4633–4639.
(102) Levine, I.; Nayak, P. K.; Wang, J. T.-W.; Sakai, N.; Van Reenen, S.; Brenner, T. M.; Mukhopadhyay, S.; Snaith, H. J.; Hodes, G.; Cahen, D. Interface-Dependent Ion Migration/Accumulation Controls Hysteresis in MAPbI3 Solar Cells. *J. Phys. Chem. C* **2016**, *120* (30), 16399–16411.
(103) Almora, O.; Zarazua, I.; Mas-Marza, E.; Mora-Sero, I.; Bisquert, J.; Garcia-Belmonte, G. Capacitive Dark Currents, Hysteresis, and Electrode Polarization in Lead Halide Perovskite Solar Cells. *J. Phys. Chem. Lett.* **2015**, *6* (9), 1645–1652.
(104) Xiao, Z.; Yuan, Y.; Shao, Y.; Wang, Q.; Dong, Q.; Bi, C.; Sharma, P.; Gruverman, A.; Huang, J. Giant Switchable Photovoltaic Effect in Organometal Trihalide Perovskite Devices. *Nat. Mater.* **2015**, *14* (2), 193–198.

(105) Yuan, Y.; Chae, J.; Shao, Y.; Wang, Q.; Xiao, Z.; Centrone, A.; Huang, J. Photovoltaic Switching Mechanism in Lateral Structure Hybrid Perovskite Solar Cells. *Adv. Energy Mater.* **2015**, *5* (15), 201500615.
(106) Jeangros, Q.; Duchamp, M.; Werner, J.; Kruth, M.; Dunin-Borkowski, R. E.; Niesen, B.; Ballif, C.; Hessler-Wyser, A. In Situ TEM Analysis of Organic–Inorganic Metal-Halide Perovskite Solar Cells under Electrical Bias. *Nano Lett.* **2016**, *16* (11), 7013–7018.
(107) Park, S.; Jeong, J.; Hyun, G.; Kim, M.; Lee, H.; Yi, Y. The Origin of High PCE in PTB7 Based Photovoltaics: Proper Charge Neutrality Level and Free Energy of Charge Separation at PTB7/PC71BM Interface. *Sci. Rep.* **2016**, *6*, 35262.
(108) Ono, L. K.; Qi, Y. Surface and Interface Aspects of Organometal Halide Perovskite Materials and Solar Cells. *J. Phys. Chem. Lett.* **2016**, *7* (22), 4764–4794.
(109) Grancini, G.; Polli, D.; Fazzi, D.; Cabanillas-Gonzalez, J.; Cerullo, G.; Lanzani, G. Transient Absorption Imaging of P3HT:PCBM Photovoltaic Blend: Evidence For Interfacial Charge Transfer State. *J. Phys. Chem. Lett.* **2011**, *2* (9), 1099–1105.
(110) Wu, X.; Trinh, M. T.; Niesner, D.; Zhu, H.; Norman, Z.; Owen, J. S.; Yaffe, O.; Kudisch, B. J.; Zhu, X.-Y. Trap States in Lead Iodide Perovskites. *J. Am. Chem. Soc.* **2015**, *137* (5), 2089–2096.
(111) Jailaubekov, A. E.; Willard, A. P.; Tritsch, J. R.; Chan, W.-L.; Sai, N.; Gearba, R.; Kaake, L. G.; Williams, K. J.; Leung, K.; Rossky, P. J.; et al. Hot Charge-Transfer Excitons Set the Time Limit for Charge Separation at Donor/Acceptor Interfaces in Organic Photovoltaics. *Nat. Mater.* **2012**, *12*, 66.
(112) Xu, J.; Buin, A.; Ip, A. H.; Li, W.; Voznyy, O.; Comin, R.; Yuan, M.; Jeon, S.; Ning, Z.; McDowell, J. J.; et al. Perovskite–fullerene Hybrid Materials Suppress Hysteresis in Planar Diodes. *Nat. Commun.* **2015**, *6*, 7081.
(113) Griffin, M. P.; Gearba, R.; Stevenson, K. J.; Vanden Bout, D. A.; Dolocan, A. Revealing the Chemistry and Morphology of Buried Donor/Acceptor Interfaces in Organic Photovoltaics. *J. Phys. Chem. Lett.* **2017**, 2764–2773.
(114) Alekseev, A.; Hedley, G. J.; Al-Afeef, A.; Ageev, O. A.; Samuel, I. D. W. Morphology and Local Electrical Properties of PTB7:PC71BM Blends. *J. Mater. Chem. A* **2015**, *3* (16), 8706–8714.
(115) Parnell, A. J.; Dunbar, A. D. F.; Pearson, A. J.; Staniec, P. A.; Dennison, A. J. C.; Hamamatsu, H.; Skoda, M. W. A.; Lidzey, D. G.; Jones, R. A. L. Depletion of PCBM at the Cathode Interface in P3HT/PCBM Thin Films as Quantified via Neutron Reflectivity Measurements. *Adv. Mater.* **2010**, *22* (22), 2444–2447.
(116) Bergmann, V. W.; Weber, S. A. L.; Javier Ramos, F.; Nazeeruddin, M. K.; Grätzel, M.; Li, D.; Domanski, A. L.; Lieberwirth, I.; Ahmad, S.; Berger, R. Real-Space Observation of Unbalanced Charge Distribution inside a Perovskite-Sensitized Solar Cell. *Nat. Commun.* **2014**, *5*, 5001.
(117) Hoppe, H.; Glatzel, T.; Niggemann, M.; Schwinger, W.; Schaeffler, F.; Hinsch, A.; Lux-Steiner, M. C.; Sariciftci, N. S. Efficiency Limiting Morphological

Factors of MDMO-PPV:PCBM Plastic Solar Cells. *Thin Solid Films* **2006**, *511–512*, 587–592.
(118) Kedem, N.; Brenner, T. M.; Kulbak, M.; Schaefer, N.; Levcenko, S.; Levine, I.; Abou-Ras, D.; Hodes, G.; Cahen, D. Light-Induced Increase of Electron Diffusion Length in a P–n Junction Type CH3NH3PbBr3 Perovskite Solar Cell. *J. Phys. Chem. Lett.* **2015**, *6* (13), 2469–2476.
(119) Gutierrez, M.; Slobodyan, O.; Dodabalapur, A.; Vanden Bout, D. A. Using Lateral Bulk Heterojunctions to Study the Effects of Additives on PTB7:PC61BM Space Charge Regions. *Synth. Met.* **2015**, *209*, 158–163.
(120) Huang, W.; Huang, F.; Gann, E.; Cheng, Y.-B.; McNeill, C. R. Probing Molecular and Crystalline Orientation in Solution-Processed Perovskite Solar Cells. *Adv. Funct. Mater.* **2015**, *25* (34), 5529–5536.
(121) Mukherjee, S.; Proctor, C. M.; Bazan, G. C.; Nguyen, T.-Q.; Ade, H. Significance of Average Domain Purity and Mixed Domains on the Photovoltaic Performance of High-Efficiency Solution-Processed Small-Molecule BHJ Solar Cells. *Adv. Energy Mater.* **2015**, *5* (21), 1500877.
(122) Treat, N. D.; Brady, M. A.; Smith, G.; Toney, M. F.; Kramer, E. J.; Hawker, C. J.; Chabinyc, M. L. Interdiffusion of PCBM and P3HT Reveals Miscibility in a Photovoltaically Active Blend. *Adv. Energy Mater.* **2011**, *1* (1), 82–89.
(123) Wirix, M. J. M.; Bomans, P. H. H.; Hendrix, M. M. R. M.; Friedrich, H.; Sommerdijk, N. A. J. M.; With, G. de. Visualizing Order in Dispersions and Solid State Morphology with Cryo-TEM and Electron Tomography: P3HT:PCBM Organic Solar Cells. *J. Mater. Chem. A* **2015**, *3* (9), 5031–5040.
(124) Herzing, A. A.; Richter, L. J.; Anderson, I. M. 3D Nanoscale Characterization of Thin-Film Organic Photovoltaic Device Structures via Spectroscopic Contrast in the TEM 1. *J. Phys. Chem. C* **2010**, *114* (41), 17501–17508.
(125) Roehling, J. D.; Baran, D.; Sit, J.; Kassar, T.; Ameri, T.; Unruh, T.; Brabec, C. J.; Moulé, A. J. Nanoscale Morphology of PTB7 Based Organic Photovoltaics as a Function of Fullerene Size. *Sci. Rep.* **2016**, *6*, 30915.
(126) Liu, F.; Zhao, W.; Tumbleston, J. R.; Wang, C.; Gu, Y.; Wang, D.; Briseno, A. L.; Ade, H.; Russell, T. P. Understanding the Morphology of PTB7:PCBM Blends in Organic Photovoltaics. *Adv. Energy Mater.* **2014**, *4* (5), 1301377.
(127) Westacott, P.; Tumbleston, J. R.; Shoaee, S.; Fearn, S.; Bannock, J. H.; Gilchrist, J. B.; Heutz, S.; deMello, J.; Heeney, M.; Ade, H.; et al. On the Role of Intermixed Phases in Organic Photovoltaic Blends. *Energy Environ. Sci.* **2013**, *6* (9), 2756–2764.
(128) Matteocci, F.; Busby, Y.; Pireaux, J.-J.; Divitini, G.; Cacovich, S.; Ducati, C.; Di Carlo, A. Interface and Composition Analysis on Perovskite Solar Cells. *ACS Appl. Mater. Interfaces* **2015**, *7* (47), 26176–26183.
(129) Mok, J. W.; Kipp, D.; Hasbun, L. R.; Dolocan, A.; Strzalka, J.; Ganesan, V.; Verduzco, R. Parallel Bulk Heterojunction Photovoltaics Based on All-Conjugated Block Copolymer Additives. *J. Mater. Chem. A* **2016**, *4* (38), 14804–14813.

(130) Pavlopoulou, E.; Fleury, G.; Deribew, D.; Cousin, F.; Geoghegan, M.; Hadziioannou, G. Phase Separation-Driven Stratification in Conventional and Inverted P3HT:PCBM Organic Solar Cells. *Org. Electron.* **2013**, *14* (5), 1249–1254.
(131) Busby, Y.; List-Kratochvil, E. J. W.; Pireaux, J.-J. Chemical Analysis of the Interface in Bulk-Heterojunction Solar Cells by X-Ray Photoelectron Spectroscopy Depth Profiling. *ACS Appl. Mater. Interfaces* **2017**, *9* (4), 3842–3848.
(132) Vickerman, J.; Briggs, D. *TOF-SIMS: Materials Analysis by Mass Spectrometry*, 2nd ed.; IM Publications LLP and SurfaceSpectra Limited: UK, 2013.
(133) Benninghoven, A. Surface Analysis by Secondary Ion Mass Spectrometry (SIMS). *Surf. Sci.* **1994**, *299–300*, 246–260.
(134) IONTOF. TOF-SIMS surface analysis: time of flight secondary ion mass spectrometry products by IONTOF. Leading manufacturer for TOF-SIMS products worldwide https://www.iontof.com/tof-sims-5-product-version-100mm-200mm-300mm.html (accessed Feb 5, 2018).
(135) Zimmerman, J. D.; Lassiter, B. E.; Xiao, X.; Sun, K.; Dolocan, A.; Gearba, R.; Vanden Bout, D. A.; Stevenson, K. J.; Wickramasinghe, P.; Thompson, M. E.; et al. Control of Interface Order by Inverse Quasi-Epitaxial Growth of Squaraine/Fullerene Thin Film Photovoltaics. *ACS Nano* **2013**, *7* (10), 9268–9275.
(136) Hofmann, S. Sputter Depth Profile Analysis of Interfaces. *Rep. Prog. Phys.* **1998**, *61* (7), 827.
(137) Brison, J.; Muramoto, S.; Castner, D. G. ToF-SIMS Depth Profiling of Organic Films: A Comparison between Single-Beam and Dual-Beam Analysis. *J. Phys. Chem. C* **2010**, *114* (12), 5565–5573.
(138) Dubey, M.; Brison, J.; Grainger, D. W.; Castner, D. G. Comparison of Bi1+, Bi3+ and C60+ Primary Ion Sources for ToF-SIMS Imaging of Patterned Protein Samples. *Surf. Interface Anal.* **2011**, *43* (1–2), 261–264.
(139) Muramoto, S.; Brison, J.; Castner, D. G. Exploring the Surface Sensitivity of TOF-Secondary Ion Mass Spectrometry by Measuring the Implantation and Sampling Depths of Bin and C60 Ions in Organic Films. *Anal. Chem.* **2012**, *84* (1), 365–372.
(140) Iltgen, K.; Bendel, C.; Benninghoven, A.; Niehuis, E. Optimized Time-of-Flight Secondary Ion Mass Spectroscopy Depth Profiling with a Dual Beam Technique. *J. Vac. Sci. Technol. Vac. Surf. Films* **1997**, *15* (3), 460–464.
(141) Hofmann, S. From Depth Resolution to Depth Resolution Function: Refinement of the Concept for Delta Layers, Single Layers and Multilayers. *Surf. Interface Anal.* **1999**, *27* (9), 825–834.
(142) Hofmann, S. Profile Reconstruction in Sputter Depth Profiling. *Thin Solid Films* **2001**, *398–399*, 336–342.
(143) Magee, C. W.; Honig, R. E. Depth Profiling by SIMS—depth Resolution, Dynamic Range and Sensitivity. *Surf. Interface Anal.* **1982**, *4* (2), 35–41.

(144) Chou, H.; Ismach, A.; Ghosh, R.; Ruoff, R. S.; Dolocan, A. Revealing the Planar Chemistry of Two-Dimensional Heterostructures at the Atomic Level. *Nat. Commun.* **2015**, *6*, 7482.
(145) McLean, R. S.; Sauer, B. B. Tapping-Mode AFM Studies Using Phase Detection for Resolution of Nanophases in Segmented Polyurethanes and Other Block Copolymers. *Macromolecules* **1997**, *30* (26), 8314–8317.
(146) Chang, K.-C.; Chiang, Y.-W.; Yang, C.-H.; Liou, J.-W. Atomic Force Microscopy in Biology and Biomedicine. *Tzu Chi Med. J.* **2012**, *24* (4), 162–169.
(147) Hansma, P. K.; Cleveland, J. P.; Radmacher, M.; Walters, D. A.; Hillner, P. E.; Bezanilla, M.; Fritz, M.; Vie, D.; Hansma, H. G.; Prater, C. B.; et al. Tapping Mode Atomic Force Microscopy in Liquids. *Appl. Phys. Lett.* **1994**, *64* (13), 1738–1740.
(148) Magonov, S. N.; Elings, V.; Whangbo, M.-H. Phase Imaging and Stiffness in Tapping-Mode Atomic Force Microscopy. *Surf. Sci.* **1997**, *375* (2), L385–L391.
(149) Johnson, D.; Hilal, N.; Bowen, W. R. Basic Principles of Atomic Force Microscopy. In *Atomic Force Microscopy in Process Engineering*; Butterworth-Heinemann; pp 1–30.
(150) Rogers, B.; Manning, L.; Sulchek, T.; Adams, J. D. Improving Tapping Mode Atomic Force Microscopy with Piezoelectric Cantilevers. *Ultramicroscopy* **2004**, *100* (3), 267–276.
(151) Kubicek, M.; Holzlechner, G.; Opitz, A. K.; Larisegger, S.; Hutter, H.; Fleig, J. A Novel ToF-SIMS Operation Mode for Sub 100 Nm Lateral Resolution: Application and Performance. *Appl. Surf. Sci.* **2014**, *289* (100), 407–416.
(152) Koch, S.; Ziegler, G.; Hutter, H. ToF-SIMS Measurements with Topographic Information in Combined Images. *Anal. Bioanal. Chem.* **2013**, *405* (22), 7161–7167.
(153) Jung, S.; Lee, N.; Choi, M.; Lee, J.; Cho, E.; Joo, M. Methodological Development of Topographic Correction in 2D/3D ToF-SIMS Images Using AFM Images. *Appl. Surf. Sci.* **2018**, *432*, 90–96.
(154) Terlier, T.; Lee, J.; Lee, K.; Lee, Y. Improvement of the Correlative AFM and ToF-SIMS Approach Using an Empirical Sputter Model for 3D Chemical Characterization. *Anal. Chem.* **2018**, *90* (3), 1701–1709.
(155) Gulin, A.; Nadtochenko, V.; Astafiev, A.; Pogorelova, V.; Rtimi, S.; Pogorelov, A. Correlating Microscopy Techniques and ToF-SIMS Analysis of Fully Grown Mammalian Oocytes. *Analyst* **2016**, *141* (13), 4121–4129.
(156) Elko-Hansen, T. D.-M.; Dolocan, A.; Ekerdt, J. G. Atomic Interdiffusion and Diffusive Stabilization of Cobalt by Copper During Atomic Layer Deposition from Bis(N-Tert-Butyl-N′-Ethylpropionamidinato) Cobalt(II). *J. Phys. Chem. Lett.* **2014**, *5* (7), 1091–1095.
(157) Robinson, M. A.; Graham, D. J.; Castner, D. G. ToF-SIMS Depth Profiling of Cells: Z-Correction, 3D Imaging, and Sputter Rate of Individual NIH/3T3 Fibroblasts. *Anal. Chem.* **2012**, *84* (11), 4880–4885.

(158) Wirtz, T.; Fleming, Y.; Gysin, U.; Glatzel, T.; Wegmann, U.; Meyer, E.; Maier, U.; Rychen, J. Combined SIMS-SPM Instrument for High Sensitivity and High-Resolution Elemental 3D Analysis. *Surf. Interface Anal.* **2013**, *45* (1), 513–516.
(159) Whitby, J. A.; Östlund, F.; Horvath, P.; Gabureac, M.; Riesterer, J. L.; Utke, I.; Hohl, M.; Sedláček, L.; Jiruše, J.; Friedli, V.; et al. High Spatial Resolution Time-of-Flight Secondary Ion Mass Spectrometry for the Masses: A Novel Orthogonal ToF FIB-SIMS Instrument with In Situ AFM. *Adv. Mater. Sci. Eng.* **2012**, 180437.
(160) Celio, H. Interface Designed with Differential Pumping and Built-in Figure of Merit Method to Monitor Chambers Where Environmentally Sensitive Samples Are Prepared and Transferred for Analysis. US20150037904 A1, February 5, 2015.
(161) HeliaFilm - Heliatek. http://www.heliatek.com/en/heliafilm (accessed Mar 8, 2016).
(162) Gomez, E. D.; Barteau, K. P.; Wang, H.; Toney, M. F.; Loo, Y.-L. Correlating the Scattered Intensities of P3HT and PCBM to the Current Densities of Polymer Solar Cells. *Chem. Commun.* **2010**, *47* (1), 436–438.
(163) Yin, W.; Dadmun, M. A New Model for the Morphology of P3HT/PCBM Organic Photovoltaics from Small-Angle Neutron Scattering: Rivers and Streams. *ACS Nano* **2011**, *5* (6), 4756–4768.
(164) Mok, J. W.; Kipp, D. R.; Hasbun, L. R.; Dolocan, A.; Strzalka, J.; Ganesan, V.; Verduzco, R. Parallel Bulk Heterojunction Photovoltaics Based on All-Conjugated Block Copolymer Additives. *J. Mater. Chem. A* **2016**, *4* (38), 14804–14813.
(165) Elko-Hansen, T. D.-M.; Dolocan, A.; Ekerdt, J. G. Atomic Interdiffusion and Diffusive Stabilization of Cobalt by Copper During Atomic Layer Deposition from Bis(N-Tert-Butyl-N′-Ethylpropionamidinato) Cobalt(II). *J. Phys. Chem. Lett.* **2014**, *5* (7), 1091–1095.
(166) Ye, L.; Jiao, X.; Zhao, W.; Zhang, S.; Yao, H.; Li, S.; Ade, H.; Hou, J. Manipulation of Domain Purity and Orientational Ordering in High Performance All-Polymer Solar Cells. *Chem. Mater.* **2016**, *28* (17), 6178–6185.
(167) Chen, D.; Liu, F.; Wang, C.; Nakahara, A.; Russell, T. P. Bulk Heterojunction Photovoltaic Active Layers via Bilayer Interdiffusion. *Nano Lett.* **2011**, *11* (5), 2071–2078.
(168) Campoy-Quiles, M.; Ferenczi, T.; Agostinelli, T.; Etchegoin, P. G.; Kim, Y.; Anthopoulos, T. D.; Stavrinou, P. N.; Bradley, D. D. C.; Nelson, J. Morphology Evolution via Self-Organization and Lateral and Vertical Diffusion in Polymer:Fullerene Solar Cell Blends. *Nat. Mater.* **2008**, *7* (2), 158–164.
(169) Kohn, P.; Rong, Z.; Scherer, K. H.; Sepe, A.; Sommer, M.; Müller-Buschbaum, P.; Friend, R. H.; Steiner, U.; Hüttner, S. Crystallization-Induced 10-Nm Structure Formation in P3HT/PCBM Blends. *Macromolecules* **2013**, *46* (10), 4002–4013.

(170) van Bavel, S.; Sourty, E.; de With, G.; Frolic, K.; Loos, J. Relation between Photoactive Layer Thickness, 3D Morphology, and Device Performance in P3HT/PCBM Bulk-Heterojunction Solar Cells. *Macromolecules* **2009**, *42* (19), 7396–7403.
(171) Gasparini, N.; Jiao, X.; Heumueller, T.; Baran, D.; Matt, G. J.; Fladischer, S.; Spiecker, E.; Ade, H.; Brabec, C. J.; Ameri, T. Designing Ternary Blend Bulk Heterojunction Solar Cells with Reduced Carrier Recombination and a Fill Factor of 77%. *Nat. Energy* **2016**, *1*, 16118.
(172) Singh, T.; Singh, J.; Miyasaka, T. Role of Metal Oxide Electron-Transport Layer Modification on the Stability of High Performing Perovskite Solar Cells. *ChemSusChem* **2016**, *9* (18), 2559–2566.
(173) Wang, D.; Wright, M.; Elumalai, N. K.; Uddin, A. Stability of Perovskite Solar Cells. *Sol. Energy Mater. Sol. Cells* **2016**, *147*, 255–275.
(174) Zuo, C.; Bolink, H. J.; Han, H.; Huang, J.; Cahen, D.; Ding, L. Advances in Perovskite Solar Cells. *Adv. Sci.* **2016**, *3* (7), 1500324.
(175) Kim, H.-S.; Seo, J.-Y.; Park, N.-G. Material and Device Stability in Perovskite Solar Cells. *ChemSusChem* **2016**, *9* (18), 2528–2540.
(176) Seo, J.; Noh, J. H.; Seok, S. I. Rational Strategies for Efficient Perovskite Solar Cells. *Acc. Chem. Res.* **2016**, *49* (3), 562–572.
(177) Bi, D.; Tress, W.; Dar, M. I.; Gao, P.; Luo, J.; Renevier, C.; Schenk, K.; Abate, A.; Giordano, F.; Baena, J.-P. C.; et al. Efficient Luminescent Solar Cells Based on Tailored Mixed-Cation Perovskites. *Sci. Adv.* **2016**, *2* (1), 1501170.
(178) Yin, W.; Pan, L.; Yang, T.; Liang, Y. Recent Advances in Interface Engineering for Planar Heterojunction Perovskite Solar Cells. *Molecules* **2016**, *21* (7), 837.
(179) Schmidt, T. M.; Larsen-Olsen, T. T.; Carlé, J. E.; Angmo, D.; Krebs, F. C. Upscaling of Perovskite Solar Cells: Fully Ambient Roll Processing of Flexible Perovskite Solar Cells with Printed Back Electrodes. *Adv. Energy Mater.* **2015**, *5* (15), 1500569.
(180) Zuo, C.; Ding, L. Modified PEDOT Layer Makes a 1.52 V Voc for Perovskite/PCBM Solar Cells. *Adv. Energy Mater.* **2017**, *7* (2), 1601193.
(181) Zuo, C.; Ding, L. Solution-Processed Cu2O and CuO as Hole Transport Materials for Efficient Perovskite Solar Cells. *Small* **2015**, *11* (41), 5528–5532.
(182) Jeng, J.-Y.; Chiang, Y.-F.; Lee, M.-H.; Peng, S.-R.; Guo, T.-F.; Chen, P.; Wen, T.-C. CH3NH3PbI3 Perovskite/Fullerene Planar-Heterojunction Hybrid Solar Cells. *Adv. Mater.* **2013**, *25* (27), 3727–3732.
(183) Kang, H.; Lee, W.; Oh, J.; Kim, T.; Lee, C.; Kim, B. J. From Fullerene–Polymer to All-Polymer Solar Cells: The Importance of Molecular Packing, Orientation, and Morphology Control. *Acc. Chem. Res.* **2016**, *49* (11), 2424–2434.
(184) Sun, C.; Wu, Z.; Yip, H.-L.; Zhang, H.; Jiang, X.-F.; Xue, Q.; Hu, Z.; Hu, Z.; Shen, Y.; Wang, M.; et al. Amino-Functionalized Conjugated Polymer as an Efficient Electron Transport Layer for High-Performance Planar-Heterojunction Perovskite Solar Cells. *Adv. Energy Mater.* **2016**, *6* (5), 1501534.

(185) Wang, W.; Yuan, J.; Shi, G.; Zhu, X.; Shi, S.; Liu, Z.; Han, L.; Wang, H.-Q.; Ma, W. Inverted Planar Heterojunction Perovskite Solar Cells Employing Polymer as the Electron Conductor. *ACS Appl. Mater. Interfaces* **2015**, *7* (7), 3994–3999.
(186) Liu, D.; Kelly, T. L. Perovskite Solar Cells with a Planar Heterojunction Structure Prepared Using Room-Temperature Solution Processing Techniques. *Nat. Photonics* **2014**, *8* (2), 133–138.
(187) You, J.; Meng, L.; Song, T.-B.; Guo, T.-F.; Yang, Y. (Michael); Chang, W.-H.; Hong, Z.; Chen, H.; Zhou, H.; Chen, Q.; et al. Improved Air Stability of Perovskite Solar Cells via Solution-Processed Metal Oxide Transport Layers. *Nat. Nanotechnol.* **2016**, *11* (1), 75–81.
(188) Min, J.; Zhang, Z.-G.; Hou, Y.; Ramirez Quiroz, C. O.; Przybilla, T.; Bronnbauer, C.; Guo, F.; Forberich, K.; Azimi, H.; Ameri, T.; et al. Interface Engineering of Perovskite Hybrid Solar Cells with Solution-Processed Perylene–Diimide Heterojunctions toward High Performance. *Chem. Mater.* **2015**, *27* (1), 227–234.
(189) Kaltenbrunner, M.; Adam, G.; Głowacki, E. D.; Drack, M.; Schwödiauer, R.; Leonat, L.; Apaydin, D. H.; Groiss, H.; Scharber, M. C.; White, M. S.; et al. Flexible High Power-per-Weight Perovskite Solar Cells with Chromium Oxide–metal Contacts for Improved Stability in Air. *Nat. Mater.* **2015**, *14* (10), 1032–1039.
(190) Gil-Escrig, L.; Momblona, C.; Forgács, D.; Pla, S.; Fernández-Lázaro, F.; Sessolo, M.; Sastre-Santos, Á.; Bolink, H. J. Interface Engineering in Efficient Vacuum Deposited Perovskite Solar Cells. *Org. Electron.* **2016**, *37*, 396–401.
(191) Huang, J.; Gu, Z.; Zuo, L.; Ye, T.; Chen, H. Morphology Control of Planar Heterojunction Perovskite Solar Cells with Fluorinated PDI Films as Organic Electron Transport Layer. *Sol. Energy* **2016**, *133*, 331–338.
(192) Fan, B.; Meng, D.; Peng, D.; Lin, S.; Wang, Z.; Sun, Y. Perylene Bisimides as Efficient Electron Transport Layers in Planar Heterojunction Perovskite Solar Cells. *Sci. China Chem.* **2016**, *59* (12), 1658–1662.
(193) Zhang, H.; Xue, L.; Han, J.; Fu, Y. Q.; Shen, Y.; Zhang, Z.; Li, Y.; Wang, M. New Generation Perovskite Solar Cells with Solution-Processed Amino-Substituted Perylene Diimide Derivative as Electron-Transport Layer. *J. Mater. Chem. A* **2016**, *4* (22), 8724–8733.
(194) Kim, S. S.; Bae, S.; Jo, W. H. A Perylene Diimide-Based Non-Fullerene Acceptor as an Electron Transporting Material for Inverted Perovskite Solar Cells. *RSC Adv.* **2016**, *6* (24), 19923–19927.
(195) Shao, S.; Abdu-Aguye, M.; Qiu, L.; Lai, L.-H.; Liu, J.; Adjokatse, S.; Jahani, F.; Kamminga, M. E.; Brink, G. H. ten; Palstra, T. T. M.; et al. Elimination of the Light Soaking Effect and Performance Enhancement in Perovskite Solar Cells Using a Fullerene Derivative. *Energy Environ. Sci.* **2016**, *9* (7), 2444–2452.
(196) Xing, Y.; Sun, C.; Yip, H.-L.; Bazan, G. C.; Huang, F.; Cao, Y. New Fullerene Design Enables Efficient Passivation of Surface Traps in High Performance P-i-n Heterojunction Perovskite Solar Cells. *Nano Energy* **2016**, *26*, 7–15.

(197) Yan, W.; Ye, S.; Li, Y.; Sun, W.; Rao, H.; Liu, Z.; Bian, Z.; Huang, C. Hole-Transporting Materials in Inverted Planar Perovskite Solar Cells. *Adv. Energy Mater.* **2016**, *6* (17), 1600474.
(198) Tang, F.; Chen, Q.; Chen, L.; Ye, F.; Cai, J.; Chen, L. Mixture Interlayer for High Performance Organic-Inorganic Perovskite Photodetectors. *Appl. Phys. Lett.* **2016**, *109* (12), 123301.
(199) Wei, J.; Li, H.; Zhao, Y.; Zhou, W.; Fu, R.; Leprince-Wang, Y.; Yu, D.; Zhao, Q. Suppressed Hysteresis and Improved Stability in Perovskite Solar Cells with Conductive Organic Network. *Nano Energy* **2016**, *26*, 139–147.
(200) Huang, W.-J.; Huang, P.-H.; Yang, S.-H. PCBM Doped with Fluorene-Based Polyelectrolytes as Electron Transporting Layers for Improving the Performance of Planar Heterojunction Perovskite Solar Cells. *Chem. Commun.* **2016**, *52* (93), 13572–13575.
(201) Bai, Y.; Yu, H.; Zhu, Z.; Jiang, K.; Zhang, T.; Zhao, N.; Yang, S.; Yan, H. High Performance Inverted Structure Perovskite Solar Cells Based on a PCBM:Polystyrene Blend Electron Transport Layer. *J. Mater. Chem. A* **2015**, *3* (17), 9098–9102.
(202) Chiang, C.-H.; Wu, C.-G. Bulk Heterojunction Perovskite–PCBM Solar Cells with High Fill Factor. *Nat. Photonics* **2016**, *10* (3), 196–200.
(203) Tao, C.; Neutzner, S.; Colella, L.; Marras, S.; Kandada, A. R. S.; Gandini, M.; Bastiani, M. D.; Pace, G.; Manna, L.; Caironi, M.; et al. 17.6% Stabilized Efficiency in Low-Temperature Processed Planar Perovskite Solar Cells. *Energy Environ. Sci.* **2015**, *8* (8), 2365–2370.
(204) Mumyatov, A. V.; Leshanskaya, L. I.; Anokhin, D. V.; Dremova, N. N.; Troshin, P. A. Organic Field-Effect Transistors Based on Disubstituted Perylene Diimides: Effect of Alkyl Chains on the Device Performance. *Mendeleev Commun.* **2014**, *24* (5), 306–307.
(205) Distler, A.; Sauermann, T.; Egelhaaf, H.-J.; Rodman, S.; Waller, D.; Cheon, K.-S.; Lee, M.; Guldi, D. M. The Effect of PCBM Dimerization on the Performance of Bulk Heterojunction Solar Cells. *Adv. Energy Mater.* **2014**, *4* (1), 1300693.
(206) Yang, B.; Keum, J.; Ovchinnikova, O. S.; Belianinov, A.; Chen, S.; Du, M.-H.; Ivanov, I. N.; Rouleau, C. M.; Geohegan, D. B.; Xiao, K. Deciphering Halogen Competition in Organometallic Halide Perovskite Growth. *J. Am. Chem. Soc.* **2016**, *138* (15), 5028–5035.
(207) Ralaiarisoa, M.; Busby, Y.; Frisch, J.; Salzmann, I.; Pireaux, J.-J.; Koch, N. Correlation of Annealing Time with Crystal Structure, Composition, and Electronic Properties of CH3NH3PbI3−xClx Mixed-Halide Perovskite Films. *Phys. Chem. Chem. Phys.* **2016**, *19* (1), 828–836.
(208) Zhang, T.; Meng, X.; Bai, Y.; Xiao, S.; Hu, C.; Yang, Y.; Chen, H.; Yang, S. Profiling the Organic Cation-Dependent Degradation of Organolead Halide Perovskite Solar Cells. *J. Mater. Chem. A* **2017**, *5* (3), 1103–1111.
(209) deQuilettes, D. W.; Zhang, W.; Burlakov, V. M.; Graham, D. J.; Leijtens, T.; Osherov, A.; Bulović, V.; Snaith, H. J.; Ginger, D. S.; Stranks, S. D. Photo-

Induced Halide Redistribution in Organic–inorganic Perovskite Films. *Nat. Commun.* **2016**, *7*, 11683.
(210) Kato, Y.; Ono, L. K.; Lee, M. V.; Wang, S.; Raga, S. R.; Qi, Y. Silver Iodide Formation in Methyl Ammonium Lead Iodide Perovskite Solar Cells with Silver Top Electrodes. *Adv. Mater. Interfaces* **2015**, *2* (13), 1500195.
(211) Li, J.; Dong, Q.; Li, N.; Wang, L. Direct Evidence of Ion Diffusion for the Silver-Electrode-Induced Thermal Degradation of Inverted Perovskite Solar Cells. *Adv. Energy Mater.* **2017**, *7* (14), 1602922.
(212) Besleaga, C.; Abramiuc, L. E.; Stancu, V.; Tomulescu, A. G.; Sima, M.; Trinca, L.; Plugaru, N.; Pintilie, L.; Nemnes, G. A.; Iliescu, M.; et al. Iodine Migration and Degradation of Perovskite Solar Cells Enhanced by Metallic Electrodes. *J. Phys. Chem. Lett.* **2016**, *7* (24), 5168–5175.
(213) Berhe, T. A.; Su, W.-N.; Chen, C.-H.; Pan, C.-J.; Cheng, J.-H.; Chen, H.-M.; Tsai, M.-C.; Chen, L.-Y.; Dubale, A. A.; Hwang, B.-J. Organometal Halide Perovskite Solar Cells: Degradation and Stability. *Energy Environ. Sci.* **2016**, *9* (2), 323–356.
(214) Bryant, D.; Aristidou, N.; Pont, S.; Sanchez-Molina, I.; Chotchunangatchaval, T.; Wheeler, S.; Durrant, J. R.; Haque, S. A. Light and Oxygen Induced Degradation Limits the Operational Stability of Methylammonium Lead Triiodide Perovskite Solar Cells. *Energy Environ. Sci.* **2016**, *9* (5), 1655–1660.
(215) M. Azpiroz, J.; Mosconi, E.; Bisquert, J.; Angelis, F. D. Defect Migration in Methylammonium Lead Iodide and Its Role in Perovskite Solar Cell Operation. *Energy Environ. Sci.* **2015**, *8* (7), 2118–2127.
(216) Yang, T.-Y.; Gregori, G.; Pellet, N.; Grätzel, M.; Maier, J. The Significance of Ion Conduction in a Hybrid Organic–Inorganic Lead-Iodide-Based Perovskite Photosensitizer. *Angew. Chem. Int. Ed.* **2015**, *54* (27), 7905–7910.
(217) Yuan, Y.; Huang, J. Ion Migration in Organometal Trihalide Perovskite and Its Impact on Photovoltaic Efficiency and Stability. *Acc. Chem. Res.* **2016**, *49* (2), 286–293.
(218) Bae, S.; Kim, S.; Lee, S.-W.; Cho, K. J.; Park, S.; Lee, S.; Kang, Y.; Lee, H.-S.; Kim, D. Electric-Field-Induced Degradation of Methylammonium Lead Iodide Perovskite Solar Cells. *J. Phys. Chem. Lett.* **2016**, *7* (16), 3091–3096.
(219) Verwey, J. F. Time and Intensity Dependence of the Photolysis of Lead Halides. *J. Phys. Chem. Solids* **1970**, *31* (1), 163–168.
(220) Deng, Y.; Xiao, Z.; Huang, J. Light-Induced Self-Poling Effect on Organometal Trihalide Perovskite Solar Cells for Increased Device Efficiency and Stability. *Adv. Energy Mater.* **2015**, *5* (20), 1500721.
(221) Xing, J.; Wang, Q.; Dong, Q.; Yuan, Y.; Fang, Y.; Huang, J. Ultrafast Ion Migration in Hybrid Perovskite Polycrystalline Thin Films under Light and Suppression in Single Crystals. *Phys. Chem. Chem. Phys.* **2016**, *18* (44), 30484–30490.
(222) Yuan, Y.; Wang, Q.; Shao, Y.; Lu, H.; Li, T.; Gruverman, A.; Huang, J. Electric-Field-Driven Reversible Conversion Between Methylammonium Lead Triiodide

Perovskites and Lead Iodide at Elevated Temperatures. *Adv. Energy Mater.* **2016**, *6* (2), 1501803.
(223) Garcia-Belmonte, G.; Bisquert, J. Distinction between Capacitive and Noncapacitive Hysteretic Currents in Operation and Degradation of Perovskite Solar Cells. *ACS Energy Lett.* **2016**, *1* (4), 683–688.
(224) Wang, Q.; Shao, Y.; Xie, H.; Lyu, L.; Liu, X.; Gao, Y.; Huang, J. Qualifying Composition Dependent p and n Self-Doping in CH3NH3PbI3. *Appl. Phys. Lett.* **2014**, *105* (16), 163508.
(225) Yin, W.-J.; Shi, T.; Yan, Y. Unusual Defect Physics in CH3NH3PbI3 Perovskite Solar Cell Absorber. *Appl. Phys. Lett.* **2014**, *104*, 063903.
(226) Kim, J.; Lee, S.-H.; Lee, J. H.; Hong, K.-H. The Role of Intrinsic Defects in Methylammonium Lead Iodide Perovskite. *J. Phys. Chem. Lett.* **2014**, *5* (8), 1312–1317.
(227) Egger, D. A.; Kronik, L.; Rappe, A. M. Theory of Hydrogen Migration in Organic–Inorganic Halide Perovskites. *Angew. Chem. Int. Ed.* **2015**, *54* (42), 12437–12441.
(228) Liu, B.; Yu, X.-Y.; Zhu, Z.; Hua, X.; Yang, L.; Wang, Z. In Situ Chemical Probing of the Electrode–electrolyte Interface by ToF-SIMS. *Lab. Chip* **2014**, *14* (5), 855–859.
(229) Wang, Z.; Zhang, Y.; Liu, B.; Wu, K.; Thevuthasan, S.; Baer, D. R.; Zhu, Z.; Yu, X.-Y.; Wang, F. In Situ Mass Spectrometric Monitoring of the Dynamic Electrochemical Process at the Electrode–Electrolyte Interface: A SIMS Approach. *Anal. Chem.* **2017**, *89* (1), 960–965.
(230) Rohnke, M.; Schaepe, K.; Bachmann, A.-K.; Laenger, M.; Janek, J. In Situ ToF-SIMS Monitoring of SOFC Cathodes – A Case Study of La0.74Sr0.17Mn1.01O2.9 Model Electrodes. *Appl. Surf. Sci.* **2017**, *422*, 817–827.
(231) Bush, K. A.; Palmstrom, A. F.; Yu, Z. J.; Boccard, M.; Cheacharoen, R.; Mailoa, J. P.; McMeekin, D. P.; Hoye, R. L. Z.; Bailie, C. D.; Leijtens, T.; et al. 23.6%-Efficient Monolithic Perovskite/Silicon Tandem Solar Cells with Improved Stability. *Nat. Energy* **2017**, *2* (4), 17009.
(232) Slobodyan, O. V.; 0000-0002-9882-407X. Investigation of Charge Transport in Organic Photovoltaic Materials Using Lateral Device Structures. Thesis, 2016.

Vita

Monroe P. Griffin was born in Albany, NY and raised in Myrtle Beach, SC. After graduating from Socastee High School in 2008, he attended Wofford College to study Chemistry and Mathematics. He graduated college in 2012 as a member of Phi Beta Kappa and *magna cum laude* with dual degrees: a Bachelor of Science in Chemistry and a Bachelor of Arts in Mathematics with high honors and a concentration in Applied Mathematics (Honors Thesis titled "Modeling the Effects of Malaria Preventative Measures" under Dr. Anne Catlla). In combining his passion for both disciplines, he decided to attend graduate school at The University of Texas at Austin to pursue his doctorate in Physical Chemistry under the supervision of Professor David Vanden Bout.

Permanent email: griffinmp@utexas.edu

This dissertation was typed by the author.